2019

Developing X-ray Spectromicroscopic Techniques to Quantitatively Determine Population Statistics and Individual Particle Composition of Complex Mixed Aerosols

Matthew Fraund
University of the Pacific, matthewwf@msn.com

DEVELOPING X-RAY SPECTROMICROSCOPIC TECHNIQUES TO QUANTITATIVELY
DETERMINE POPULATION STATISTICS AND INDIVIDUAL PARTICLE COMPOSITION
OF COMPLEX MIXED AEROSOLS

by

Matthew W. Fraund

A Dissertation Submitted to the

Graduate School

In Partial Fulfilment of the

Requirements for the Degree of

DOCTOR OF PHILOSOPHY

Thomas J. Long School of Pharmacy and Health Sciences
Bioanalytical and Physical Chemistry

University of the Pacific
Stockton, California

2019

DEVELOPING X-RAY SPECTROMICROSCOPIC TECHNIQUES TO QUANTITATIVELY
DETERMINE POPULATION STATISTICS AND INDIVIDUAL PARTICLE COMPOSITION
OF COMPLEX MIXED AEROSOLS

by

Matthew W. Fraund

APPROVED BY:

Dissertation Advisor: Ryan Moffet, Ph.D.

Committee Member: Andreas Franz, Ph.D.

Committee Member: Jinhua Ren, Ph.D.

Committee Member: Balint Sztaráy, Ph.D.

Committee Member: James Hetrick, Ph.D.

Department Chair: Jerry Tsai, Ph.D.

Dean of Graduate School: Thomas Naehr, Ph.D.

DEVELOPING X-RAY SPECTROMICROSCOPIC TECHNIQUES TO QUANTITATIVELY
DETERMINE POPULATION STATISTICS AND INDIVIDUAL PARTICLE COMPOSITION
OF COMPLEX MIXED AEROSOLS

Copyright 2019

By

Matthew W. Fraund

DEDICATION

This dissertation is dedicated to my parents Diane and Curt Fraund. Their love and encouragement has been a constant throughout my life. I also want to dedicate this work to my fiancé Katy-Ann Kelley. Without her love and support and I wouldn't have been able to make it this far. Thank you.

ACKNOWLEDGEMENTS

DEVELOPING X-RAY SPECTROMICROSCOPIC TECHNIQUES TO QUANTITATIVELY
DETERMINE POPULATION STATISTICS AND INDIVIDUAL PARTICLE COMPOSITION
OF COMPLEX MIXED AEROSOLS

Abstract

by Matthew Wyatt Fraund

University of the Pacific
2019

Aerosols are a major source of uncertainty in estimates of anthropogenic effects on global radiative forcing and can pose serious health concerns. While many instrumental techniques capable of analyzing aerosol samples are available, individual-particle spectromicroscopic techniques like the ones presented here are the only ones to offer morphological and compositional measurements together. Studying the composition and mixing state of aerosol populations allowed for important aspects to be uncovered, such as: aerosol source, formation mechanism, hygroscopicity, optical properties, level of aging, and inhalation dangers. Ambient aerosols from the Amazon, both biogenic and anthropogenic, were apportioned based on their individual composition. Recently discovered organic aerosols from the central United States were identified and their chemical properties were characterized. The lead fraction of mixed lead- and zinc-rich particles from Mexico City was speciated to determine the lead's solubility and possible bioavailability. It is through the use of these powerful spectromicroscopic techniques that a better understanding of complex mixed aerosols was achieved.

TABLE OF CONTENTS

LIST OF TABLES

LIST OF FIGURES

LIST OF ABBREVIATIONS

AAE	Absorption Angström exponent
AE	Angström exponent
AHPS	Advanced hydrologic prediction service
ARM	Atmospheric radiation measurement facility
ACSM	Aerosol chemical speciation monitor
AED	Area equivalent diameter
AFM	Atomic force microscopy
ALS	Advanced light source
AMS	Aerosol mass spectrometer
ASOP	Airborne soil organic particle
ATOFMS	Aerosol time-of-flight mass spectrometer
ATTO	Amazon tall tower observatory
BC	Black Carbon
BNL	Brookhaven national laboratory
BrC	Brown Carbon
CCN	Cloud condensation nuclei
CED	Circular Equivalent Diameter
CLS	Canadian light source
D_i, D_α, D_γ	Diversity values (individual, average, and bulk respectively)
EC	Elemental carbon
EDX or EDS	Energy-dispersive X-ray spectroscopy
EELS	Electron energy loss spectroscopy
EMSL	Environmental molecular sciences laboratories
EPA	Environmental protection agency
FOV	Field of view
HISCALE	Holistic interactions of shallow clouds, aerosols, and land ecosystems
HOPG	Highly-ordered pyrolytic graphite
HYSPLIT	Hybrid single-particle lagrangian integrated trajectory model
ICP-AES	Inductively coupled plasma with atomic emission spectrophotometry
INP	Ice nucleating particle
IOP	Intensive operating period
IPCC	Intergovernmental Panel on Climate Change
LBL	Lawrence Berkeley laboratory
LIBS	Laser induced breakdown spectroscopy
Linac	Linear accelerator
MOUDI	Micro-orifice uniform deposit impactor
NEXAFS	Near-edge X-ray absorption fine-structure spectroscopy (also XANES)
NSLS-II	National synchrotron light source II
NWS	National weather service
OD	Optical density
OMF	Organic mass fraction
OSA	Order sorting aperture
OVF	Organic volume fraction
PIXE	Proton-induced X-ray Absorption
PM_{10}	Particulate matter with diameter > 10 μm

PM$_{2.5}$	Particulate matter with diameter > 2.5 μm
PNNL	Pacific northwest national laboratory
PSAP	Particle soot absorption photometer
RF	Radio frequency
RH	Relative humidity
SAED	Selected area electron diffraction
SEM	Scanning electron microscopy
SGP	Southern Great Plains
SIMS	Secondary ion mass spectrometry
SOA	Secondary organic aerosols
SOM	Soil organic matter
SP	Spherical Particle
SP2	Single-particle soot photometer
SPLAT	Single-particle laser ablation time-of-flight mass spectrometer
SRX	Sub-micron resolution X-ray beamline
STXM	Scanning transmission X-ray microscopy
T3	Sampling site designation in the Amazon
TEM	Transmission electron microscopy
TRAC	Time resolved aerosol collector
VOC	volatile organic compounds
XANES	X-ray absorption near-edge spectroscopy
XRF	X-ray fluorescence spectroscopy
ZF2	Small road marker in the Amazon
ZP	Zone plate
χ	Mixing state index

Chapter 1: Introduction

1.1 The Importance of Aerosols

      1.1.1 Aerosol impacts. Aerosols are any solid or liquid particles suspended in a gas, or

as is the case with ambient aerosols, the atmosphere.[1] One of the most easily understandable

issues that aerosol present is their impact on visibility. Aerosols from vehicle exhaust, industrial

processes, and combustion products (either from energy production or from fires) all contribute

to declining visibility.[2] Light absorbing particles like black carbon (BC, also known as soot) or

brown carbon (BrC) and light scattering particles like sulfates or organic particles emitted from

these sources can accumulate to the point of obscuring buildings and landmarks, Figure 1.1

shows two examples of greatly reduced visibility.[3]

Figure 1.1 Smog obscured skylines of two major cities. (top) Aerial picture of Los Angeles and surrounding area on a day with heavy smog. (bottom) Tourists pose in front of a picture of Hong Kong on a day with particularly bad visibility.

While less immediately apparent, one of the biggest impacts aerosols can have on our environment is how they influence temperature. There are two main ways in which aerosols do this (both of which are shown in Figure 1.2): through aerosol-radiation interactions and aerosol-cloud interactions.[4] Aerosol-radiation interactions (also known as the direct effect) deal with light being either scattered or absorbed directly by the aerosol itself. Absorbing aerosols such as soot or BrC can absorb solar radiation, leading to overall warming of the atmosphere. On the other hand, aerosols which chiefly scatter radiation (like sulfate-rich particles) can have a cooling effect on the atmosphere.[5] Aerosol-cloud interactions refer to the same scattering or absorption, except by the water droplets surrounding individual aerosol particles within clouds. Because it is unfavorable for water vapor to spontaneously coagulate into water droplets under normal

atmospheric conditions, aerosols are inextricably linked to the formation and behavior of clouds.[6-7]
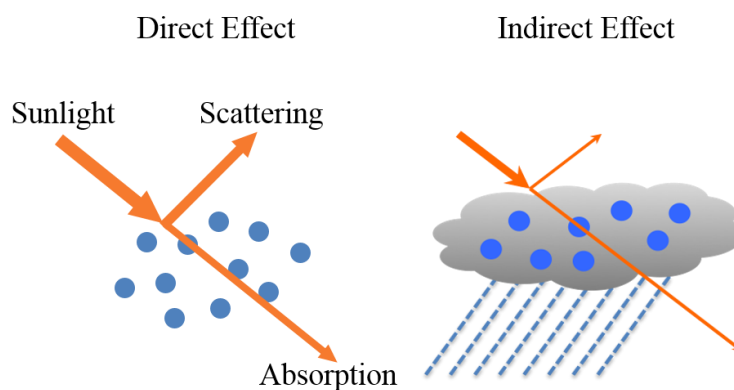
Figure 1.2 Diagrams of the direct and indirect effects.[8]

The extent to which any system, including aerosols and clouds, cool or warm the atmosphere is referred to as radiative forcing and is expressed in units of power per area (Watts per square meter usually).[9] As such, radiative forcing is one of the many outputs that climate models calculate, with positive radiative forcing values meaning overall warming. Because of this it is a key metric in determining a population of aerosol's impact on climate and it is often used (among many other things) to probe the question of how much humans are affecting our environment. Approximately every 7 years, the Intergovernmental Panel on Climate Change (IPCC) meets to answer just this type of question. The IPCC has involvement from over 100 countries with hundreds of scientists contributing to the writing and assessment of current literature. At the time of writing, they are working towards their sixth assessment report to be completed in 2022.[10] In the most recently released fifth assessment report in 2014 they show that aerosols and their effects on clouds contribute the greatest uncertainty in our understanding on anthropogenic radiative forcing.[4]

1.1.2 Health effects. Not only are aerosols of concern for environmental reasons, they can also be detrimental to our health as well. Inhalation of small mineral or dust particles over time can lead to pneumoconiosis, causing difficulty breathing and lung tissue scarring.[11] Reports of this type of disease are so prevalent that common names have been coined depending on the type of dust causing the issue: black lung or miner's lung from the inhalation of coal dust, asbestosis from inhalation of asbestos particles, and silicosis or grinder's asthma from inhalation of silica dust. Two size fractions have been noted as especially important to the ill health effects caused by particle inhalation. PM_{10} and $PM_{2.5}$ which stand for particulate matter smaller than 10 μm or smaller than 2.5 μm respectively. Figure 1.3 below shows a diagram of the respiratory system and how far PM_{10} and $PM_{2.5}$ travel when inhaled.[12] Because $PM_{2.5}$ are able to travel all the way down to the alveoli (small sacks where the body's gas exchange takes place), strong correlations between $PM_{2.5}$ and pulmonary disease and lung cancer have been observed.[13-15] The right plot in Figure 1.3 plots the mass density of $PM_{2.5}$ particles against the mortality rate ratio for 6 US cities, with the ratios being normalized to the city with the lowest $PM_{2.5}$ mass density. The dangers that $PM_{2.5}$ poses to air quality and human health has earned it a spot as one of the US environmental protection agencies (EPA) criteria air pollutants.[16]
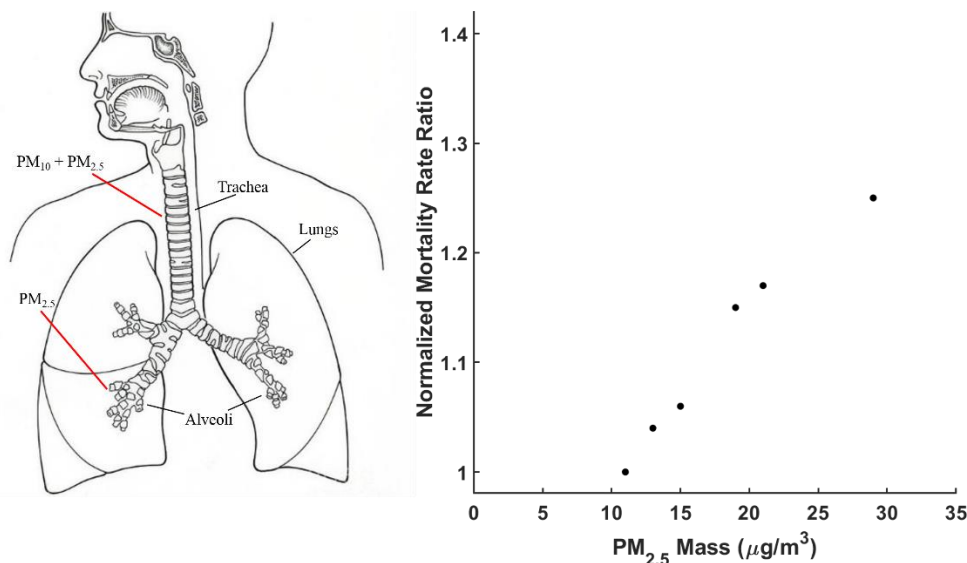
Figure 1.3 Aerosol inhalation depth and mortality rate ratio. (left) Diagram of the respiratory system with the depth to which inhaled aerosols will travel. (right) Plot of mortality rate ratio of 6 US cities normalized to the city with the lowest ratio.

The inhalation of general aerosols is not the only aspect with negative health effects. There are specific issues that can arise from the inhalation of aerosols like metals, for instance zinc, zinc oxide, and zinc chloride inhalation has been implicated in lung cancer, a decrease in lung capacity, and fluid buildup in the lungs.[17-18] Lead is another metal associated with many negative health effects, so much so that it is another of the EPA's criteria air pollutants.[16] Chronic lead exposure can have serious neurological effects with children, and their rapidly developing neurological system, being the most vulnerable.[19] The dangers posed by lead has previously resulted in the removal of leaded gasoline from many countries.

1.1.3 Aerosol classification. Aerosols can be split into two broad categories: naturally occurring biogenic aerosols and human-made anthropogenic aerosols.[1] Biogenic aerosols can include things like particles ejected from sea spray or mineral dust lifted from deserts or soil surfaces whereas anthropogenic aerosols include soot emitted from vehicles or metal particulates produced from industrial processes.[20] Aerosols can be further classified by their formation

mechanism into primary and secondary aerosols. Particles like sea spray or soot particles are examples of primary aerosols as they are produced and ejected into the atmosphere directly. Secondary aerosols, on the other hand, are formed through gas-phase reactions.[21] Reactions resulting in the formation of secondary aerosol are varied and range from simple to complex, multi-step reactions. Many secondary organic aerosols (SOA) are produced through gas-phase reactions, with volatile organic compounds (VOCs) reacting with oxidants such as ozone or hydroxyl radicals.[22] The volatile organic compounds can go through multiple oxidation steps ultimately resulting in less volatile compounds which can condense onto an existing aerosol or coagulate into a new particle.[23] While some gasses undergo reactions to produce secondary aerosols, other gasses are simply co-emitted. These co-emitted gasses can be useful in understanding the aerosol population present in a location. As an example, carbon monoxide is emitted almost exclusively from sources of combustion and because of this it can be used as a way to trace combustion products.[24-25]

In addition to source and formation mechanism, aerosols are also classified by their size. The size of an aerosol is closely linked to its origin and can give insight into what atmospheric processes it may have undergone. Aerosols can range anywhere from a few nanometers to 100 micrometers (approximately the width of a human hair). Generally, four distinct size modes are defined for ambient aerosol populations, each of which is shown in Figure 1.4 in different distributions.
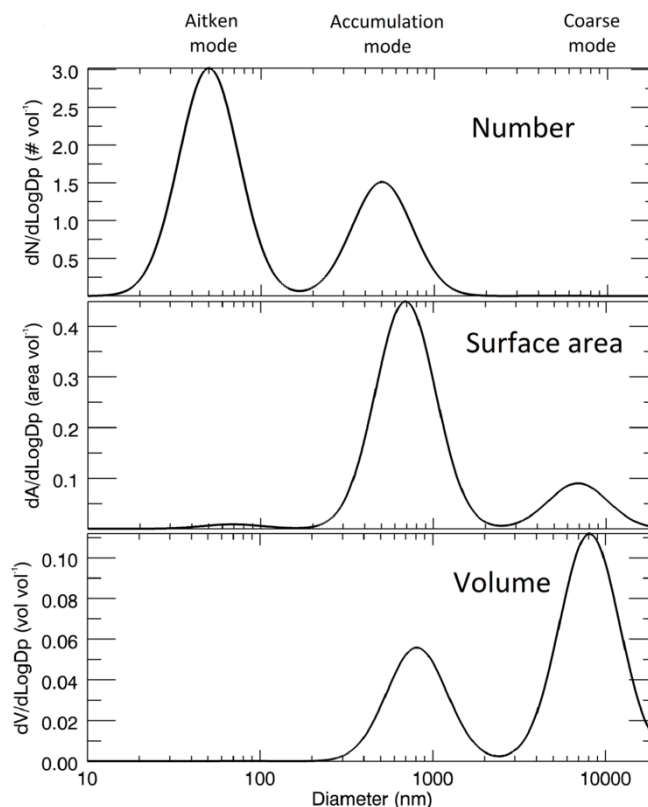
Figure 1.4 Number, surface area, and volume distributions of an aerosol population. This represents a synthetic distribution; experimental conditions may enhance or dampen individual modes. The vertical axis values are all normalized by the bin width of the horizontal axis to allow for comparison.

Coarse mode particles are the largest, consisting of particles greater than 1 μm. These aerosols account for the majority of the volume (and mass) of ambient aerosols, though they are much less numerous than particles of other modes.[26] Coarse mode particles are often primary aerosols and while some are organic like bacteria or plant/fungal spores, most of these particles are inorganic with mineral dust (metals and carbonate salts) and especially sea salt aerosols making up the majority of coarse mode particles. On the other end, nucleation mode (not shown in Figure 1.4) and Aitken mode particles greatly outnumber other particle sizes while making up a much smaller fraction of the volume of ambient aerosols. Nucleation mode particles (also referred to as the ultrafine mode) are <0.01 μm and consist mainly of secondary particles formed through nucleation of gas-to-particle reaction products.[27] For example, ammonium salts

represent a significant fraction of the fine aerosol mass (<0.1 μm)[28] and are formed through the reaction of gaseous ammonia with sulfuric or nitric acid to produce inorganic secondary aerosols as shown in Eq. 1.1 and Eq. 1.2.

$$NH_{3(g)} + H_2SO_{4(g)} \rightarrow (NH_4)_2SO_{4(s)} \tag{1.1}$$

$$NH_{3(g)} + HNO_{3(g)} \rightarrow NH_4NO_{3(s)} \tag{1.2}$$
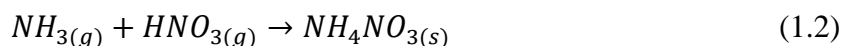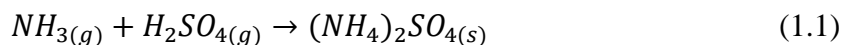
These particles quickly grow in size due to condensation of other compounds or impaction with other aerosols; this makes nucleation mode aerosols fleeting and difficult to measure, lasting for mere minutes before becoming Aitken mode particles. The Aitken mode is named after Scottish meteorologist John Aitken who first observed these particles.[29] In the middle of the size range are the accumulation mode particles which make up a smaller fraction of total aerosol volume and account for the greatest total surface area. In addition to aerosols produced at this size, smaller particles can grow to become accumulation mode aerosols. In addition to condensation of less volatile gasses onto smaller particles, this growth can be a result of coagulation where two or more aerosols collide to become a single particle.[30] Accumulation mode particles are also not removed from the atmosphere as easily as with other size ranges and thus particles tend to accumulate here, hence the name.

Ambient aerosols do not persist in the atmosphere indefinitely, Figure 1.5 outlines some of these aerosol removal mechanisms as well as some of the sources and processes mentioned above. Aerosols can settle over time due to gravity (sedimentation), as well as impact solid surfaces (removing them from the atmosphere) or other aerosols (decreasing total aerosol concentration).[31] These methods don't involve water or precipitation and so are known as dry deposition methods. Wet deposition methods include rainfall collecting or scavenging aerosols as it falls from clouds (washout) as well as aerosols impacting cloud droplets. In a calm, non-

turbulent environment gravitational settling removes larger aerosols the fastest. For coarse mode aerosols, 10 μm particles will fall 10 m in about an hour, while 1 μm particles will fall the same distance in 3 days. Nucleation and Aitken mode aerosols take much longer, months or years to fall the same 10 m.[1, 32] Turbulent air can serve to keep particles aloft longer, making gravitation sedimentation only an effective deposition method for large particles. This isn't to say fine mode aerosols persist indefinitely as other removal methods reduce the lifetimes of these particles to approximately 5 days, although atmospheric conditions can make this number quite variable.[33]
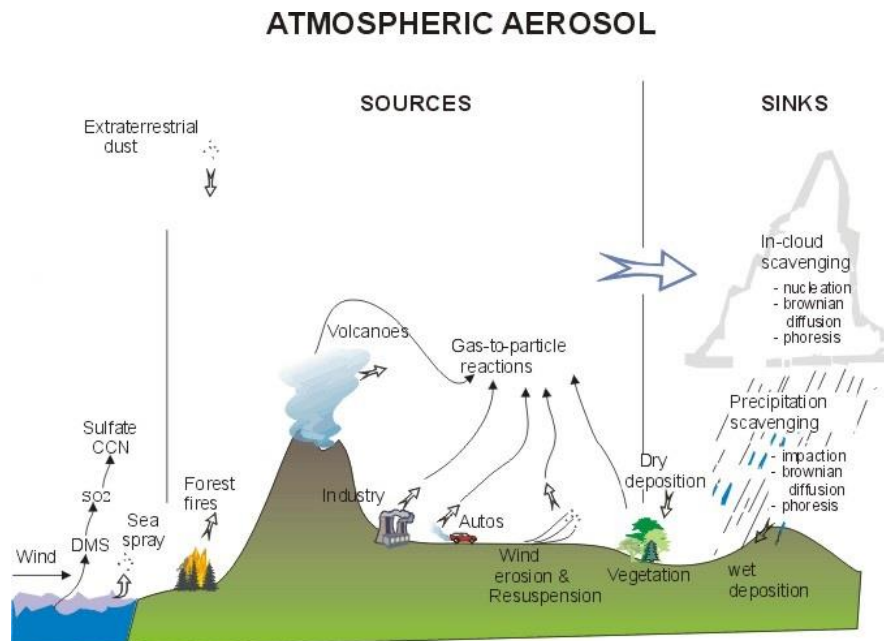
Figure 1.5 Diagram of select aerosol sources and sinks.

1.1.4 Aerosol composition. The composition of a population of aerosols can control its effect on health as well as its role in climate, both directly and through the formation of clouds. In general, coarse mode aerosols are comprised of mostly inorganics with calcium, magnesium, iron, and silicon (crustal elements) often present. Sea salt particles are also present in the coarse fraction containing sodium chloride and magnesium chloride along with biological particles like

fungal or plant spores. On average, fine mode particles contain ammonium, sulfate, and nitrate salts in addition to soot and a large variety of organic compounds. Knowing the composition of a population of aerosols can help to better understand their impact and, in turn, better define model parameters. For instance, many of the inorganic aerosols serve to scatter and reflect incoming solar radiation whereas soot absorbs solar radiation. Organic aerosols scatter radiation but to a much lesser extent than inorganic ones. Measurements of aerosol composition are vital for improving estimates of how much of each aerosol component is present and where concentrations might be elevated.

Not only is composition important for the aerosols already present in the atmosphere, but an aerosol's composition can be used to determine where it came from. Soot is an indicator of both biogenic and anthropogenic combustion; however, when soot is present alongside potassium it is an indicator that fossil fuel burning was the source.[34] Similarly, levoglucosan is a common fragment ion seen in mass spectra derived from cellulose. Finding levoglucosan with soot in the same aerosol sample points to biomass burning as the source.[35] Source apportionment with the use of tracers can help researchers understand a complex population of aerosols. Aerosols at a sampling site can be compared to aerosols collected at the source to investigate the aerosol aging process. Policymakers can be interested in aerosol sources like these as well, making decisions to curtail processes producing harmful aerosols.

The composition of a population of aerosols also plays a large role in determining their cloud nucleating properties. Because of surface area effects, a water droplet will only spontaneously nucleate if it is large enough. Under normal atmospheric conditions the probability that enough water molecules will clump together to overcome this barrier is essentially zero, making aerosols absolutely critical to the formation of clouds.[7, 36-37] Inorganic

aerosols like sodium chloride are especially hygroscopic, meaning they will pull water from the air. This makes them excellent cloud condensation nuclei (CCN), allowing a cloud droplet to form around the aerosol center. Organics tend to have the opposite effect, with hydrophobic components reducing the aerosol's effectiveness as a CCN.

    1.1.5 Mixing state. Aerosol's are rarely purely inorganic or organic and complex compositions like this highlight the need for single particle measurements. How components are distributed through a sample of aerosols is referred to as the sample's mixing state. Two terms are defined for the extreme cases (and are shown in Figure 1.6): an external mixture will have each aerosol comprised of a single component, while an internal mixture will have an equal amount of each component distributed within every aerosol (in other words, all of the aerosols are identical).
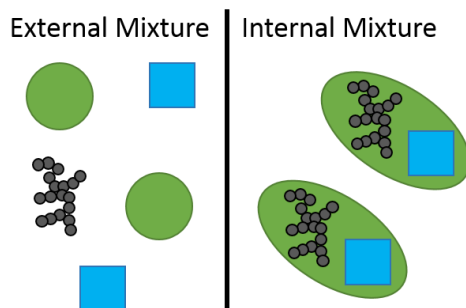
Figure 1.6 Example of external and internal aerosol mixtures.

Properly understanding the mixing state of aerosols and how it changes over time will help models more accurately predict optical properties and CCN activity.[38-39] The mixing state of a sample of particles is complicated however, and can change continuously over the lifetime of the aerosols. As aerosols age they can be subjected to coagulation with other aerosols, condensation of gasses, or to reactions changing their composition.[40]

With the numerous variations in mixing state as a particle is emitted and travels through the atmosphere, the binary designations of internal or external mixtures is insufficient. In an attempt to more carefully describe aerosol mixing state and, what's more, to quantify it for easier use in model systems, a mixing state parameter was developed by Nicole Riemer and Matt West. They use the concept of Shannon entropy (named after Claude Shannon, also called information entropy) to define diversity parameters. Simply put, Shannon entropy quantifies how uniform a probability distribution is. To do this, mass fractions of aerosol components are treated as probabilities and used to calculate the entropy followed by diversity metrics. From this both a bulk and an average particle diversity is calculated, with the diversity being essentially the mass weighted average of the number of components (components here, whether it be elements or molecules or something else, are defined by the user). Finally, the mixing state parameter is calculated from the ratio of average individual diversity (D_α) and bulk diversity (D_γ). Figure 1.7 illustrates some possible diversity and mixing state values from a sample of particles.

Population	Per-part. div. D_α	Bulk div. D_γ	Mix. state index χ	Description
	3	3	100%	all particles identical (fully internally mixed) with identical bulk fractions
	1	3	0%	all particles pure (1 effective species per particle, fully externally mixed) but identical bulk fractions (3 effective bulk species)
	1	1.89	0%	all particles pure (1 effective species per particle, fully externally mixed) but less than two effective bulk species
	2.37	3	68%	each particle has less than three effective species (unequal fractions) but bulk fractions are identical (3 effective bulk species)
	1.89	1.89	100%	all particles are identical (fully internally mixed) but less than 2 effective bulk species

Figure 1.7 Example particle populations and their diversity and mixing state. Reproduced from Riemer and West, 2013 under Creative Commons 3.0.[41]

1.1.6 Aerosol morphology. The composition of an aerosol indicates a great many things about its source and how it will interact with its environment, but it alone is not the sole deciding factor. Aerosol shape and how its components are spatially distributed, collectively called morphology, can modify or change how it behaves. Certain aerosols can even be partially identified by their morphology alone, something that can take much less time than composition measurements. Figure 1.8 below shows images taken using electron microscopy highlighting some different aerosol morphologies. Image A points to two particles, both of which are comprised of organics. The particle to the left retains its spherical shape upon impaction due to its higher viscosity, spherical particles like these are thought to be a type of underrepresented type of carbonaceous aerosol.[42-43] Image B depicts sea spray aerosols collected above breaking ocean waves. A cubic sodium chloride core (surrounded by a coating of organics) is a hallmark of these aerosols. Images C and D both are of a single soot particle. When soot is first emitted it

is a branching, fractal particle with many small spherules as seen in C.[44-45] As the soot particle

travels over time and distance it compacts into the particle seen in D; this aging process can

change the behavior of the aerosol.[46-47] For example, the surface area of the soot particle

decreases which will reduce the likelihood of heterogeneous reactions.
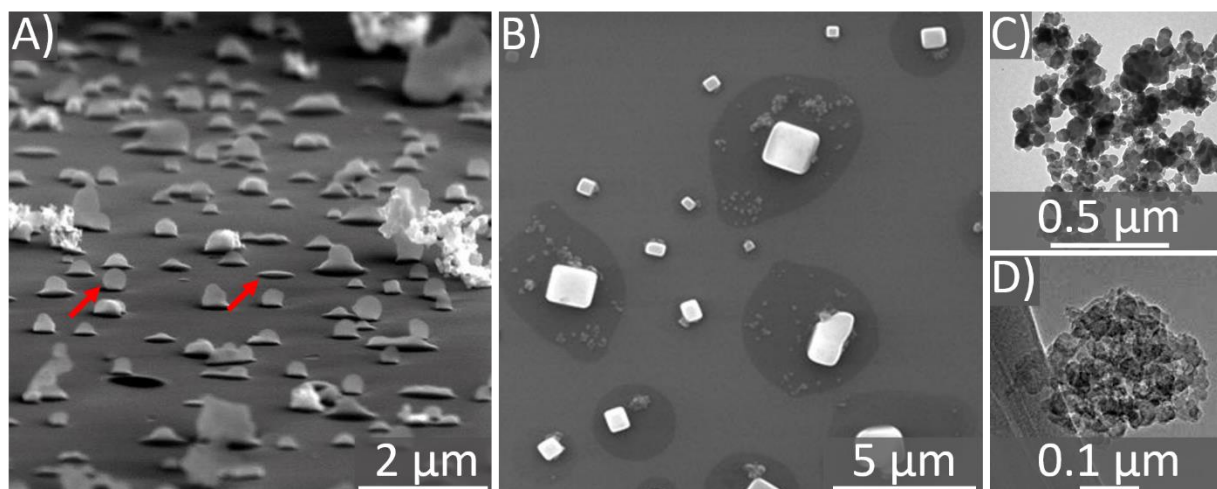
Figure 1.8 Electron micrographs of aerosols with various morphologies. A) Image taken at a 75° angle, red arrows point to a flat and a spherical particle, both of which are organic. B) Sea spray aerosol showing cubic NaCl crystals coated by an organic layer (copyright 2016, Proceedings of the National Academy of Sciences).[48] C) Freshly emitted soot particle showing fractal geometry. D) Aged soot particle with a compacted morphology (reproduced from China, et al, 2015 under Creative Commons 3.0).[49]

Not only is the overall shape of an aerosol important, but how the various components are

distributed within an aerosol can affect how it behaves in the atmosphere. When soot is emitted

it is composed of elemental carbon. These fresh soot particles (also called black carbon or BC)

strongly absorb solar radiation, in fact they've been deemed the second biggest source of

anthropogenic radiative forcing after CO_2.[50] While traveling through the atmosphere,

heterogeneous reactions and gas condensation can coat these soot particles with a layer of

organics.[51] A lensing effect has been observed with these organic coatings, where light is

refracted inward toward the central soot particle, effectively increasing the radiative forcing.[52]

Akin to how the spatial distribution of aerosol components can affect aerosol-radiation interactions, aerosol-cloud interactions also depend on internal morphology. Sodium chloride is ubiquitous in the atmosphere due to its high concentration in seawater and the vast amount of the earth's surface area covered by ocean. Being hygroscopic, sodium chloride particles act as CCN, with water condensing onto the particles to form cloud droplets. However, many sodium chloride particles are observed with an organic coating which can hinder water condensation and reduce the particle's effective hygroscopicity and its ability to act as a CCN.[53] To add more complexity to the issue, particles don't exist in a binary state of uncoated or coated. Figure 1.9 portrays two inorganic/organic particles with either a core-shell or partially-engulfed morphology. Inorganic components that are only partially-engulfed by organics, like the left column of Figure 1.9, will not have their effective hygroscopicity decreased as much as with the core-shell arrangement.[54]
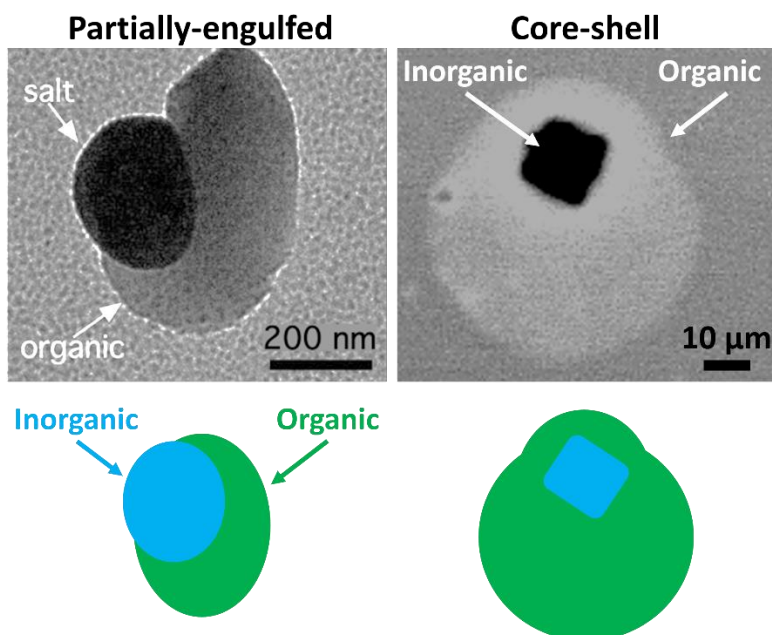
Figure 1.9 Core-shell and partially-engulfed mixed aerosols. Electron micrograph (top row) and color-coded schematic (bottom row) of separated organic/inorganic aerosols. Top left image adapted with permission from Veghte, *et al.* 2013.[55] Copyright 2013 American Chemical Society.

1.2 Measurement of Aerosol Physical and Chemical Properties

    1.2.1 Bulk analysis. To better understand aerosols, some of the most straightforward measurement techniques are bulk analysis methods. These often involve the collection of filter samples where ambient air is forced through a fine filter over the course of minutes to days depending on experimental methods and objectives. A quantitative elemental composition can be determined using techniques like inductively coupled plasma with atomic emission spectrophotometry (ICP-AES), which intensely heats a sample resulting in a total atomic emission spectrum.[56] Proton-induced X-ray emission (PIXE) spectroscopy can give elemental information as well without being destructive to the sample. PIXE uses protons to excite inner electrons which then relax and emit elementally specific X-rays.[57] If more specific information is needed, the loaded filter (or parts of it) can be digested with acid to form a solution from the aerosols.[58] This solution can be subjected to chemical reactions, column chromatography, or solution phase mass spectrometry techniques.

    The above measurements are considered offline analysis methods because they take a sample of an aerosol population and then conduct measurements weeks or months later. While this can have the benefit of using other measurements to decide which dates or analyses are important and can allow for more time consuming techniques, online techniques have the advantage of capturing real-time information. Aerosol plumes can change depending on wind direction or can have time-dependent compositions, making real-time instruments vital. Thermo-optical analysis is a common online method which can quantitatively determine the organic and elemental carbon fractions in an aerosol.[59-61] Thermo-optical instruments and procedures have been modified and improved over years, with the European Committee for Standardization (CEN) making it the reference method for quantifying organic and elemental carbon.[62] Here aerosols are allowed to flow into an inert (usually He) atmosphere inside a

heating chamber. The temperature is raised in steps up to 600 °C after which $O_{2(g)}$ is introduced and the temperature is further increased in steps to 850 °C, during each of these temperature steps the amount of $CO_{2(g)}$ released is measured. Because the organic fraction oxidizes at lower temperatures than elemental carbon, the mass of each fraction can be calculated from the amount of CO_2 released. More composition information is available with the use of an aerosol mass spectrometer (AMS) and the related aerosol chemical speciation monitor (ACSM). These two instruments both focus a stream of particles onto a heating element where they are vaporized and subjected to electron ionization. The ACSM then uses a residual gas analyzer mass spectrometer to measure the amount of organic, sulfate, nitrate, ammonium, and chloride in the aerosols based on the signal at chosen *m/z* values.[63] The AMS works similarly but yields a full, higher resolution mass spectrum.[64] Laser-induced breakdown spectroscopy (LIBS) can be used to measure elemental composition in real-time by focusing an energetic laser pulse into a plasma.[65-66] The plasma atomizes the sample and the elementally characteristic X-rays are measured. The experimental conditions can vary from one laser pulse to another, however, which makes quantitative analysis difficult.[67-69]

1.2.2 Single particle analysis. Many different types of aerosols can make up an aerosol plume and each of these particles will interact with the surrounding environment based on their individual composition. Bulk analysis can be useful for identifying trends or for observing when an aerosol plume changes, but to properly understand (and model) a population of particles it is necessary to study them on an individual level. For the ever-important soot particle, the single particle soot photometer (SP2) is widely used.[70-72] This *in-situ* instrument uses a laser to heat incoming particles. Those particles which strongly absorb the light (soot) will be heated to incandescence. This incandescent emission is measured and correlated with the soot mass in

each particle.[73-75] Mass spectrometry has been applied to single particle *in-situ* measurements as well. Single particle aerosol mass spectrometers such as the aerosol time-of-flight mass spectrometer (ATOFMS) and the single particle laser ablation time-of-flight (SPLAT) mass spectrometer both use 2 lasers separated by a known distance to identify particles and their velocity, this allows a third desorption-ionization laser to be triggered at the precise time an aerosol crosses its beam path.[76-77] Work has been done previously to determine density and optical properties along with composition information using an ATOFMS.[78]

Online instruments can give detailed composition information in real-time but aerosols are complex and often heterogeneous mixtures. The overall shape of an aerosol, along with how its inner components are distributed, can impact how the particle interacts with its environment. To probe morphology and the spatial distribution of components within individual particles an offline technique like spectromicroscopy is needed. This usually involves impacting aerosols onto a substrate like a silicon nitride (Si_3N_4) membrane or a copper grid coated with a thin membrane (like Formvar). A popular tool for impaction sampling is a micro-orifice uniform deposit impactor (MOUDI) which is shown below in Figure 1.10. This device uses a series of plates to impact aerosols while simultaneously separating particles by size. As particles travel down through the MOUDI due to the pull of a vacuum pump, air is forced around these centrally located impaction plates. Large particles with greater momentum are not able to follow the air stream and impact on higher stages. Higher numbered stages have both a smaller inlet and a shorter distance between the inlet and the impaction plate, making smaller particles unable to avoid impaction.[79]
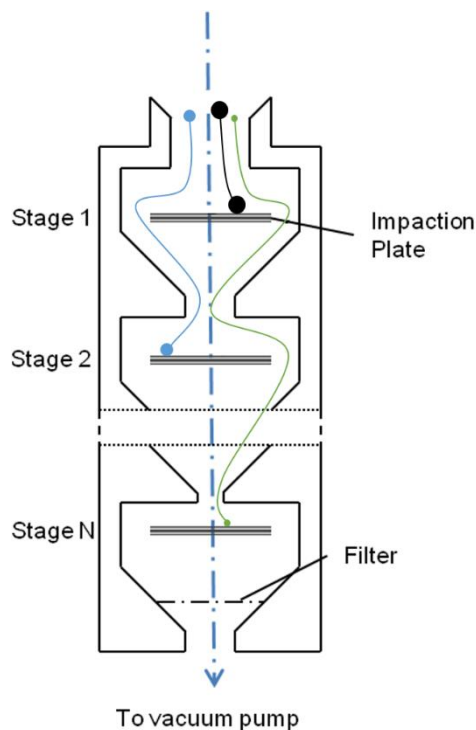
Figure 1.10 Schematic of a micro-orifice uniform deposit impactor (MOUDI).

To study morphology, especially of small particles (down to 0.01 μm), atomic force microscopy

(AFM) can be used to great effect. With this technique a small probe with a sharp tip is placed

in contact with a sample. The probe is then scanned across the sample and any deflection due to

particles on the substrate is recorded.[80] AFM is capable of detailed images of small particles but

used alone it lacks the ability to determine particle composition. Scanning electron microscopy

(SEM) and transmission electron microscopy (TEM) are two other techniques which can yield

high resolution images of small particles, although without the height detection that AFM has.[81]

Here electrons are focused and directed onto a sample where they are transmitted or scattered

back by particles on the substrate. TEM typically uses much higher accelerating voltages (200

kV vs 20 kV for SEM) for the electron beam and is done under vacuum with thin samples.[82]

These stipulations allow for greater resolution (down to 0.01 μm vs 0.1 μm with SEM) at the cost

of data acquisition time and sample preparation restrictions.[83] In order to measure elemental

composition in addition to morphology, energy dispersive X-ray spectroscopy (EDX or EDS) is often coupled to these two electron microscopy techniques. Here, as the energetic electrons impinge upon the sample, core-shell electrons may be ejected followed by the relaxation of other electrons into the now vacant core-shell orbital. This release of characteristic X-rays is measured with a dispersive energy detector (in order to detect X-rays at multiple energies simultaneously), producing an elemental spectrum. TEM can also be coupled with electron energy loss spectroscopy (EELS), where the difference between the energy of the initial electron beam and the energy of the scattered electrons are measured.[84-85] The energy of incoming electrons can be partially transferred (inelastic scattering) to the sample based on elemental absorption edges or molecular absorption peaks.[86] Similar elemental and molecular information can be obtained using scanning transmission X-ray microscopy coupled with near-edge X-ray absorption fine structure spectroscopy (STXM-NEXAFS). Though the technique is the same, sometimes the acronym X-ray absorption near-edge spectroscopy (XANES) is used, with NEXAFS being more popular with the soft X-ray regime (to study elements like C, N, and O) and XANES being more common with hard X-rays (to study transition metals like Pb, Zn, or Fe). This technique uses a focused beam of monochromatic X-ray light to take images of a sample at multiple energies near or around an element's absorption edge. Not only is this technique quantitative, but it can operate over a wide range of elements without some of the sample restrictions of TEM-EELS and without being as damaging to the sample.

1.3 X-ray Spectromicroscopy

1.3.1 STXM/NEXAFS. Considering the impact aerosol composition and the spatial distribution of its components can have on a particle's behavior, it becomes clear that individual particle measurements are vital to fully understand an aerosol population. Spectromicroscopic

techniques like STXM/NEXAFS and SEM/EDX are well-suited to this task. Because many aerosols are often carbonaceous in nature, carbon-edge STXM/NEXAFS can be especially powerful in determining organic composition and quantifying the organic fraction.

    1.3.1.1 The synchrotron. As the name suggests, STXM/NEXAFS measures X-ray absorption through a sample. While various methods exist to generate X-ray radiation, no currently existing method can produce X-ray light as bright as synchrotrons can. The concept for building what we now call a synchrotron was independently developed in 1945 by Vladimir Veksler and Edwin McMillan, whose discovery led to the construction of the first 70-MeV facility by General Electric in 1947.[87] Today there are over 50 synchrotron facilities around the world with operating energies in the GeV range.

    Synchrotron operation (as shown in Figure 1.11) begins with the production of electrons from an electron gun. A cathode (often made from barium or strontium compounds) is heated to produce electrons via thermionic emission. These electrons are then pulled towards a circular anode, directing a beam of electrons into the linear accelerator (linac for short). In order to separate the electron beam into discrete bunches, and to accelerate them, a series of hollow cylindrical electrodes are positioned along the axis of the electron beam. A strong oscillating potential is applied to alternating electrodes so that, along the axis of the beam, electrons are pulled towards the electrode in front and pushed forward by the electrode behind.[88] Linear accelerators in synchrotrons have many of these electrode pairs in order to accelerate the electrons to relativistic speeds before they are directed into the booster ring. The booster ring acts as an extension of the linac, continually accelerating electrons with strong radiofrequency (RF) pulses until they are speeding along at 99.999985% the speed of light.[89] Once the electron bunches have been sufficiently accelerated, they are directed into the storage ring where their

energy is maintained by additional RF pulses. The RF pulses which accelerate the electrons are timed so that electron bunches pass through the RF cavities at the midpoint of an RF pulse. This synchronization of accelerating pulses gives the synchrotron its name and is what separates it from the previous cyclotron models.
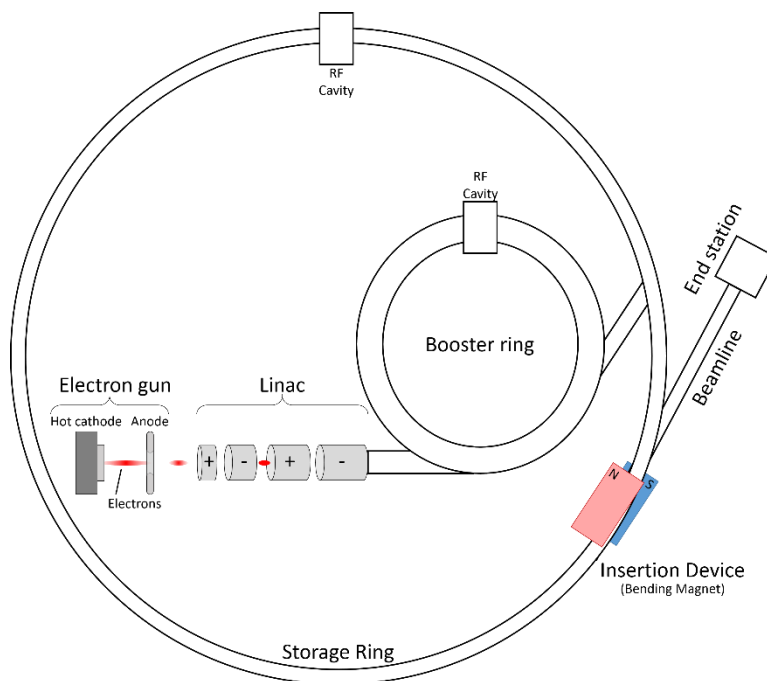
Figure 1.11 Schematic of a synchrotron.

To produce the bright X-ray light that is used in experiments, electrons in the storage ring pass through various insertion devices installed around the ring. Insertion devices are magnets (or sets of magnets) which act upon the moving electrons, causing them to emit synchrotron radiation. Two types of insertion devices are commonly used: undulators and bending magnets. Bending magnets are the simplest insertion device, consisting of a single north and south pole pair positioned across the axis of the beam. This produces light with a broad range of energies which are then narrowed down using beamline optics (like a monochromator). Undulators, on

the other hand, consist of alternating sets of magnets with a carefully tuned spacing between each set. This arrangement results in constructive and destructive interference of the emitted X-ray light, producing harmonics. These harmonics are much brighter and produced with a much narrower spectrum of light than bending magnets or wigglers, though the magnet spacing needs to be re-optimized if one wishes to change the energy of the emitted light.

1.3.1.2 The STXM instrument. After X-ray light is emitted from the electrons interacting with the insertion device it is directed down a series of mirrors and optics towards the experimental station. Figure 1.12 shows a schematic of some of the main optics used in a STXM beamline. Starting with the insertion device, the light is directed towards a grating monochromator which fans out the different energies of incoming light. This monochromator is able to be rotated in order to choose specific energies as needed. Then a thin beam of this fan is selected using a set of movable slits to ensure only a narrow spectrum of energies is used in the experiment. After energy selection the light is focused by a Fresnel (pronounced "fruh-nel") zone plate, first passing an order sorting aperture (OSA) to remove unwanted light. The focused light impinges upon the sample which can be scanned to produce an image. Lastly the transmitted light is collected by an X-ray detector located behind the sample.
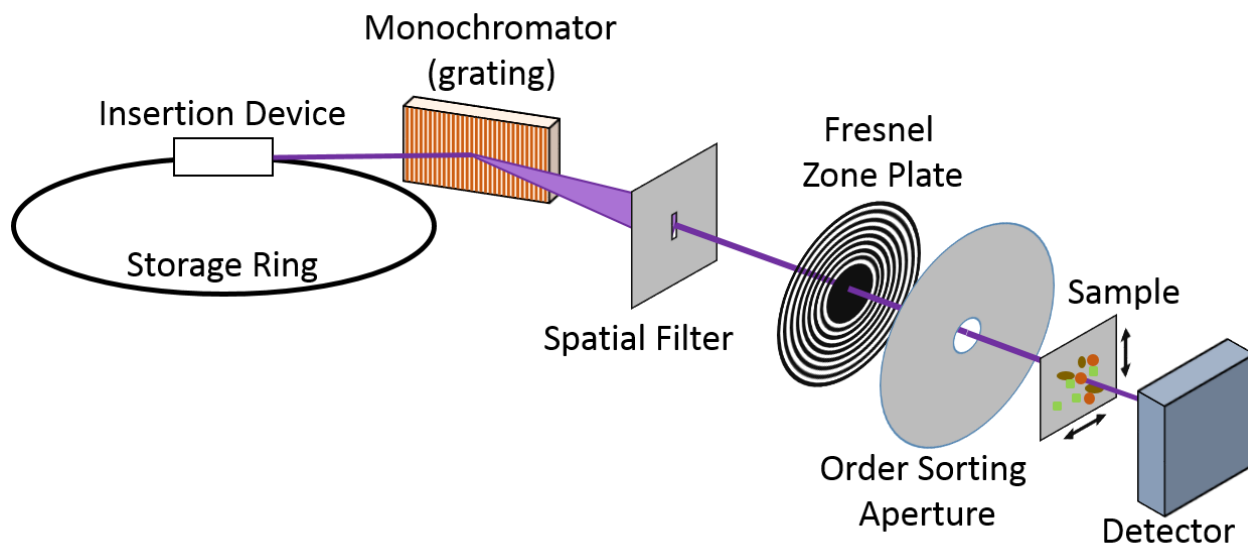
Figure 1.12 Schematic of STXM beamline.

The use of a Fresnel zone plate is necessary because at soft X-ray energies, most materials have a refractive index near (or less than) one, making traditional refractive optics difficult.[90] Fresnel zone plates are essentially transmissive circular diffraction gratings, producing multiple focused fringes as seen in Figure 1.13. Zone plates used in STXM instruments are around 200 μm and composed of zones approximately 40 nm wide at the edges. To remove the higher order (and less intense) fringes, an OSA is used which consists of a small pinhole that lets only the brightest first order light through.
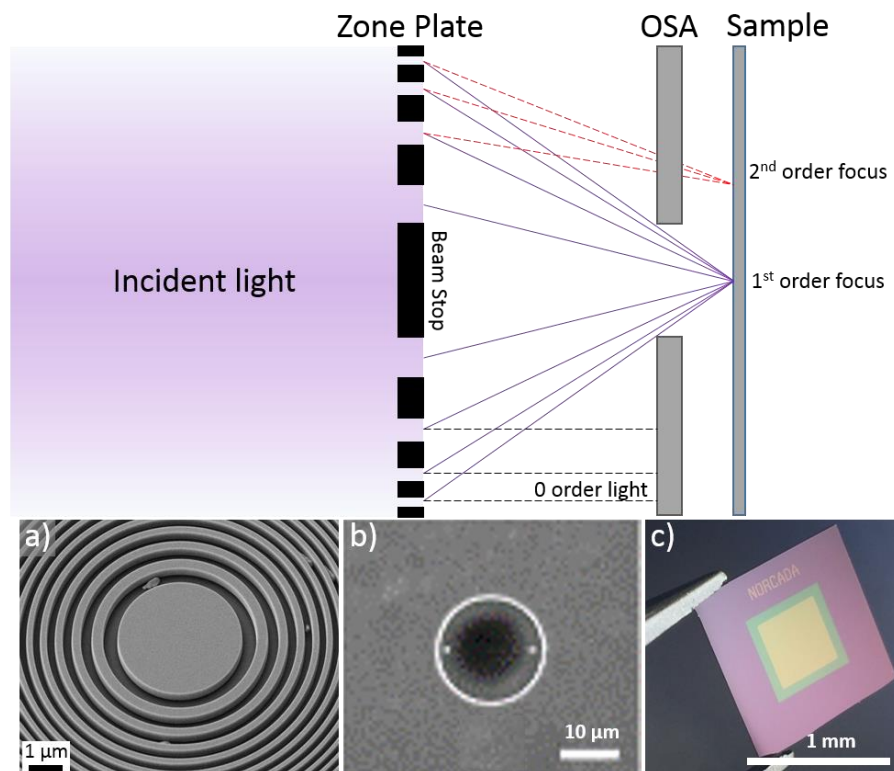
Figure 1.13 Schematic of zone plate and order sorting aperture (OSA). Incident light is diffracted with the zone plate and the first order light is focused (purple lines) while higher order light is blocked by the OSA. Zero order (undiffracted) light is blocked by the central beam stop and the OSA. Shown below are examples of the components: a) zone plate, b) OSA, c) sample substrate (Si_3N_4 silicon nitride window).

The result of the above engineering is the ability to take absorption measurements at a small point (down to ~25 nm) using light at a specific energy. Images are produced by raster scanning the sample over a region of interest. Two sets of horizontal and vertical stages are used to accomplish this, a set of stepping motor stages (coarse stages) with a large range of motion and a set of piezoelectric stages to control sub-micron motion (fine stages).[91] When an area with aerosols is found using the coarse stages, a region of interest (usually a 15 x 15 μm) is identified. The fine stages move the sample so that the incident beam is focused on the lower corner of the region. A raster scan is then taken, where the fine stages move the sample horizontally to collect the bottom row of data points before moving up a point vertically to collect the next row. Taking images in this way alone defines STXM as a microscopy technique. NEXAFS refers to the

collection of multiple images over the same region of interest, with each one image being taken at a different energy. These images are usually collected around an element's absorption edge; for example, images of carbonaceous aerosols are taken between 278 and 320 eV to capture the entire carbon 1s absorption edge (also called the K-edge). Generally, two types of data are collected depending on the number of energies used across a given absorption edge. When the objective is to capture the detailed spectral features of an absorption edge, anywhere from 60 to 200 images can be taken. Collections of images taken this way are referred to as a "stack" and contain a full carbon absorption spectrum for each pixel of the stack, an example of this is shown in Figure 1.14 below. Alternatively, one can take images at only a small number of energies (fewer than 10) with each image corresponding to an important absorption energy. The purpose being to create a map of the spatial distribution of the components represented by the chosen absorption energies, and so these collections of images are referred to as "maps".

When X-rays with energies near an element's absorption edge are absorbed by a sample, electrons in core orbitals are excited to unoccupied molecular orbitals. Figure 1.14 depicts how these changes in core electron energy levels result in an absorption spectrum, allowing STXM/NEXAFS to ascertain molecular functionality with elemental specificity. Typically, this technique is used with low Z elements like C, N, and O, though heavier elements can be probed. Focusing on low Z elements is ideal for aerosols because many of them are either carbonaceous or have a carbonaceous coating. As long as an element has an absorption edge accessible by the energy range defined by the individual instrument, it can be used to perform STXM/NEXAFS. The K-shell absorption edge is used for light elements and is generally preferred as absorption features are sharpest here. For heavier elements, especially transition metals, L or even M absorption edges can be used as the K-edge is often too high in energy for most soft X-ray

beamlines; however, spin-orbit coupling and broader or less intense absorption edges can make the analysis much more difficult here.[92]
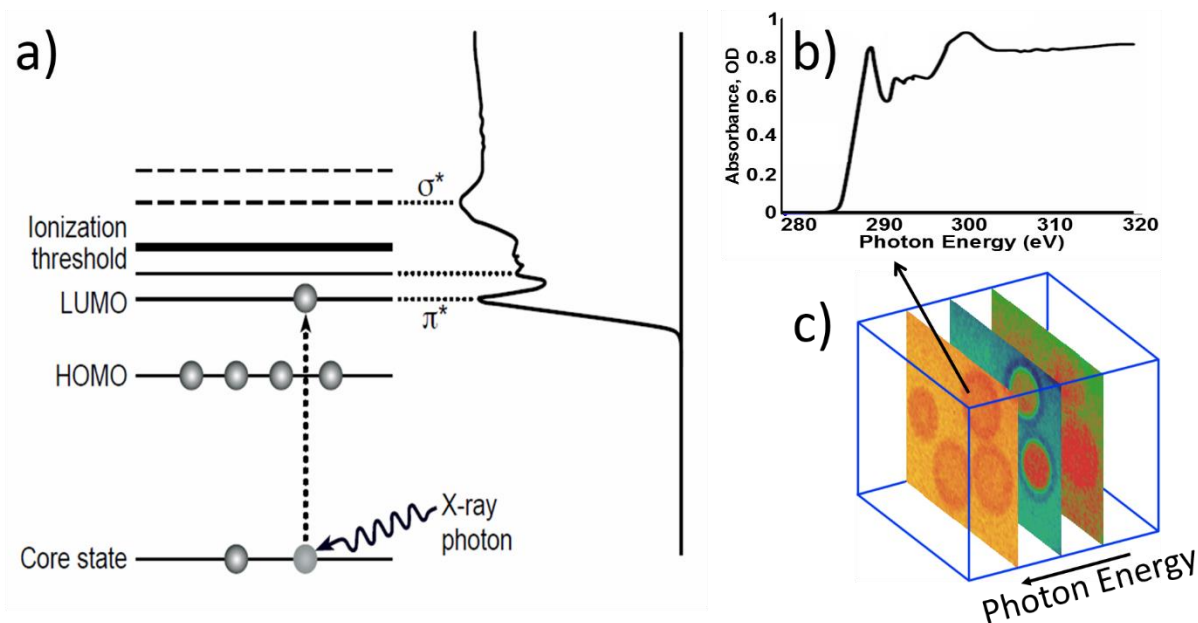
Figure 1.14 Example energy level transitions for STXM/NEXAFS and stack image. a) X-ray photon absorption exciting a core (1s) carbon electron into unoccupied molecular orbitals. b) Rotated absorption spectrum showing how energy level transitions result in spectrum. c) Representation of a "stack", arrow shows the spectrum in b) being retrieved from a single pixel. Images reproduced with permission from Moffet, *et al.* 2010.[93] Copyright 2010 Taylor & Francis.

1.3.2 SEM/EDX. Scanning electron microscopy is another microscopy technique which uses electrons instead of X-rays to image a sample (Figure 1.15 gives a schematic of the major components). Because the effects of diffraction are much less pronounced with electrons, electron microscopy can achieve greater spatial resolution (around 10 nm).[83] A drawback to this technique, at least compared to STXM, is that the electrons used here are more energetic than the X-rays used in STXM and so can easily damage samples making them unfit for further analysis. With this technique, electrons are emitted via thermionic emission from an electron gun. Unlike the electron gun used in a synchrotron (which is a 1 cm^3 chunk of material),[94] the emitter

material is usually fashioned into a fine tip or point which can be 100 nm or smaller.[95] The

smaller the region that electrons are emitted from, the smaller the resulting electron beam which

improves spatial resolution. From here the electrons are accelerated and focused using sets of

electromagnetic lenses. To produce an image, the electron beam is raster scanned over a

stationary sample, differing from how STXM images are produced. When the electron beam

impinges upon the sample many possible interactions can take place. The incoming electrons

can be scattered at shallow angles and be transmitted through the sample, they can be scattered

back towards the source (aptly named backscattered electrons), or they can impart their energy to

an atom causing it to eject core electrons (called secondary electrons).
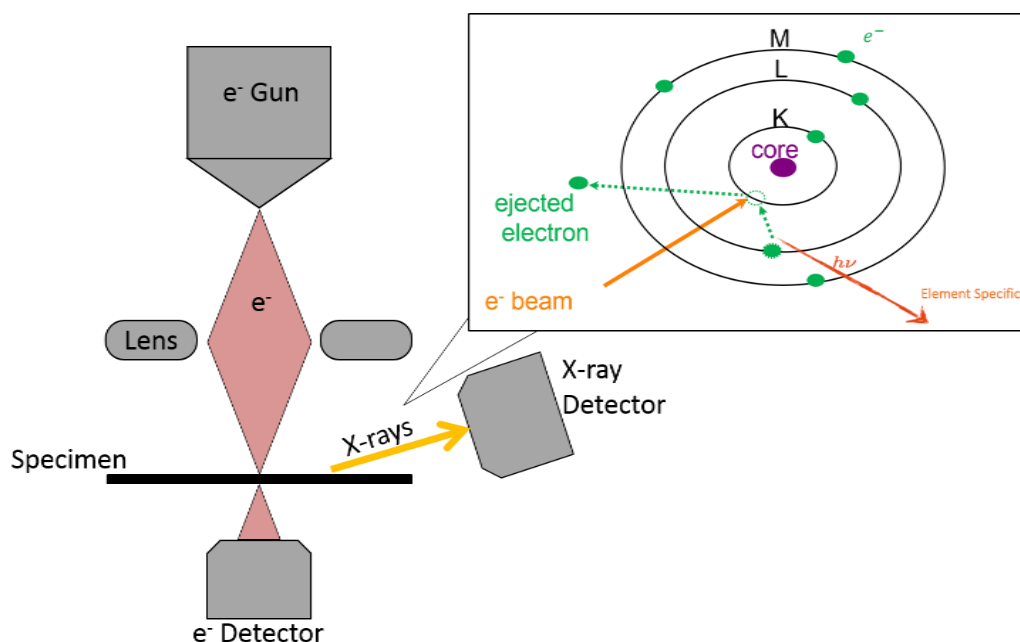
Figure 1.15 Schematic of an SEM with EDX. Inset image depicts EDX emission process.

When these secondary electrons are ejected, the vacancy left behind can then be filled by

a relaxing electron from a higher orbital. From this relaxation characteristic X-rays are

produced. Because each released X-ray is caused by an energy level transition within a single

atom, the wavelength of X-ray light produced is indicative of the element producing it. Energy

dispersive X-ray spectroscopy (EDX or EDS) takes advantage of these characteristic X-rays and

is often coupled with SEM. When the electron beam interacts with the sample, all of the

characteristic X-rays are produced simultaneously. In order to separate the intensity of light by

wavelength (and therefore by element), an energy dispersive detector is placed at a shallow angle

with respect to the sample plane to collect the emitted light.

     1.3.3 XRF/XANES. X-ray fluorescence (XRF) spectroscopy shares many similarities

with STXM, from the need for a synchrotron facility to the way the beamline is setup. While

STXM/NEXAFS is able to collect images and spectra for elements like C, N, and O and lighter

metals like the first row transition metals, heavier elements are inaccessible or not well-suited for

this technique. These heavier elements have core-shell binding energies too high to be easily

accessed (Pb's K-edge is at 88000 eV) or, for absorption edges that can be reached, the

absorption edge can be too broad or the absorption cross section may not increase enough

between pre- and post-edge.[92]

     The XRF beamline used here was the submicron resolution X-ray (SRX) beamline at the

National Synchrotron Light Source II (NSLS-II) located in Brookhaven National Lab (BNL) on

Long Island, New York. A schematic of the beamline is shown in Figure 1.16 below. With XRF

spectroscopy much more energetic X-ray light is used compared to STXM, often measured in

keV rather than eV. The incident light used for the work presented here was approximately 13

keV, selected to provide the best contrast for Pb particles. Here, when the X-ray light from the

synchrotron reaches the sample it is able to eject inner shell electrons. Just like with EDX, a

higher orbital electron can then relax and fill the newly created hole which is then detected with

a dispersive energy detector. The result is a spectrum comprised of the fluorescence signals from all elements with electrons in orbitals having a binding energy lower than the incident X-ray energy.96 A caveat to this, however, is that XRF is best suited for heavier elements. Although light elements like C, N, and O certainly have ionizable electrons with a low enough binding energy, the fluorescence yield for these elements is low.92 This means that more sample is needed to produce a strong enough fluorescence signal. XANES, as mentioned above, is identical to NEXAFS with the two names being popular in the hard or soft X-ray community respectively.
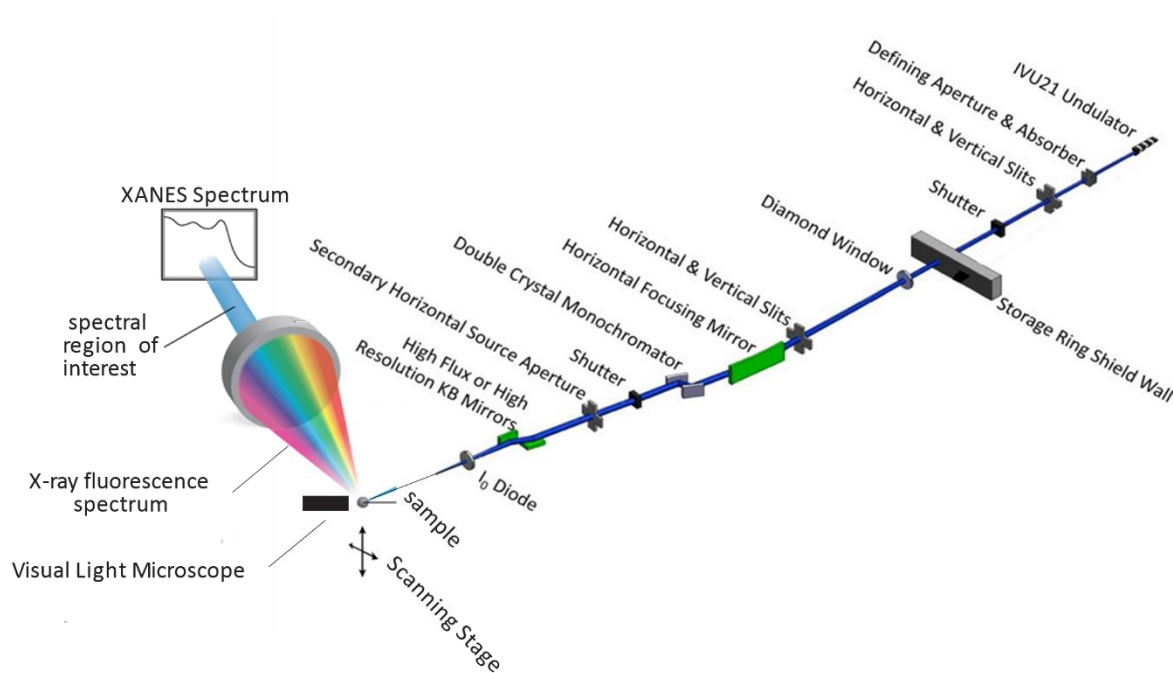
Figure 1.16 Schematic of the SRX beamline.

1.4 Image Processing and Analysis

1.4.1 Raw data processing. Whether taking a few images to create a map or taking

multiple images for a stack, deciding which energies to collect data at is important. Most of the STXM/NEXAFS analysis done for the current work involves the carbon K-edge and so examples and specific energies mentioned will be for carbon unless otherwise specified. In order to measure how much absorption at a given spot is due to a specific element, a pre-edge image is always taken. This is usually taken at a low enough energy that it is not affected by any of the element's absorption features, or any pre-peak features that may be present. For carbon, the absorption edge begins at 284.2 eV and pre-edge images are taken at 278 eV. The simplest of maps are composed of just two images, this pre-edge image and a post-edge image, to measure how much of a given element is present and where it is located. Like the pre-edge, post-edge images are best taken far enough away from the absorption edge and any other absorption features, this is usually 320 eV for carbon. To glean additional information from these maps, two extra images are often taken corresponding to ubiquitous carbon features.

Before the raw data is used, however, some pre-processing is needed. When a sample is ready to be imaged, shutters are opened to expose the X-ray light. Any beamline elements (as well as the sample) will be heated by the incoming radiation, causing some amount of thermal expansion and can result in particles drifting over the course of data acquisition. Vibrations or accidentally hitting the instrument enclosure can also cause tiny shifts at the small length scales involved. To fix this, a Fourier transform based alignment routine is performed to ensure particles are in the same position in each of the images. Here, translations between individual images are represented by simple shifts frequency space. This method also can identify translations on a sub-pixel level and works well even with noisy images, making it ideal for these images. The present work uses an optimized algorithm developed by Guizar-Sicairos to reduce computation time.[97] After image alignment is complete, an average intensity image is calculated

for the purpose of identifying particles. A gamma correction factor is first applied to this average image to improve the detection of small, faint particles and of any thin coatings on the edges of particles. This involves each of the normalized pixel intensities being raised to an exponent (named gamma, γ) and usually a single value is used for a given data set, anywhere between 2 and 15. After this image enhancement, the particle detection algorithm called Otsu's method is performed.[98] Otsu's method takes a grayscale image (like an intensity image) and separates the image into two groups using a threshold value, or in this case a threshold intensity. The optimal threshold is based on minimizing the variance within each of the two groups. When the variance within each group (called the intra-class variance) is minimized the intensity values within each class of pixels are the most similar. For images of aerosols on blank substrates these two classes of pixels are "particle" and "background".

At this point the raw intensity images are transformed into optical density (OD) using the Beer-Lambert law seen in Equation 1.3 below.[99]

$$OD = -\ln\left(\frac{I}{I_o}\right) = \mu\rho t \tag{1.3}$$

Here, I is the intensity of the transmitted light, I_o is the intensity of the incident light, μ is the mass absorption coefficient (usually in units of cm^2 g^{-1}), and t is the thickness of the sample. Because aerosols are often collected on a substrate which will have some incidental absorption, in practice I_o is the light transmitted through the portions of the substrate without particles or the background pixels. The use of the Beer-Lambert law highlights a strength of the STXM/NEXAFS technique in that it is a quantitative technique. Table 1.1 below gives a few values for μ at the carbon pre- and post-edge (278 and 320 eV respectively), note the small changes for N and O compared to C.

Table 1.1 Select mass absorption coefficient (μ) values.

Element	Mass absorption coefficients ($cm^2\,g^{-1}$)	
	(278 eV)	(320 eV)
C	1900	39500
N	3700	2500
O	6000	4200

1.4.2 Carbon speciation mapping. In addition to the pre and post image, which is standard practice for taking maps over any elemental absorption edge, images at additional energies can be taken at important absorptions to give maps more detail. Moffet, *et al.*, 2010 describes a mapping procedure able to speciate soot, organic, and inorganic carbon with the use of 4-energy maps.[100] For carbon the absorption peak at 285.4 eV is due to the 1s $\rightarrow \pi^*_{C=C}$ transition. While double bonds in organic compounds are common, because soot contains so many sp^2 hybridized C-C bonds a large peak at 285.4 eV can be indicative of soot. The % sp^2 hybridization is calculated by taking the ratio between the 285.4 eV peak area of a sample with that of pure highly-ordered pyrolytic graphite (HOPG) which represents 100% sp^2 bonding. Empirical observations have shown that a % sp^2 value of 35% or higher is consistent with ambient soot observations.

To identify organic and inorganic regions the pre- and post-edge images are used. Any absorption at the pre-edge at 278 eV is due to small contributions from all elements present. Absorption at the post-edge at 320 eV is mainly the result of carbon absorption; any absorption contributions from other elements remain fairly constant over this range. A ratio between the OD at the pre-edge and the OD at the post-edge will then show what fraction of the total

absorption is due to carbon. The paper by Moffet, *et al.* 2010 calculated OD_{pre}/OD_{post} ratios for 7 different inorganics while assuming a wide range of organic to inorganic thickness ratios.[100] Adipic acid was used as a representative organic, though varying the assumed organic will only change results slightly as the densities and absorption coefficients are similar for reasonably representative organics. The paper found that when the inorganic component was thicker than the organic component, the OD_{pre}/OD_{post} ratio was greater than 0.5. Using this value as a threshold, any pixels greater than 0.5 are deemed inorganic dominant, while any other pixels are labeled organic dominant. Note that there still may be organics in these inorganic dominant regions, especially if the OD_{pre}/OD_{post} ratio is near 0.5.

After these threshold values are calculated the carbon speciation maps are assembled according to a hierarchy on a pixel-by-pixel basis. First, if a pixel has a % sp^2 hybridization greater than 35%, it is labeled as a soot pixel regardless of its OD_{pre}/OD_{post} ratio. The peak area comparison with HOPG is a more specific and robust condition than those for inorganic or organic pixels and so it is given priority. Next pixels are separated into inorganic and organic dominant using the OD_{pre}/OD_{post} ratio of 0.5. Because this ratio was determined to be a good value when the inorganic is not known, the inorganic/organic thresholding can be improved if the inorganic has been previously identified or is known from other experiments. Figure 1.17 shows an example of a carbon speciation map along with the spectra from each of the three components within a specific particle. Notice how the red soot spectrum has a much higher absorption peak at 285.4 eV compared to the other two and how the inorganic spectrum shows much less overall absorption than the other spectra. The inorganic spectrum still has defined absorption peaks, again emphasizing these regions as inorganic dominant rather than exclusively inorganic.
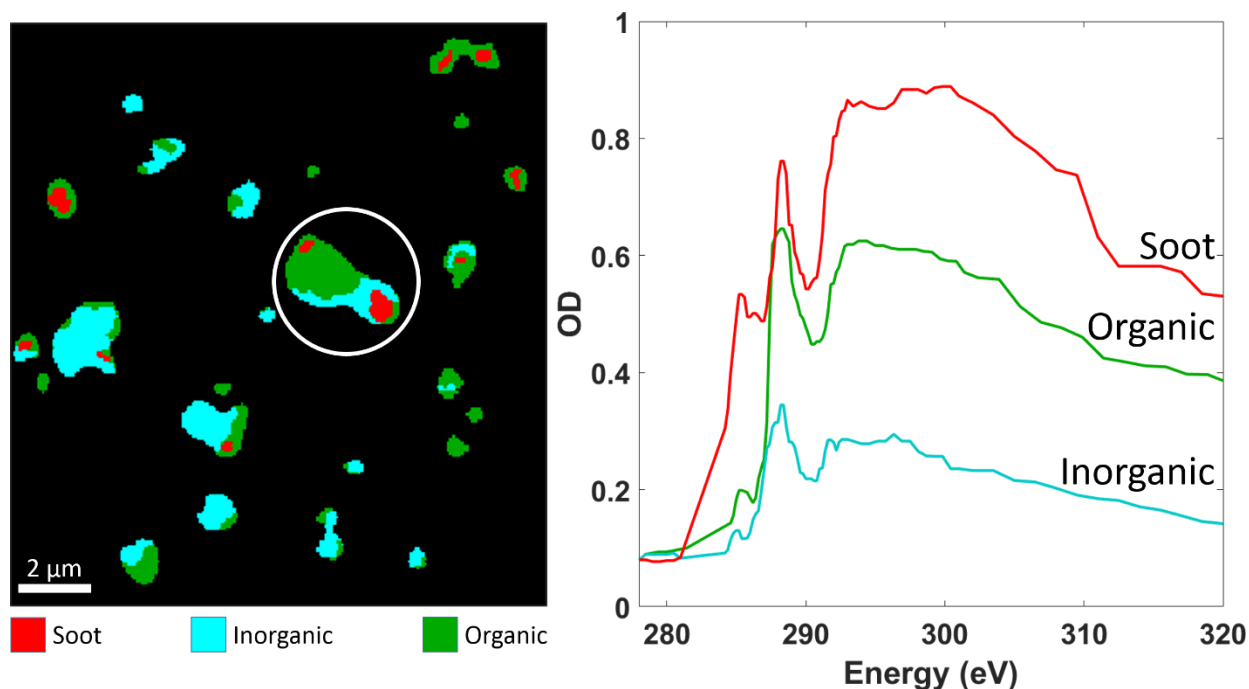
Figure 1.17 Example C speciation map and component C spectra. (left) Carbon speciation map. (right) Carbon spectra of the three components of the circled particle. Each component spectrum was calculated from the average spectrum of all pixels of the given component within the circled particle.

1.5 Direction of Dissertation

The chapters within this dissertation focus on the application of X-ray spectroscopy to aerosol samples. Single-particle spectromicroscopic techniques are powerful tools that can help improve our understanding of aerosol populations, atmospheric or otherwise. The combination of high resolution images with composition information comes closer to describing how these particles interact in their native environments than either aspect alone does. As climate becomes more and more of a critical public issue, advancing our understanding of all aspects of climate becomes increasingly important.

To this end, these spectromicroscopic techniques have been applied to aerosols from three different field studies in vastly different locations and for different purposes. Particles from the Amazon were collected to investigate anthropogenic influences of a large city on some of the most pristine environment left on the planet. New particle formation was investigated in

the rural plains of Oklahoma which could have a measurable effect on the absorption of solar radiation on days after it rains, meaning these particles may need consideration in future atmospheric models. Lead particles originating from garbage burning were observed in Mexico City and analyzed to determine what species of lead or lead salts were present. With the dangerous neurological effects lead can have, especially on children, the identification of the specific type of lead, its solubility, and its bioavailability is necessary to protect the people affected by it. Presented here is also a look into the quantitative capabilities of STXM/NEXAFS to calculate mass as well as volume and volume fractions with the use of laboratory-generated particles. There are many more ways in which these techniques can be used and just as many ways for improvements to data processing and analysis.

Chapter 2: Quantitative Capabilities of STXM to Measure Spatially Resolved Organic Volume Fractions of Mixed Organic / Inorganic Particles

2.1 Synopsis

Scanning Transmission X-ray Microscopy coupled with Near-Edge X-ray Absorption and Fine Structure (STXM/NEXAFS) spectroscopy can be used to characterize the morphology and composition of aerosol particles. Here, two inorganic/organic systems are used to validate the calculation of Organic Volume Fraction (OVF) and determine the level of associated error by using carbon K-edge STXM data at 278.0, 285.4, 288.6, and 320.0 eV. Using the mixture of sodium chloride and sucrose as one system and ammonium sulfate and sucrose as another, three solutions each were made with 10:1, 1:1, and 1:10 mass ratios (inorganic to organic). The OVF of the organic rich aerosols of both systems deviated from the bulk OVF by less than 1%, while the inorganic rich aerosols deviated by approximately 1%. Aerosols from the equal mass mixture deviated more (about 4%) due to thick inorganic regions exceeding the linear range of Beer's Law. These calculations were performed after checking the data for image alignment, defocusing issues, and particles too thick to be analyzed. The potential for systematic error in the OVF calculation was also tested by assuming the incorrect composition. There is a small (about 0.5%) OVF difference if the organic is erroneously assumed to be adipic acid rather than the known organic, sucrose. A much larger (up to 25%) difference is seen if sodium chloride is assumed instead of ammonium sulfate. These results show that the OVF calculations are fairly insensitive to the choice of organic while being much more sensitive to the choice of inorganic.

2.2 Introduction

Atmospheric aerosols are airborne mixtures of solid and liquid phase components such as soot, inorganic salts, trace metals, and organics.[1] These aerosols have been shown to cause

detrimental health effects upon inhalation and can negatively impact visibility, especially around large cities.[101] In addition, aerosols currently represent the largest source of uncertainty in radiative forcing from anthropogenic sources according to the 2013 Intergovernmental Panel on Climate Change (IPCC) report.[4] Two of the main ways in which aerosols can affect radiative forcing are through aerosol-radiation interactions (also known as the "direct effect") and aerosol-cloud interactions (also known as the "indirect effect"). One of the limitations on the predictive power of global climate models is the dependence that aerosol cloud interactions have on individual particle composition.[102] Because the complex and varied compositions of aerosols are linked to their impacts on health and the environment, quantitative characterizations of detailed aerosol chemical and physical properties are necessary.

Many methods exist for quantifying the bulk composition of an aerosol sample both in real time ("online") or offline. Offline analysis is most commonly achieved by analysis of filter sample deposits. Characterization with filter samples benefit from a large body of literature detailing standard operating procedures along with a variety of compatible analysis methods.[103] Depending on the filter type and composition, a limited elemental analysis can be conducted using, for example, Proton Induced X-ray Emission (PIXE) or Inductively-Coupled Plasma with Atomic Emission Spectrophotometry (ICP-AES).[56-57] While these methods are highly accurate and precise, they often cannot offer the possibility of quantifying the lighter elements (C, N, O) which often make up the majority of the accumulation mode aerosol. Online bulk analysis is most often accomplished with relatively complex automated instruments. Thermo-optical analysis is regularly performed and has well established protocols for quantitatively determining fractions of Organic Carbon (OC) and Elemental Carbon (EC).[62] The Aerosol Mass Spectrometer (AMS) and the related Aerosol Chemical Speciation Monitor (ACSM) are real-

time instruments which can be operated *in situ*, allowing for aerosol events and plume evolution to be studied.[64] Heavier elements (Al and higher) can be measured in real-time with a portable X-ray Fluorescence spectrometer with low detection limits (<40 ng/m^3).[104] Laser-Induced Breakdown Spectroscopy (LIBS) is able to detect light and heavy elements down to low ppm-levels in real-time, however shot-to-shot variation hampers this techniques quantitative capabilities.[67-69] Although many of these quantitative techniques have well defined methods along with, in some sampling locations, long historical records, bulk measurements cannot easily study particle-specific qualities of aerosols.

The challenge of characterizing the composition and source variation within aerosol populations highlights the necessity for quantitative measurement techniques that can determine particle-resolved composition. Many of these techniques are also *in situ* and time-resolved, like the Soot Photometer (SP2) which measures black carbon and any associated coating by way of incandescence and scattering.[73-75] Like its counterpart, the Single Particle Aerosol Mass Spectrometer (SP-AMS) can also provide *in situ* and time-resolved composition but it does so for individual particles.[105] Single particle laser desorption instruments like the Single Particle Laser Ablation Time-of-flight (SPLAT) mass spectrometer and the Aerosol Time-Of-Flight Mass Spectrometer (ATOFMS)[76-77, 106] have been used to obtain particle information about particle composition. Other single particle parameters of interest, like optical properties and particle density, are able to be calculated from ATOFMS data as well.[78] On-line techniques like these provide useful size and composition information but cannot easily probe the detailed morphology, quantitative single particle composition, or spatially-resolved composition of aerosol particles; for this, microscopic and spectromicroscopic techniques may be better suited. Although microscopy measurements can carry more stipulations (substrate effects,[107] sample

storage considerations, analysis time, and sometimes large infrastructure requirements), techniques like Scanning Electron Microscopy (SEM), Transmission Electron Microscopy (TEM), Atomic Force Microscopy (AFM), and Scanning Transmission X-ray Microscopy (STXM) can distinguish and classify individual particles or regions therein based on morphology.[83]

In addition to morphology, spectroscopic techniques can be combined with some types of microscopy to study particle composition. For example, high spatial resolution of TEM can be combined with both Energy Dispersive X-ray spectroscopy (EDX, also EDS) and Electron Energy Loss Spectroscopy (EELS) to obtain elemental information about internally mixed particles.[108] Nanoscale Secondary Ion Mass Spectrometry (NanoSIMS) has also been applied to aerosol studies, often as a complementary technique to electron microscopy and EDX.[109] This technique can be used to study carbonaceous aerosols[110] as well as metal-rich aerosols[111] and is able to provide composition as a function of depth. Another example of a combined spectromicroscopic technique is STXM, which can be coupled with Near-Edge X-ray Fine Structure spectroscopy (STXM/NEXAFS). This retrieves quantitative elemental composition on a per-particle basis and is well suited for the analysis of C, N, and O. With a spatial resolution of ~30 nm and a spectral resolution of ~150 meV,[91, 112] STXM can identify the elemental composition of distinct regions within a particle. From this (along with component density) an Organic Volume Fraction (OVF) can be calculated, which can be used to characterize hygroscopicity and has been used in part to quantify the effects of biological activity of laboratory generated sea spray aerosols.[37] Heavier elements can be difficult to measure in tandem with C, N, and O while using STXM, which has an energy operating range defined by the synchrotron and the design of the STXM. However, heavier elements such as Na and higher

can be quantitatively measured using SEM coupled with EDX.[113] These two techniques have previously been used in combination on the same set of particles in order to retrieve an elemental composition that is both quantitative and includes lighter and heavier elements.[114-115]

The presence of an organic component within aerosol populations is important in determining their reactivity and hygroscopic behavior. The amount of organics, and their distribution throughout an aerosol, can affect the reaction rates and equilibrium positions of some heterogeneous reactions.[116-117] Organics can also affect the ability for an aerosol to serve as both cloud condensation nuclei (CCN) or ice nucleating particles (INP).[118-120] Because of the vital role that organics play in affecting aerosol behavior, specifically the effects organics have in changing an aerosol's hygroscopicity, the OVF is used as key piece of data feeding into κ-Köhler theory.[121] The use of STXM to spatially resolve carbon species in aerosols has been reported since the early 2000s.[91, 122] An automated method for producing spatial maps of these aerosol components was presented in 2010.[100] The method was further refined in 2016[107] where the use of carbon maps with only 4 energies was introduced to increase the number of particles analyzed, thereby improving particle population statistics. The quantitative capabilities of this 4 energy mapping method are discussed in the current work by comparing the experimentally determined OVF of two known solutions. Also discussed are the quality control measures necessary to ensure quantitative data, along with the potential for error should they be omitted. Lastly, the uncertainty introduced from assumptions made during OVF calculations was examined. To accomplish this, two systems of inorganic and organic mixtures were studied, each with three formulations of differing inorganic to organic ratios.

2.3 Materials and Methods

2.3.1 Standard preparation. Standard 100 mL solutions of NaCl/Sucrose and

$(NH_4)_2SO_4$/sucrose mixtures were prepared according to Table 2.1. Standard grade (Sigma-

Aldrich, >99% purity) material was weighed using a recently calibrated analytical balance

(Torbal, AGN200C) with an accuracy of $\pm$ 0.0001g. The powder was quantitatively transferred

into a 100 mL volumetric flask ($\pm$ 0.1 mL) which was then filled with room-temperature

Millipore-filtered 18 MΩ distilled water, capped, and inverted to mix. All glassware and utensils

were washed and soaked in a nitric acid bath overnight before use after which they were rinsed

with the 18MΩ water and left to air-dry.

Table 2.1 Calculated masses of each compound needed to make 100 mL of solution. Measured masses in parentheses.

System		Inorganic (g)	Organic (g)
Sodium Chloride / Sucrose	10:1	1.5213 (1.5210)	0.1521 (0.1523)
	1:1	0.7327 (0.7325)	0.7327 (0.7328)
	1:10	0.1185 (0.1185)	1.1848 (1.1846)
Ammonium Sulfate / Sucrose	10:1	1.2742 (1.2748)	0.1274 (0.1273)
	1:1	0.6701 (0.6701)	0.6701 (0.6701)
	1:10	0.1167 (0.1165)	1.1672 (1.1673)

2.3.2 Sample production and collection.   After the solutions were prepared, the

aerosol generation apparatus in Figure 2.1 was assembled. Nitrogen gas at ~ 20 PSI (~140 kPa)

was fed into a Collison nebulizer (3 jet MRE, CH Technologies USA) which was filled with one

of the standard solutions. The aerosols first passed through an Erlenmeyer flask with a rubber

stopper and two stainless steel pieces of tubing in order to collect any large droplets that may

have been produced. This flask also had a HEPA filtered air inlet in order to maintain

atmospheric pressure and air flow rate. The still humid aerosols next pass through two 66 cm

long laboratory-made diffusion driers. The driers consist of a mesh cylinder (2 cm OD)

surrounded by a larger Plexiglas cylinder (9 cm OD) with the space between the tubes filled with

desiccant (Silica Gel). The dried aerosols are finally directed into a small 4-stage collision

impactor (Sioutas Personal Cascade Impactor #225-370, SKC, Fullerton, CA USA) which was

loaded with Si_3N_4 windows to collect the particles. The four stages had D50 size cuts at 2.5, 1.0,

0.5, and 0.25 μm. A small diaphragm vacuum pump was attached to the bottom of the impactor

to maintain an air flow of ~9 L/min.
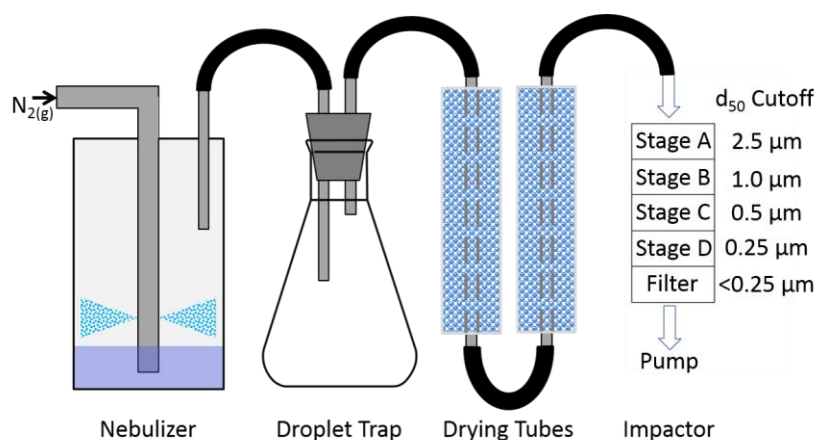
Figure 2.1 Schematic of laboratory-based aerosol generation setup. Running through the drying tubes are smaller, mesh tubes surrounded by silica gel desiccant (represented in blue).

2.3.3 STXM/NEXAFS data collection and analysis. Si_3N_4 windows were mounted to

an aluminum plate[91] to be imaged at the STXM beamline 5.3.2.2 at the Advanced Light Source

(ALS, Berkeley, CA, USA) as well as at the Canadian Light Source (CLS, Saskatoon, SK,

Canada). These STXM beamlines have an energy range of 250-780 eV (ALS) and 130-2700 eV

(CLS) which allows for the C K-edge to be studied. Soft X-rays were energy selected and then

focused to a ~30 nm spot size on the sample surface. A 15x15 μm region containing individual

particles was then selected and the sample stage was raster scanned using 40 nm steps. This

process was repeated at 4 different energies: A pre and post edge image was taken along with an

additional 2 images for C to allow for regions of soot, inorganics, and organics to be determined. The four energies near the carbon edge corresponded to the pre-edge, C=C, COOH, and post-edge regions (278.0, 285.4, 288.6, and 320.0 eV respectively).

These groups of images (collectively called a "stack") are first aligned with a method based on Guizar-Sicarios' image registration algorithm;[97] this ensures particle positions are constant throughout the stack. Once the stack is aligned, a gamma correction[123] is applied with each pixel's normalized intensity being raised to an exponent (a γ of 15 is used here) to modify the image contrast in order to detect small, faint particles. Otsu's method is then applied to this enhanced image which automatically differentiates between particles and background.[98] The intensity image is then transformed into an optical density (OD) image on a per-pixel basis using:

$$OD = -\ln\left(\frac{I}{I_o}\right) = \mu\rho t \qquad (2.1)$$

Where OD is optical density, I is the intensity of the given pixel, and I_o is the background intensity, μ being the mass absorption coefficient, ρ being the density, and t being the thickness of the given pixel.

The additional carbon edge images were used to determine carbon speciation according to previously developed algorithms.[100] With this algorithm, a series of thresholds are used to identify inorganic and organic dominant regions of each particle. These regions are differentiated based on their pre to post edge ratio OD_{278}/OD_{320}. Previous work has compared this pre to post edge ratio with the calculated thickness ratios of adipic acid and various inorganics. A pre to post edge ratio of 0.5 was selected as a general thresholding value when the identity of the inorganic isn't known.[100]

Carbon edge images were also used to calculate an organic volume fraction (OVF). This was done by first calculating the thicknesses of both the inorganic and organic components using a previously published method,[124] which is reproduced here. Knowing that the OD at each pixel is due to a mixture of inorganic and organic components, the following equations can be written:

$$OD_{278} = \mu^I_{278}\rho^I t^I + \mu^O_{278}\rho^O t^O \tag{2.2}$$

$$OD_{320} = \mu^I_{320}\rho^I t^I + \mu^O_{320}\rho^O t^O \tag{2.3}$$

With OD_E being the optical density at energy E, I and O representing inorganic and organic components respectively. The elemental mass absorption coefficients used here have been retrieved from previously published work.[92] By calculating and rearranging $OD_{320} - OD_{278}$ (taking $X^I = \mu^I_{320}/\mu^I_{278}$ for convenience) the thicknesses of the inorganic and organic components can be expressed as:

$$t^O = \frac{OD_{320} - X^I OD_{278}}{(\mu^O_{320} - X^I \mu^O_{278})\rho^O} \tag{2.4}$$

$$t^I = \frac{OD_{278} - \mu^O_{278}\rho^O t^O}{\mu^I_{278}\rho^I} \tag{2.5}$$

Mass absorption coefficients in accordance with published methods.[92] The densities of sucrose (1.59 g/cm^3), NaCl (2.16 g/cm^3), and (NH$_4$)$_2$SO$_4$ (1.77 g/cm^3) are used in this work. This study takes advantage of the *a priori* knowledge of the inorganic and organic compounds. For the sodium chloride/sucrose system, the mass absorption cross sections for sodium chloride and sucrose are calculated and their known densities are used for calculations. The same thing is done for the ammonium sulfate/sucrose system. Inorganic, organic, and total thickness maps can then be generated, and the OVF for each pixel (or each particle) can be calculated by taking the ratio of organic thickness to total thickness as shown in Figure 2.2.
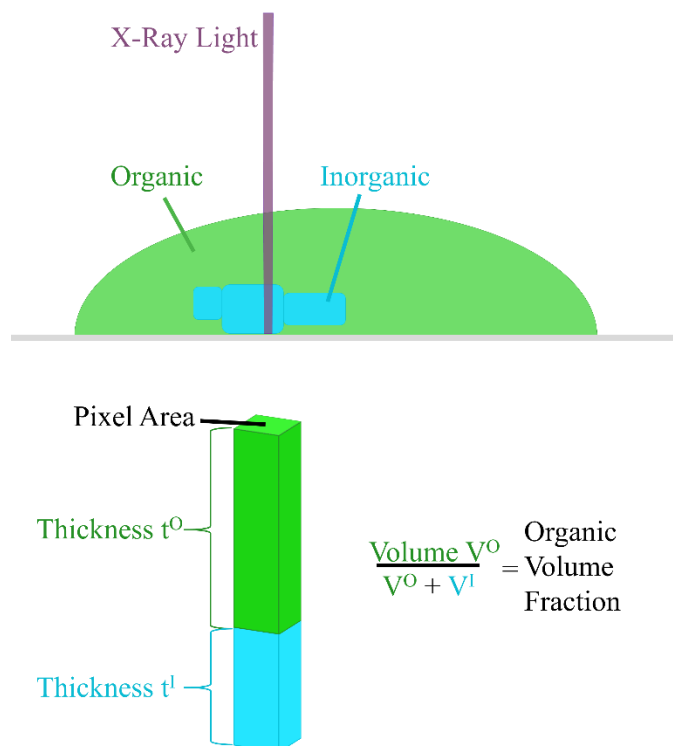
Figure 2.2 Visual of organic volume fraction (OVF) calculation. Shown is a 2 μm particle with a 30 nm beam spot size.

2.3.4 Quality control of processed images. In order to ensure quantitative results from this analysis, each data set was screened for any systematic errors that may have occurred during collection or analysis. The first screening step is to remove stacks with "defocusing issues" where the errors in the zone plate stage positioning result in a sample image that is not in focus. These defocusing issues occurred due to long term wear on the zone plate translation stage. When the sample is not at the focal point of the incoming X-rays, this increases the minimum spatial resolution of the instrument. This also results in unreliable particle morphologies, with many particles taking on a characteristic toroidal or "donut" shape, often seen in unfocused images. Along with major focusing issues, image stacks with a single, slightly defocused image must also be avoided. Field of Views (FOVs) with a single defocused image can present errors in mass determination and C species identification (soot, organic, or inorganic). This is

especially apparent near the edges of particles or inorganic cores where defocusing can blur these edges and, for example, misattribute inorganic pixels within an organic coating.

Following this, stacks were reviewed for proper alignment. This was checked by overlaying the aligned images and highlighting pixels which did not match. Any misalignment found was corrected manually before undergoing the automatic particle detection.

The image adjustment done on stacks prior to particle detection can introduce errors. On particularly noisy data a high gamma correction value can accentuate noise peaks causing them to be erroneously labeled as particles, often being only a few pixels wide. Gamma corrections which are too low can also cause the thinner, outer regions of particles to be ignored, instead only detecting the relatively thicker particle cores. Because of this, each FOV was visually inspected for correct particle detection and the gamma correction was adjusted accordingly between $5 \leq \gamma \leq 15$. In addition, a filter was applied after particles are detected which discounts any particles less than 8 contiguous pixels. Detected particles which were cut off by the edge of the image frame were also removed from analysis. An exception was made for particles where only a small portion (less than 8 pixels) appeared to be out of the frame, which were identified manually. These particles were not removed in order to improve particle statistics at the expense of a small error in accuracy.

A final correction was made on any pixels which had an OD >1.5, which is outside of the linear range of Beer's law where Eq. (2.1) is no longer valid. [93, 125-126] These pixels are from thick/dense regions of the particle, often being from the particle's inorganic center. Because the high OD regions tend to be inorganic cores, and due to the prevalence of cubic NaCl crystals in atmospheric aerosols, the regions are treated by taking the thickness to be equal to the lateral dimension of a cube having the same area as the high OD areas. The number of pixels with an

OD >1.5 are added up and the square root of sum is taken, this is then multiplied by the pixel width and the result is used as the particle thickness for all OD >1.5 pixels.

2.4 Results and Discussion

2.4.1 Particle morphology. Particle mixing state and morphology can potentially impact their effectiveness as either ice nuclei or CCN.[127-130] Here, particles were produced by nebulization of mixed organic/inorganic solutions of known concentrations. Because each of the solutes are quite soluble in water (with solubilities of 75.4 g/100 mL, 35.9 g/100 mL, and 201.9 g/100 mL for ammonium sulfate, sodium chloride, and sucrose respectively)[131] and because the nebulization process ensures a well-mixed solution, the resulting droplets are expected to be similar in composition to the homogenous bulk solution and therefore little particle-to-particle variability is anticipated. When qualitatively comparing OVF and carbon speciation maps, most samples exhibited a core-shell morphology that is common in mixed inorganic/organic systems.[55, 132] A few representative pairs for the sodium chloride/sucrose and ammonium sulfate/sucrose systems are shown in Figure 2.3 and Figure 2.4 respectively.

2.4.1.1 Sodium chloride / sucrose morphology. For the sodium chloride/sucrose system, across all stages the inorganic rich mixture showed cubic particles with few organic dominant regions according to the C speciation map. In the OVF maps, like the one shown in Figure 2.3, a thin coating of organics can be seen surrounding the inorganic centers. This thin coating of organics is not visible in the C speciation map due to the threshold of the pre to post edge ratio for all pixels exceeding 0.5 as described above. Particles appear to be made up of multiple smaller cubic units which is consistent with scanning electron microscopy images of lab-generated sodium chloride aerosols.[133]

Sodium Chloride/Sucrose
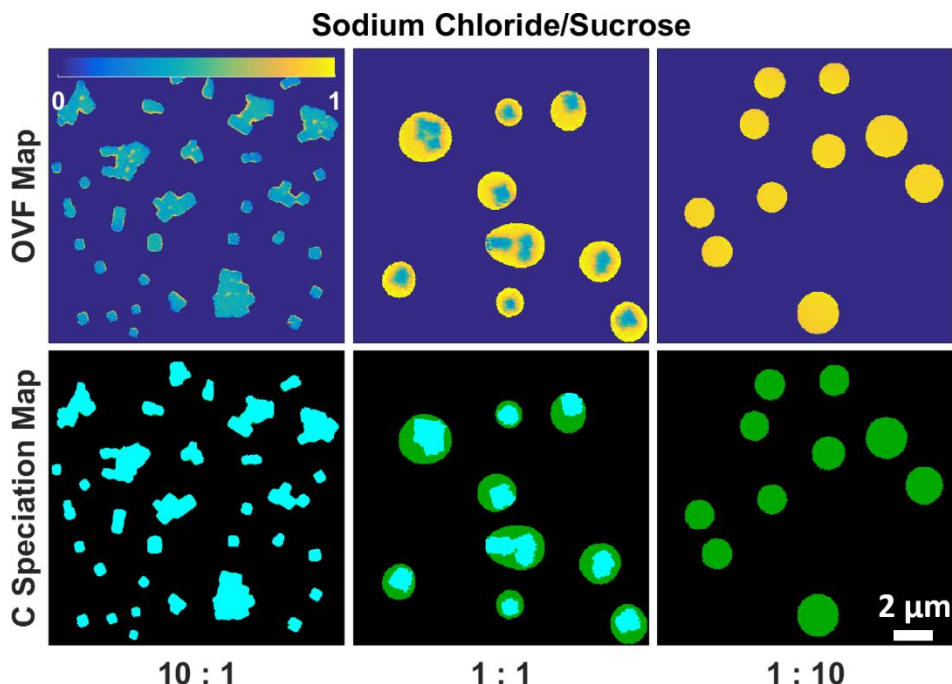
Figure 2.3 Representative OVF maps and C speciation maps for sodium chloride/sucrose systems. Samples shown were collected from impactor stage C (0.5 – 0.25 μm nominal size range). For the C speciation maps, green represents organic dominant and blue represents inorganic dominant regions.

A similar observation can be made for the 1:1 mixture, except with a thicker coating of organics. Of note here is the ability to resolve multiple individual NaCl crystals within some of the aerosols when looking at the OVF maps. Particles collected from the smallest stage (stage D, not shown) can still be seen as an inorganic core with an organic coating in the OVF maps, although it is no longer apparent from the C speciation maps. A few of the particles appear not to exhibit a core-shell morphology but instead look partially engulfed, which is observed for inorganic/organic mixtures under certain conditions.[134] However, this may well be a result of impaction and so it is difficult to comment on how these particles look when airborne.

OVF maps and C speciation maps for the organic rich mixture show circular homogenous particles over all stages. No NaCl dominant inclusions or particles were observed though some inorganic material was detected based on the pre-edge absorption. From the OVF map in Figure 2.3, the inorganic phase present is homogenously mixed with the organic phase in this system.

Previous studies have shown that high organic concentrations can inhibit the crystallization of inorganic species.[135-136]

      2.4.1.2 Ammonium sulfate / sucrose morphology. In contrast to the sodium chloride/sucrose system, the inorganic rich mixture for the ammonium sulfate/sucrose system did not show cubic crystals. Instead circular inorganic particles were observed in all stages. Ammonium sulfate particles have been observed with a circular or rounded shape by TEM at these sizes before.[137-138] Pósfai, *et al.* suggested that the ammonium sulfate started forming as a polycrystalline solid but then recrystallized. Most of the ammonium sulfate particles observed by Pósfai, *et al.* were rounded and, although some particles were aggregates, selected area diffraction (SAED) patterns indicated most were single crystals. In addition, a bumpy irregular surface was documented. Buseck *et al.* showed how ambient ammonium sulfate particles had a coating of organics which filled in these bumps and irregularities. From the OVF maps in Figure 2.4 of the current work, a thin coating of organics can be seen in most particles along with a few particles which show a higher than average OVF.
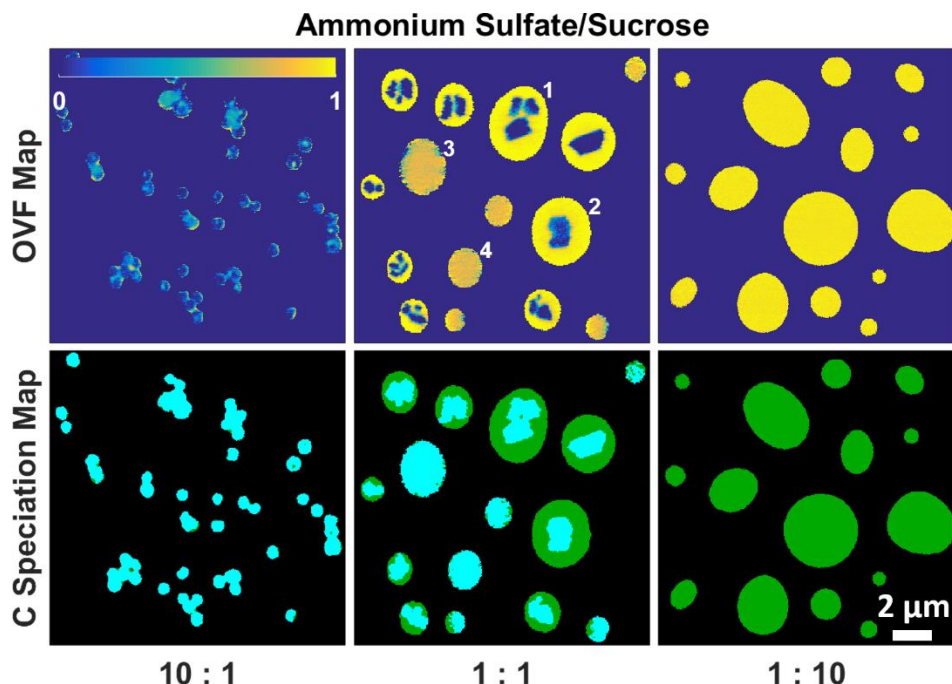
Figure 3.4 Representative OVF maps and C speciation maps for the ammonium sulfate/sucrose systems. Samples shown were collected from impactor stage C ($0.5 - 0.25$ μm nominal size range). For the C speciation maps, green represents organic dominant and blue represents inorganic dominant regions. The four particles labeled in the top middle image have OVFs of: 0.56, 0.41, 0.77, and 0.79 for particles labeled # 1, 2, 3, and 4 respectively.

The 1:1 ammonium sulfate/sucrose mixture presented two distinct particle types, seen in both OVF and C speciation maps. A core-shell type of particle is most commonly observed with a defined, rectangular inorganic core surrounded by a thick organic coating. Also seen are circular, fairly homogenous particles which have a pre to post edge ratio > 0.5 according to the C speciation map. The OVF map, however, shows that around 75% of the volume of these particles are attributed to the organic component. This phase separation is discussed in further detail below.

The organic rich mixture of ammonium sulfate and sucrose shows the same behavior as the sodium chloride/sucrose system, with homogenous organic dominant particles. This, as well, is likely attributed to the inhibition of crystallization in concentrated organic solutions. The lack of efflorescence, even at low relative humidity, has been previously observed for ammonium

sulfate/organic mixed aerosols with an organic O:C ratio > 0.7 and organic:sulfate mass ratios above 2.[139] In this study, the lack of efflorescence was seen with an organic:sulfate mass ratio of 10:1 and so, with an O:C ratio of 0.91, so this system should be governed by the same principles.

2.4.1.3 Multiple inorganic inclusions. For the inorganic rich and 1:1 systems, multiple distinct inorganic inclusions can be seen within individual particles. This may be a result of using the relatively viscous sucrose as the organic component. A similar diffusion dryer setup to the one shown in Figure 2.1 has been studied previously reported to dry at a rate of ~99.7% RH/s.[55] As a droplet of solution begins to rapidly dry passing through the dryers, its viscosity increases. By becoming increasingly viscous, mass transfer of components within the particle is inhibited [140-141]. Upon reaching a low enough water activity, spontaneous nucleation of the inorganic component begins but diffusion of additional inorganics is hampered by the viscous droplet. As drying continues, more nucleation centers form and crystallize before they are able to combine into a single inorganic core. The formation of single or multiple inorganic inclusions as a result of drying rate has been observed before in less viscous organic/inorganic systems.[142]

2.4.2 Accuracy of single-particle organic volume fractions. Experimental per-particle OVFs for each system and mixture were averaged over all stages and compared with the theoretical OVFs in Figure 2.5 and in Table 2.2. Values for Organic Mass Fractions (OMF) are included as well for completeness sake and for discussion in section 3.3 below. The bulk OVF values were calculated using the composition of the bulk solution from which the particles were generated. For the sodium chloride/sucrose system, the experimental OVFs were underestimated compared to theoretical OVF in all except the inorganic rich mixture which was overestimated. The experimental OVFs for the ammonium sulfate/sucrose mixture are all underestimated as well.
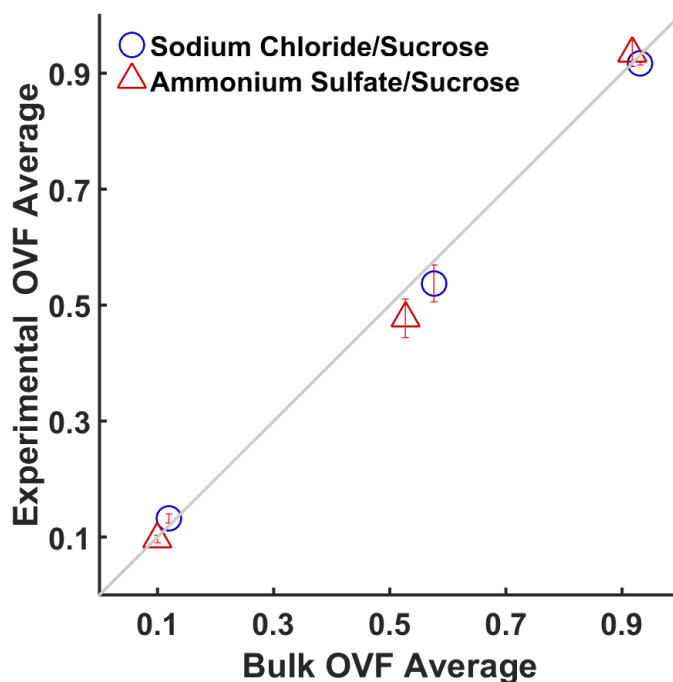
Figure 2.5 Correlation between experimentally determined and bulk average OVFs. A 1:1 line is shown in gray. Error bars represent standard error calculated by StdErr = (1.96 · S)/(N1/2) where S is the standard deviation, N is the number of particles, and 1.96 is the approximate number of standard deviations encompassing the central 95% of a student's t distribution.143 Error in bulk OVF is too small to be shown.

2.4.2.1 1:1 systems. The largest deviation of the experimental OVF from the OVF

calculated from the bulk solution was observed with 1:1 mixtures for both the sodium

chloride/sucrose and ammonium sulfate/sucrose systems. Both of these systems were

underestimated for similar reasons. Aerosols in both samples contained thick inorganic

inclusions surrounded by organics (see Figures 3 and 4). Many of these thick inorganic crystals

were thick enough for their OD to exceed the linear range of Beer-Lambert's law (OD >1.5) and

so the correction mentioned above was applied. However, considering that these cores are

surrounded with a layer of organics, there is likely a layer above and below which the high-OD

correction does not account for. This will lower the apparent volume of organics in those

regions and decrease the particle's overall OVF value.

2.4.2.2 Inorganic rich systems. The inorganic rich systems for both the sodium

chloride/sucrose and the ammonium sulfate/sucrose mixture were slightly overestimated (0.012

and 0.009 respectively, from Table 2.2). This overestimation may be due to some amount of

defocusing, especially in the pre-edge image. Images which were obviously defocused exhibited

OVFs much higher (>30% higher for the inorganic systems) than well focused images and were

excluded from analysis; however, images with subtler defocusing may still be present. Any

defocusing present in the pre-edge images will result in depression of the measured OD,

especially around the particle edges. Equation (2.4) shows that a decreased pre-edge OD will

also increase the calculated organic thickness and therefore the OVF as well. As for the potential

effects of the high-OD correction, while sodium chloride crystals which exceeded 1.5 OD were

present, the organic coatings observed are very thin, making this a minor issue. Instead, if the

high-OD correction underestimated the thickness of inorganics present, this could also contribute

to the overestimation in OVF for the sodium chloride/sucrose system. Another possible

contribution to the slightly high OVF is if any carbonate was incorporated in the standard

solutions during nebulization, as this ion will contribute to the carbon post edge value which was

assumed to be dependent only on organics. Carbonate picked up from dissolved CO_2, however,

would only amount to approximately 1×10^{-5} g in the 100 mL jar, which would correspond to an

erroneous OVF increase of about 0.0005% and so the contribution is negligible.[144] The

overestimation in the ammonium sulfate/sucrose system was smaller and, unlike with the sodium

chloride/sucrose system, was within the margin of statistical error. The inorganic rich

ammonium sulfate system also did not have any issues with thick inorganic regions making it a

fairly well-behaved system for STXM analysis. While the decrease in optical thickness of the

ammonium sulfate particles compared to the sodium chloride particles could be due to

differences in physical height, this is difficult to know given 2-dimensional images. However,

the absorption cross section for ammonium sulfate is lower than the cross section for sodium

chloride by a factor of 0.35,[92] which accounts for most of the difference in optical thickness.

   2.4.2.3 Organic rich systems. As shown in Table 2.2, the average OVF value for the

organic rich systems are in good agreement with their bulk OVF values, having an error of 0.009

for the sodium chloride/sucrose system and an error of 0.008 for the ammonium sulfate/sucrose

system. These errors are the lowest for their respective inorganic/organic systems. Because

OVF is calculated using STXM images collected before and after the C absorption edge, it is

most sensitive to C containing compounds. In addition, three of the four C edge energies taken

were associated with organics. Because of this, organic rich particles may have better defined

edges relative to inorganic particles when particle detection is performed. The OVF calculation

is thus well suited to organic rich particles like these and because of this, the error in

experimental OVF fell within the bounds of statistical uncertainty.

Table 2.2 Experimental and bulk values for Organic Volume Fraction and Organic Mass Fraction. Values shown along with their associated absolute error (Relative errors for OVF and OMF are identical to within rounding). Errors with an asterisk cannot be attributed to statistics (95% confidence) alone.

System		Fields of View	Organic Volume Fraction			Organic Mass Fraction		
			Experimental	Bulk	Error	Experimental	Bulk	Error
Sodium Chloride / Sucrose	Inorganic Rich	6	0.132	0.120	0.012*	0.100	0.091	0.009*
	1:1	3	0.538	0.576	0.039*	0.467	0.500	0.033*
	Organic Rich	3	0.923	0.931	0.009	0.900	0.909	0.009
Ammonium Sulfate / Sucrose	Inorganic Rich	4	0.091	0.100	0.009	0.082	0.091	0.009
	1:1	11	0.571	0.527	0.044*	0.542	0.500	0.042*
	Organic Rich	6	0.926	0.918	0.008	0.917	0.909	0.008

   2.4.2.4 Phase separation in 1 : 1 ammonium sulfate / sucrose system. For the 1:1

Ammonium Sulfate/Sucrose system seen in Figure 2.4, two particle types were observed:

particles with a core-shell morphology where the organic regions surround a distinct inorganic

core, and homogenous particles where a relatively constant OVF was observed. The presence of

both phase-separated and homogenous particles was observed only for the 1:1 Ammonium

Sulfate/Sucrose system and was observed across all size ranges. Figure 2.6 highlights this

system as unique compared to the others studied here.
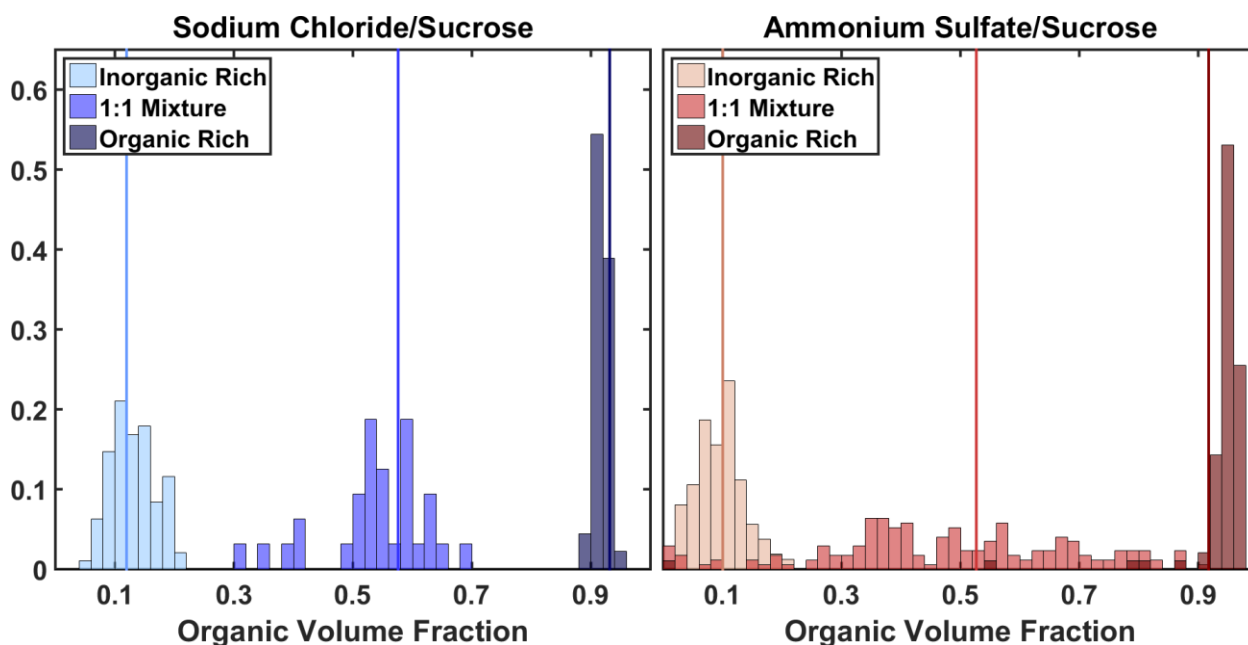
Figure 2.6 OVF histograms of sodium chloride / sucrose (blue) and ammonium sulfate / sucrose (red) systems. The three mass ratios, 10 : 1 (inorganic rich), 1 : 1, and 1 : 10 (organic rich), are shown in different shades of color. The vertical line represents the bulk OVF value.

The distribution of OVF values for most systems were Gaussian and centered around the

bulk OVF value. The organic rich systems showed little spread due to STXM's sensitivity to

carbon. Both inorganic rich systems had wider distributions and the 1:1 systems showed the

widest OVF distributions. One issue that can plague particles with crystalline regions is that

upon impaction with the substrate the particle can shatter.[145] Shattering involves small pieces of

the particle breaking away, potentially removing organic and inorganic mass from the main

particle in difficult to predict ratios. While we do not see small fragments distributed amongst

larger ones, small particle fragments are observed in the lowest stage. This may be due to the

shattered fragments bouncing upon formation and travelling further down the impactor. The 1:1

Ammonium Sulfate/Sucrose system, however, shows far more spread than any of the others due

to the two particle types observed in this system.

This distinction between phase separated particles and homogenous ones has been

observed before when mixed ammonium sulfate/polyethylene glycol-400 particles generated

from an aqueous solution are quickly dried before collection [146]. Some of the particles studied

were dried so quickly that a fraction of them were observed to solidify into an amorphous phase

rather than nucleate a distinct crystalline phase. Because the diffusion drier setup described in

the experimental section for the current work is drying particles at a similar rate compared to the

rate discussed in Altaf *et al*., 2017, the same two types of particles were observed.

A size-dependent trend was also present in the 1:1 Ammonium Sulfate/Sucrose system,

with the homogenous particles tending to be smaller on average than the phase separated ones

(see Figure 2.7). This behavior was previously observed by Altaf *et al.,* in 2016, using an

Ammonium Sulfate/Polyethylene glycol mixture. They observed that, depending on the

inorganic/organic ratio, the inorganic compound could start to undergo spinodal rather than

binodal crystallization. The end result was a size dependence seen in certain inorganic/organic

mass ratios, where nucleation of a separate phase became more energetically unfavorable at

smaller sizes.[147]
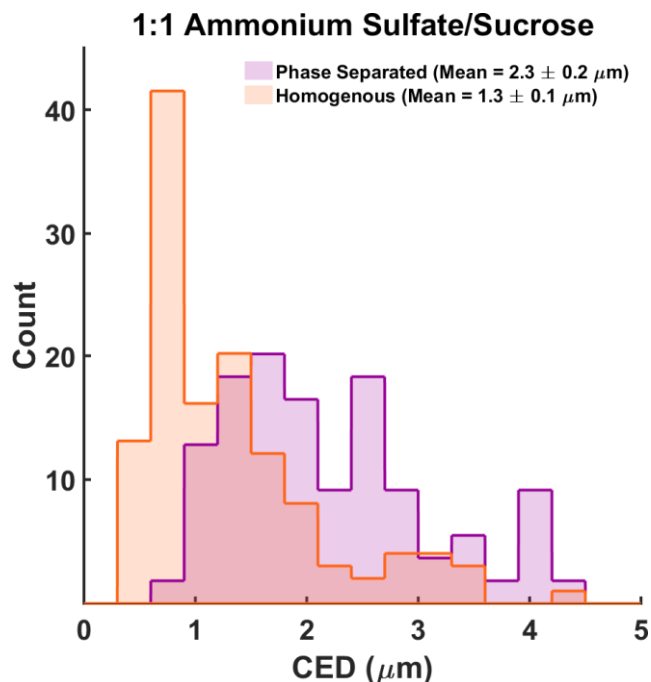
Figure 2.7 Circular equivalent diameter (CED) histogram of homogenous and phase-separated particles. This shows that homogenous particles tended to be smaller than phase-separated ones. Particles from stages B, C, and D are included here (2.5 – 0.25 μm).

The size distributions discussed in Altaf *et al.,* 2016 and Altaf and Freedman, 2017 are on the order of 200 nm, about a factor of 10 smaller than the size distributions observed here. The increase in viscosity from using sucrose as an organic rather than polyethylene glycol may increase the sizes at which phase separated and homogenous particles overlap. This was noted in Altaf *et al.*, 2016, that the components within smaller viscous particles may not have enough time to coalesce into a completely phase separated particle. In addition, rapid drying may also result in the formation of an inorganic shell as the surface of a particle dries without water within the particle able to spread outward fast enough for very viscous particles.[140]

The presence of two particle types (homogenous and phase separated) do not, alone, account for the spread of OVF seen in Figure 2.6 for the 1:1 ammonium sulfate/sucrose system. Although both types of particles are formed from the same bulk solution, and so are assumed to have the same composition, two competing issues in their analysis serve to broaden their OVF

distribution. For the phase separated particles, the issue of thick central regions persists. Because the high-OD correction may discount any organic coatings found above or below these regions and so the OVF will be depressed for these particles, this is shown in Figure 2.8 where all of the high-OD particles are found below the bulk OVF value.
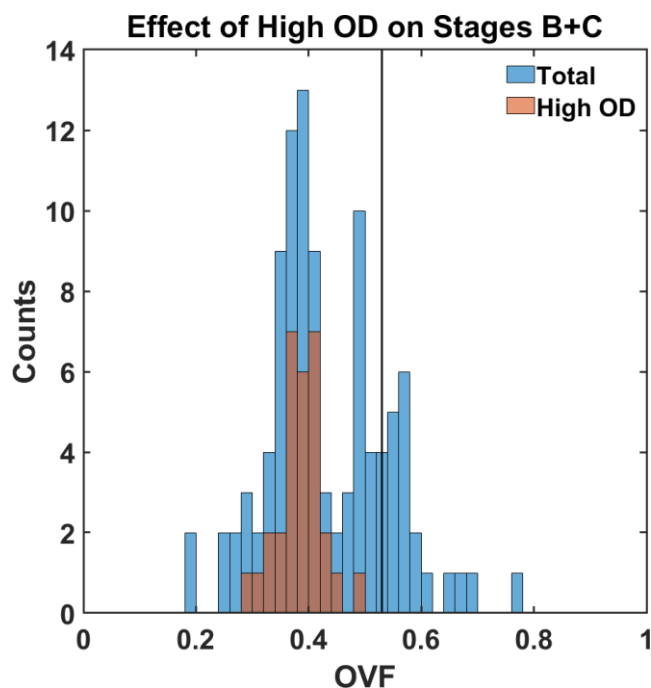
Figure 2.8 Histogram of particles from stages B and C from the 1 : 1 ammonium sulfate / sucrose system. The OVF of particles with regions exceeding an optical density (OD) of 1.5 are shown in red. The black vertical line is the OVF expected from the bulk solution.

Figure 2.9 shows a related idea where all of the phase separated particles are found below the bulk OVF value because the phase separated particles tend to be the ones with thick inorganic regions. For homogenous particles, having the inorganics distributed throughout the particle rather than concentrated in a core could result in some regions where the inorganics were poorly characterized, thereby raising the OVF. For instance, if any inorganic regions were located near the edge of the particle, the particle detection algorithm could exclude them due to

having only 1 STXM image associated with inorganics. As mentioned above, because the

organic components have 3 images (some with strongly absorbing transitions), organic regions

near the particle's edge are more likely to be better defined. The homogenous particles in Figure

2.4 with rough edges and low OVF points to this.
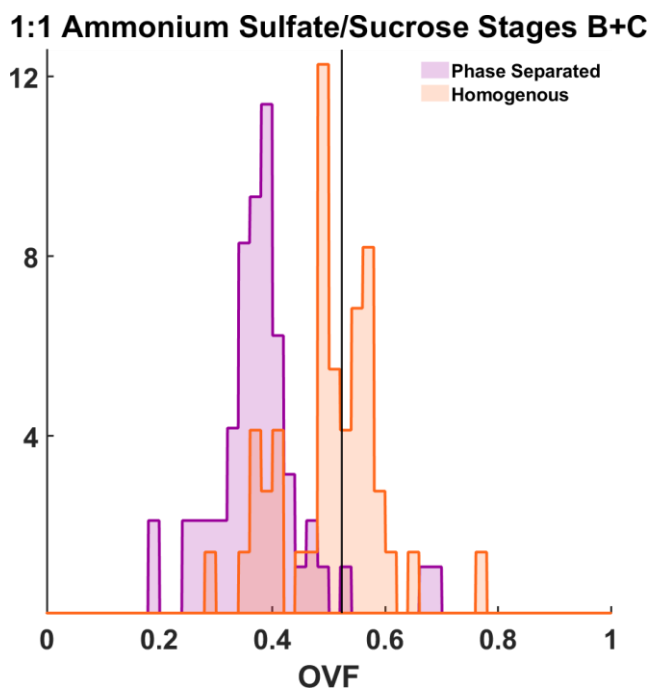
Figure 2.9 Histograms of stage B + C for the 1 : 1 ammonium sulfate / sucrose system. Both phase separated and homogenous particles are shown in separate histograms. The black vertical line is the OVF expected from the bulk solution.

Much of the extreme spread seen in the 1:1 ammonium sulfate/sucrose system, however,

is due to the smallest stage (stage D, 0.25 – 0. 5 μm). Figure 2.10 shows the OVF distribution of

this stage and the presence of almost pure inorganic and pure organic particles. This may be the

stage where fragments of particles from shattering and particle bouncing are found, with

bouncing being a particular issue for viscous particles like these.[148-151] Because shattered

fragments will not necessarily have the same organic/inorganic ratio as the bulk solution, these particles can have much higher and much lower OVF values.
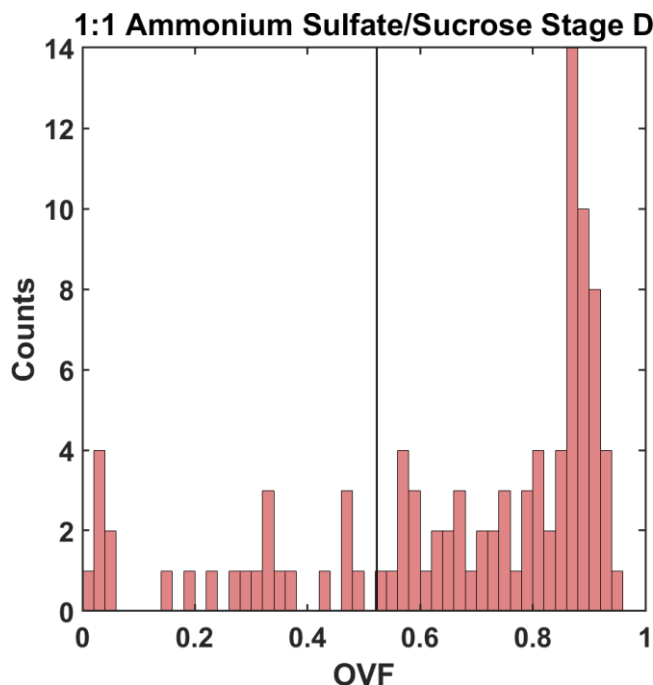
Figure 2.10 Histogram of OVFs for only stage D particles for the 1:1 ammonium sulfate/sucrose system. This shows that the extreme spread originates mainly from these particles. The black vertical line is the OVF expected from the bulk solution.

Figure 2.11 shows an X-ray micrograph of stage D particles with arrows pointing to potential fragments from shattering. These small particles are irregularly shaped (compared to the numerous surrounding circular particles) and are the particles with the extreme high and low OVF values.

Average OD for Stage D, 1:1 Ammonium Sulfate/Sucrose
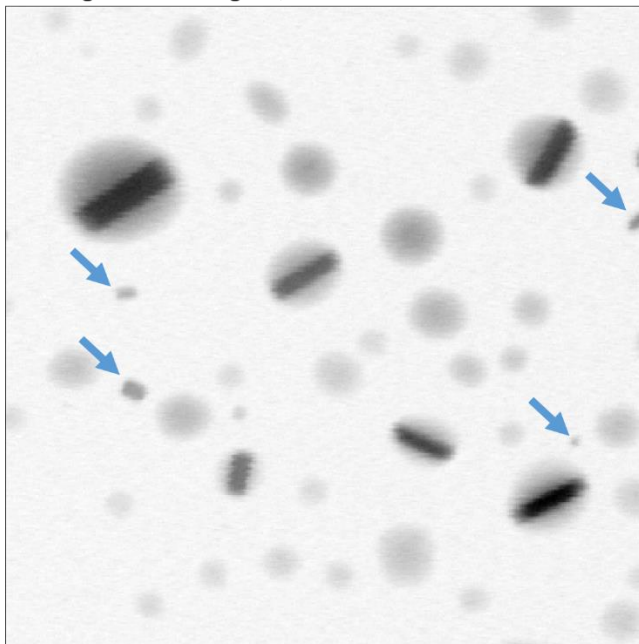
Figure 2.11 Representative average OD micrograph of the 1 : 1 ammonium sulfate / sucrose system, stage D. The average OD image provides good contrast for visualizing inorganic and organic particles. Blue arrows point to some irregularly shaped particles which suggests fragments from particle shattering.

2.4.3 Effect of inorganic and organic assumptions on OVF accuracy. All data shown above has been obtained with the known compounds being used in calculating OVF values. However, studies of ambient samples often lack prior knowledge of the major inorganic and organic species present within individual particles. Previous studies have utilized this OVF calculation for sea spray aerosols, and for these samples, sodium chloride and adipic acid were used as proxies. Sodium chloride was chosen as an inorganic due to its prevalence in ocean water and adipic acid was chosen because it has an O:C ratio of 0.66 which corresponds to aged organic aerosol species.[152] Figure 2.12 and Table 2.3 shows the result of this assumption for each system studied here.
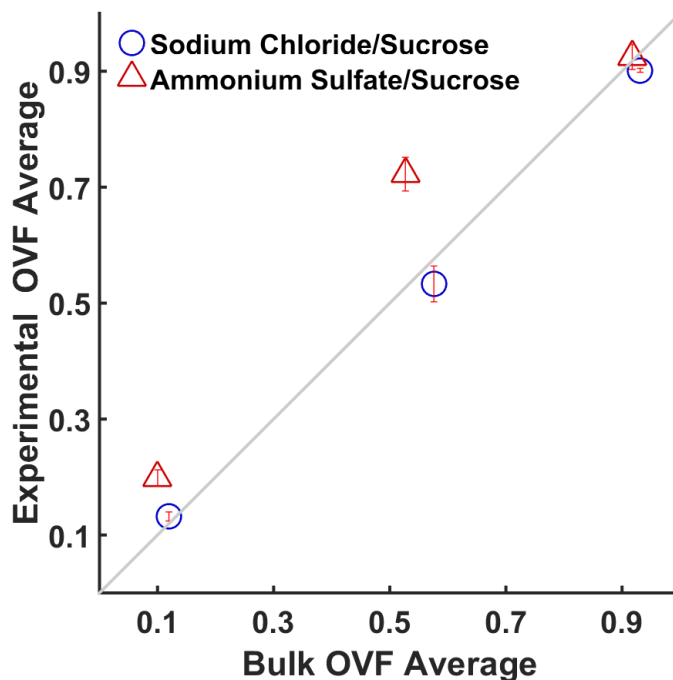
Figure 2.12 Correlation between experimentally determined and bulk OVF averages with assumed composition. sodium chloride and adipic acid were used as the assumed inorganic and organic, respectively.

The sodium chloride/sucrose system shows the effect of changing only the organic assumption from sucrose to adipic acid. Adipic acid has been used before as a proxy for oxidized organic matter based on its O:C ratio.[152] Table 2.3 shows that the experimental average OVF for each formulation decreased slightly, with the average OVF of the organic rich system decreasing more than the 1:1 system. The inorganic rich system showed very little change in experimental OVF which is expected because the assumed inorganic did not change. The insensitivity of OVF values to the assumed organic has been previously remarked upon using a few other assumed organics as well.[37]

Table 2.3 Experimental and bulk values for OVF and OMF under different inorganic and organic assumptions. The difference between OVF values using the known composition versus using sodium chloride and adipic acid is also shown.

System		Organic Volume Fraction			Organic Mass Fraction		
		Assumed Composition	Known Composition	% Difference	Assumed Composition	Known Composition	% Difference
Sodium Chloride / Sucrose	Inorganic Rich	0.132	0.132	0	0.087	0.100	1.3
	1:1	0.533	0.538	0.4	0.434	0.467	3.2
	Organic Rich	0.917	0.923	0.6	0.886	0.900	1.5
Ammonium Sulfate / Sucrose	Inorganic Rich	0.198	0.091	10.8	0.132	0.082	4.9
	1:1	0.723	0.571	15.2	0.589	0.542	4.7
	Organic Rich	0.931	0.926	0.5	0.899	0.917	1.8

There is a much more pronounced error introduced by using sodium chloride as a proxy for ammonium sulfate inorganics. Although the sensitivity of OVF to the assumed inorganic is increased compared to the assumed organic, the error is accentuated in this specific case. Because Cl has an absorption edge quite close (~270 eV) to C's absorption edge, including or excluding Cl will result in a significant change in how the pre-edge mass absorption coefficient is calculated and can result in up to a 25% error in OVF. In the case of assuming sodium chloride instead of ammonium sulfate, more of the pre-edge's OD is attributed to the increased absorption coefficient and less to the mass (and therefore the thickness) of the inorganic. This effect inflated the OVF of both the 1:1 and the inorganic rich system. The overestimation of OVF was subdued in the inorganic rich system because OVF is calculated as a ratio between organic and total volume; if the organic volume is small to begin with, the ratio will not be as affected by changes in the total volume.

Although OVFs are of interest due to their utility in κ-Köhler calculations, OMF values are readily obtained and have the benefit of not needing to assume the density of the organic and inorganic components. As far as calculating OMF versus OVF when the composition is known,

there is no difference in the error with respect to the bulk solution values (as seen in Table 2.2).

Table 2.3 also compares the OMF values obtained using the known organic and inorganic

composition with the OMF values obtained from the adipic acid/sodium chloride assumption. At

first glance, the OMF differences between the known and assumed cases do not share the same

trend as seen with OVF values. This is because the error associated with assuming an inorganic

and organic composition lies in two places: the calculation of the mass absorption coefficient,

and the density. The larger an assumed mass absorption coefficient, the more absorption will be

assigned to a specific component. Largely independent from this is the density assumption,

which dictates the volume of a specific component. These two values can serve to affect

resulting OVF in the same direction together, or can act separately in opposite directions.

Because of this, the effect of removing the assumption of density to calculate OMF instead of

OVF changes on a case-by-case basis. For any given set of assumptions, however, the OVF and

OMF will always differ by a constant (C) via the following equation:

$$C = \frac{\left(f^I\rho^O + f^O\rho^I\right)}{\left((f^O + f^I)\rho^I\right)}$$
(2.6)

where f^x and ρ^x represent the mass fraction and density of component x respectively.

The OMF calculations in Table 2.3 also show that these calculations are more sensitive to

the assumptions about the inorganic component than the organic component. The OMF

calculations also show that an erroneous mass absorption coefficient assumption will affect the

calculation's accuracy even without the assumption of density. In addition, in order to calculate

a mass absorption coefficient a molecular formula must be assumed. For organic components,

these assumptions are often supported by estimates of O/C or N/C ratios. These constraints,

along with the usefulness of the OVF calculation, can make assuming a density worthwhile. The

error of using the assumed system of NaCl and adipic acid (with densities of 2.16 and 1.36 g/mL

respectively) in the extreme case that the density assumptions are very wrong in opposite directions (say the real composition is Fe_2O_3 and pinene with densities of 5.24 and 0.86 g/mL respectively) is approximately a factor of 3.

Note that an appropriate choice for the organic or inorganic proxy for calculation purposes can be guided using peripheral measurements when analyzing ambient samples. Size resolved composition information (either molecular or elemental) can be used to constrain the identity of the components. Additionally, combining another microscopy technique which can probe heavier elements, like Scanning Electron Microscopy with Energy Dispersive X-ray spectroscopy (SEM/EDX), will narrow down the possible inorganics present within individual particles as has been shown previously.[114] Also, because the mass absorption coefficient is calculated from the compound's molecular formula, measurements of elemental ratios can serve to improve the OVF value calculation. Because of the erroneous assumption about Cl in the ammonium sulfate/sucrose system discussed above, the change in OVF in this case represents one of the larger errors possible.

2.5 Conclusions. The OVF values determined experimentally matched the values from the bulk solution well, when the known inorganic and organic compounds are used. Aerosols that are primarily composed of either inorganic or organic seem produce the smallest errors. The OVF of organic aerosols can be determined to within 0.8% under ideal conditions while the OVF of inorganic aerosols can be determined to within about 1%. Additional care must be taken when mixed phase aerosols are present that thick inorganic regions do not compromise the OVF calculation, although OVF can still be calculated to within about 4% even with thick inorganic regions.

The results shown here are most easily attainable after a series of quality control measures have been conducted. Quality control checks for issues including proper alignment, focused images, and accurate particle detection are important. These issues can result in not only a less reliable OVF calculation, but can greatly change the interpretation of an aerosol data set. Most of these issues are best remedied during data collection, though filtering data after the fact can help as well. The results here also highlight the importance of considering how particle generation and collection factor in to the results. It was observed here that particle shattering and impactor bounce may have contributed to the large spread in OVF values in the 1:1 ammonium sulfate/sucrose system.

The calculation of OVF from OD images necessitates some assumptions which should be examined during data analysis. Regions with high OD (>1.5, outside of the linear range of Beer's law) are again best remedied during data collection by avoiding high OD particles if possible. Although these high OD regions can be approximated, the quantitative nature of this technique can be compromised. This approximation tends to depress the average OVF when organic coatings are present, and so should be kept in mind when interpreting results. To ensure quantitative OVF calculations with tight distributions, which agree with bulk measurements, it is important to focus on mainly carbonaceous particles (to ensure sufficient carbon signal) or particles with thin enough inorganic inclusions (to reduce regions where beer's law is nonlinear). In general, smaller (fine mode) particles will be best suited to this type of calculation. Assumptions about the identity (or at least the molecular formula and density) of the inorganic component can also potentially have a large effect on the calculated OVF. An incorrect assumption can result in an error upwards of 15%. Because most common organic components

in aerosols are similar in composition and density, the OVF is much less sensitive to an incorrect assumption here.

Additional spectroscopic images can be used here to great effect. Along with C K-edge data, imaging particles using the nearby Cl, S, Ca, or K edges can help both better define particle boundaries and improve assumptions about the inorganic component. This, however, comes at the cost of particle population statistics as more time is spent on fewer particles. Similarly, the identity of the organic component can be better refined by including more energies while taking C edge data. For example, including an image at 290.1 eV could help remedy the issue mentioned above about carbonate falsely increasing the amount of organics.

With the proper attention paid to the quality of data, STXM can be used to quantitatively determine the OVF of a set of aerosols to within less than 1%. This method of calculating OVF has previously been used on ambient samples as an indirect measure of biological activity in sea water.[37] When applying this method to ambient samples the analyst should note factors that can affect the accuracy of the results. As an example, volatile organics and inorganics (such as ammonium nitrate) will not be accounted for due to evaporation in the vacuum of the STXM chamber. However, even being predicated on assumptions about the inorganic and organic components, the OVF can be quantitatively determined. Because of this, other STXM results such as the mass fraction of carbon and the absolute mass of carbon (which do not rely on density assumptions) can be determined quantitatively as well. Because STXM offers morphological information along with elemental and molecular composition on a sub-particle basis, it can be a powerful technique for analyzing aerosol populations. If care is taken during data collection and analysis, these quantitative results can be used to develop model parametrizations with some confidence regarding the level of associated error.

Chapter 3: Elemental Mixing State of Aerosol Particles Collected in Central Amazonia During GoAmazon2014/15

3.1 Synopsis

Two complementary techniques, Scanning Transmission X-ray Microscopy/Near Edge Fine Structure spectroscopy (STXM/NEXAFS) and Scanning Electron Microscopy/Energy Dispersive X-ray spectroscopy (SEM/EDX), have been quantitatively combined to characterize individual atmospheric particles. This pair of techniques was applied to particle samples at three sampling sites (ATTO, ZF2, and T3) in the Amazon basin as part of the Observations and Modeling of the Green Ocean Amazon (GoAmazon2014/5) field campaign during the dry season of 2014. The combined data was subjected to k-means clustering using mass fractions of the following elements: C, N, O, Na, Mg, P, S, Cl, K, Ca, Mn, Fe, Ni, and Zn. Cluster analysis identified 12 particle types, across different sampling sites and particle sizes. Samples from the remote Amazon Tall Tower Observatory (ATTO, also T0a) exhibited less cluster variety and fewer anthropogenic clusters than samples collected at the sites nearer to the Manaus metropolitan region, ZF2 (also T0t) or T3. Samples from the ZF2 site contained aged/anthropogenic clusters not readily explained by transport from ATTO or Manaus, possibly suggesting the effects of long range atmospheric transport or other local aerosol sources present during sampling. In addition, this data set allowed for recently established diversity parameters to be calculated. All sample periods had high mixing state indices (χ) that were >0.8. Two individual particle diversity (Di) populations were observed, with particles <0.5 µm having a Di of ~2.4 and >0.5 µm particles having a Di of ~3.6, which likely correspond to fresh and aged aerosols respectively. The diversity parameters determined by the quantitative method presented here will serve to aid in the accurate representation of aerosol mixing state, source apportionment, and aging in both less polluted and more industrialized environments in the Amazon Basin.

3.2 Introduction

Atmospheric aerosols are solid or liquid particles suspended in air and are comprised of mixtures of organic and/or inorganic species: organic molecules, salts, soot, minerals, and metals.[1] Aerosols have a highly uncertain effect on radiative forcing.[4] Aerosol forcing occurs via two mechanisms: light can be scattered or absorbed directly by the aerosol particle (the "direct effect", also aerosol-radiation interactions) or indirectly through aerosol effects on cloud formation (the "indirect effect", also aerosol-cloud interactions).[102] The latest Intergovernmental Panel on Climate Change (IPCC) report, released in 2013, shows that the extent of anthropogenic effects on cloud formation is currently the largest source of uncertainty for predictive understanding of global anthropogenic radiative forcing.[4] Both direct and indirect effects are heavily influenced by the composition of aerosols on a per-particle level.[153-155] To better understand and predict the influence of industrialization, one aspect of particular interest is the effect that anthropogenic emissions have on the per-particle composition of aerosols and their impacts on local and global climate.[4, 83]

One underlying reason for this uncertainty is the complex manner in which aerosol composition changes over time and distance through coagulation, condensation, and chemical reaction.[156] Because aerosol radiative forcing and cloud formation depend on the individual particle composition, it is important to know how atmospheric components are mixed within a population of aerosols. How these components are mixed plays a large role in determining the manner and extent to which radiative forcing is affected. For example, the coating of soot by organics can change the radiative forcing of those aerosols by as much as a factor of 2.4 over pure soot.[52, 73, 154, 157] Hence, in this case, it is important to know whether soot and organics coexist in the same aerosol particle. How components are mixed in an aerosol sample is referred to as its mixing state. This mixing state can range anywhere from an internal mixture where each

component is evenly distributed throughout all particles, to an external mixture where each component occupies its own population of particles. Many atmospheric models assume one of these extremes throughout their simulation.[158-160] Some models include a specific aspect of aerosol mixing such as the mixing state of black carbon,[39, 153] while other, nascent, models will account for a more complete mixing state.[38] Mixing state values for coated black carbon (BC) have been determined using a soot photometer based on the time delay between light scattering and soot incandescence but thermodynamic properties of organic coatings must be assumed to infer coating thicknesses, making the technique qualitative.[75, 161] This approach also becomes less applicable if inorganic dominant or non-soot containing particles are of interest. A real-time method in determining aerosol mixing state index has been achieved by using single particle mass spectrometry,[162] although this technique is blind to detailed aerosol morphology.

Recently, more nuanced metrics were developed to quantify the mixing state of a population of aerosols.[41] This method of mixing state determination necessitates a mass quantitative method of determining per-particle composition. Spectromicroscopy techniques are uniquely suited to analyze both the morphology and the comprehensive mixing state of a population of aerosols. Here, these quantitative mixing state metrics are applied to microscopy images of particle samples collected in the central Amazon basin.

In this study, we determine the mass fractions of 14 elements on the exact same set of particles using the complementary techniques of Scanning Transmission X-ray Microscopy with Near-Edge X-ray Absorption Fine Structure spectroscopy (STXM/NEXAFS) and Scanning Electron Microscopy coupled with Computer Controlled Energy Dispersive X-ray spectroscopy (SEM/EDX). Each technique is limited in which elements it can investigate. STXM/NEXAFS is limited by the energy range of the synchrotron insertion device as well as the limited beamtime

available for sample analysis. STXM/NEXAFS has the advantage of providing quantitative measurements of light, low Z (atomic number) elements (C, N, and O). Although SEM/EDX provides a faster method of per-particle spectromicroscopy, it is not quantitative for low Z elements (Z<11, Na). These two techniques are inherently complementary, with each technique providing mass information on elements that the other cannot adequately probe and both providing this information on an individual particle level. Both techniques have been used in tandem on microscopy samples previously.[124] In a similar way to Piens *et al.*, 2016,[115] STXM and SEM data are combined at the single particle level. The per-particle elemental mass fractions determined herein are used to calculate an elemental mixing state for particles collected at three sampling sites.

Aerosol production in the Amazon basin plays an important role in global climate due to the large scale of biogenic emissions from the tropical forest often mixed with pollutants from vegetation fires (mostly related to deforestation and pasture burning).[163-166] South America contributes significantly to the global aerosol carbon budget; ~17% of global soot emissions are produced in Central and South America combined.[167] Aerosols are also subject to long range transport and thus are of importance to global models.[168] This environmentally important region of Central Amazonia contains Manaus, a city with over two million people. Manaus is a large industrial manufacturing city as a consequence of its free trade status since the 1960s. The juxtaposition of pristine rainforest with a large anthropogenic center presents a unique circumstance for studying how native biogenic aerosols are affected by emissions from an industrial city.[169] To take advantage of this unique location, the Observations and Modeling of the Green Ocean Amazon (GoAmazon2014/5) field campaign was conducted from January 2014

through December 2015.[170-171] The GoAmazon campaign was developed with multiple scientific

objectives, two of which involve the biogenic and anthropogenic interactions studied here.

3.3 Experimental

    3.3.1 Sampling site description. As part of the GoAmazon field campaign, two

Intensive Operating Periods (IOPs) were conducted during 2014, with IOP2 taking place during

the dry season from the 15th of August through the 15th of October 2014.[170] This campaign was

conducted over central Amazonia with multiple sampling sites around the city of Manaus (Figure

3.1). Northeasterly trade winds in this region dictate the general wind direction over the area and

so the sampling sites were located with this in mind. These trade winds carry marine aerosols

from the ocean inland and, during the wet season, can also carry supermicron mineral dust from

the Sahara.[172] For the wet season, secondary organic aerosols (pure liquid or with a

soot/inorganic core) dominate the submicrometer size range.[129, 173-174] During the dry season,

however, a large fraction of the aerosol population can be attributed to large scale biomass

burning.[166]

    For this study, particle samples from three sampling sites were studied: The Amazon Tall

Tower Observatory (ATTO; T0a), the Terrestrial Ecosystem Science site (site ZF2; T0t), and the

Atmospheric Radiation Measurement (ARM) site located near Manacapuru (site T3). The

ATTO site is located approximately 150 km upwind of Manaus and serves as a background site.

During the wet season near-pristine conditions can be observed here but, because the dry season

is dominated by biomass burning particles, the ATTO site will serve as a regional background

rather than a background of pure biogenic particles as might be expected.[175] The ZF2 site is

located about 140 km directly downwind of the ATTO site. The final site, T3, is 70 km

downwind of Manaus and often experiences the pollution plume from Manaus.[170-171] Site

locations and characteristics are presented in Martin *et al.*, 2016.[170]
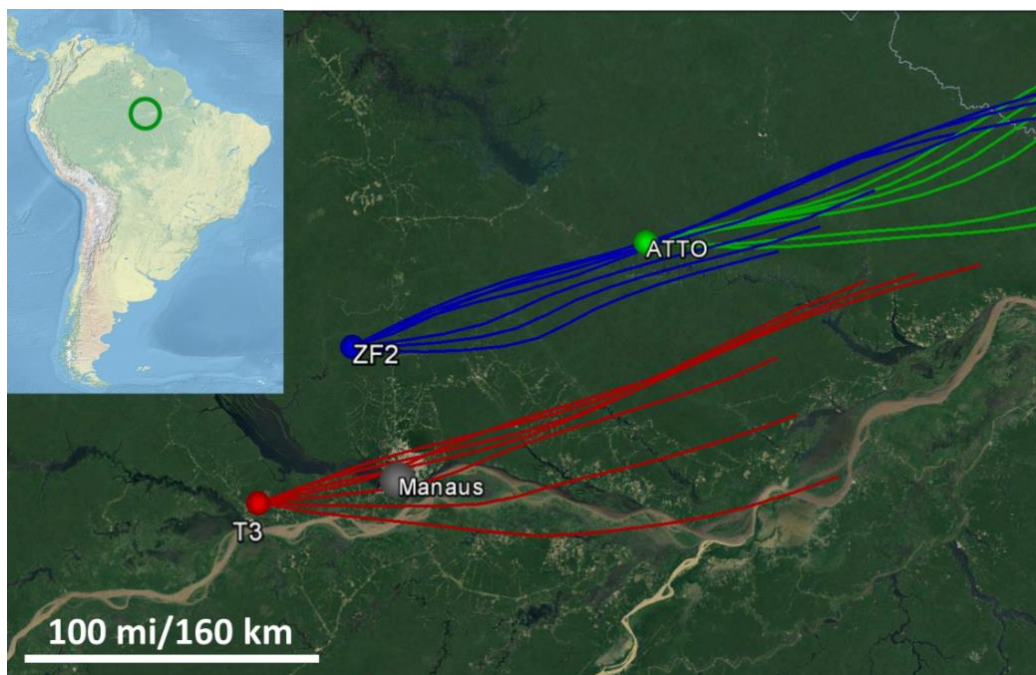
Figure 3.1 Positions of the three sampling sites located around the city of Manaus. Also shown are representative National Oceanic and Atmospheric Administration (NOAA) Hybrid Single Particle Lagrangian Integrated Trajectory Model (HYSPLIT) back trajectories (14/Sept from 9am to 12pm shown). (Inset) Overview map of South America with the region of interest circled. (For more information, please see Andreae *et al.*, 2015, Artaxo *et al.*, 2013, Martin *et al.*, 2016).[164, 170, 175]

3.3.2 Sample collection. At the three sampling sites, atmospheric particle samples were

collected on silicon nitride (Si_3N_4) membranes overlaid on a 5 x 5 mm silicon chip frame with a

central 0.5 x 0.5 mm window (100 nm thick membrane, Silson Inc.). Samples were collected using

a Micro-Orifice Uniform Deposit Impactor (MOUDI, MSP MOUDI-110) on the dates and times

shown in Table 3.1. HYSPLIT back trajectories were examined for each sampling period to

confirm the wind patterns seen in Figure 3.1. These samples were then analyzed sequentially with

the two spectromicroscopy techniques discussed in the following sections.

Table 3.1 List of samples examined for this study. The nominal size range for Micro-Orifice Uniform Deposit Impactor (MOUDI) stage 7 is 0.56–0.32 µm and stage 8 is 0.32–0.18 µm.

Site	Date (2014)	Time Period (Local Time)	MOUDI Stage	# of Analyzed Particles
ATTO	14–15 Oct	19:00 (14 Oct)–19:00 (15 Oct)	7	501
T3	12–13 Sept	Night 18:00–6:00	7	334
	13 Sept	Day 8:00–12:00	7	279
	13 Sept	Day 8:00–12:00	8	59 [1]
	14 Sept	Day 9:00–12:00	7	182
	14 Sept	Day 9:00–12:00	8	50 [1]
ZF2	3–6 Oct	11:00 (3 Oct)–11:00 (6 Oct)	7	315
	6–8 Oct	14:00 (6 Oct)–12:00 (8 Oct)	7	309
	6–8 Oct	14:00 (6 Oct)–12:00 (8 Oct)	8	967

[1] Low particle counts are due to low particle loading of microscopy samples and time constraints. The # symbol is used to represent the word number here.

3.3.3 STXM data collection and image processing. Samples were first imaged at the STXM beamline 5.3.2.2 at the Advanced Light Source (ALS).[91] The energy range of this STXM (200-600 eV) end station enables the quantitative study of carbon, nitrogen, and oxygen. Energy selected soft X-rays were focused down to a ~30 nm spot size and directed onto the sample surface. After a suitable 15x15 µm region was located, the sample stage was then raster scanned, with 40 nm steps, using piezo-electric stages to capture an image at a specific energy. This process was then repeated at multiple photon energies to produce a stack of images with an absorption spectrum associated with each 40x40 nm pixel. For each element, photon energies were chosen before and after the k-shell absorption edge: 278 and 320 eV for carbon, 400 and 430 eV for nitrogen, and 525 and 550 eV for oxygen.[92] Additional images were also taken near the carbon edge at 285.4 and 288.5 eV, for the RC=CR and RCOOR C1s→π* transitions respectively, in order to partly characterize the molecular speciation of carbon.[100]

Any displacement between images within a stack is corrected by a routine based on Guizar-Sicarios' image registration algorithm.[97] Regions within a given stack were then identified as particles or substrate using Otsu's method on that stack's average intensity image over all 8 energies.[98] Background subtraction of a given element's pre-edge intensity image from its post-edge image is then performed to account for any absorbing species not attributed to that element.

The recorded intensity at each pixel determined to be a particle was converted to optical density using:

$$OD = -\ln\left(\frac{I}{I_o}\right) \tag{3.1}$$

where OD is optical density, I is intensity of the pixel, and I_o is the background intensity. This is followed by a conversion to mass with the following formula:

$$m = \frac{OD * A}{\mu_{post} - \mu_{pre}} \tag{3.2}$$

where m is the mass of a specific element at that pixel, A is the area of that pixel, and μ_{pre} and μ_{post} refer to the mass absorption coefficients for that specific element before and after the absorption edge, respectively.

Previously developed algorithms for determining the speciation of carbon using 278.0, 285.4, 288.5, and 320.0 eV were applied to each field of view (FOV) as well. This mapping technique uses a series of thresholds to identify inorganics, soot, and organic carbon. Total carbon is taken to be $OD_{320} - OD_{278}$, pixels with an OD_{278}/OD_{320} ratio 0.5 or greater are rich in inorganics, and pixels with an elevated (0.35) ratio of sp^2 bonding compared to total carbon $(OD_{288.5} - OD_{278})/(OD_{320} - OD_{278})$ are indicative of soot.[100]

3.3.4 SEM/EDX data collection. The same sample windows previously imaged with STXM were imaged again with a computer controlled scanning electron microscope (FEI, Quanta 3D FEG) coupled with energy dispersive X-ray spectroscopy (CCSEM/EDX). The SEM utilized a field emission tip to produce an electron beam which was directed and focused onto a sample with an accelerating voltage of 20 kV which can cause core shell atomic electrons to be ejected from the sample. Higher shell electrons then relax into the newly created orbital hole, releasing an elementally characteristic photon recorded by an energy dispersive X-ray detector (EDAX PV7761/54 ME with Si(Li) detector). As the electron beam was scanned over the sample, the transmitted electron image was used to identify the exact same FOVs from the previous STXM images. Once a FOV previously analyzed with STXM is located, a 10,000x image (30 nm/pixel resolution) was captured. This image combines both transmitted and backscattered electron images to improve particle detection.[113] A threshold contrast level was then set to identify which areas of the collected image counted as particles using the "Genesis" software from EDAX, Inc. A software filter was then applied which discounts particles that are too small (e.g. noise spikes) or too large (e.g. multiple nearby particles counted as a single large particle). The electron beam was then directed towards each identified particle in sequence and an EDX spectrum was collected. Afterwards software was used to fit the peaks of eleven relevant elements selected for this study: Na, Mg, P, S, Cl, K, Ca, Mn, Fe, Ni, and Zn. Some elements of interest have been included in the spectral fit, but omitted from quantitation, including Al, Si, and Cu due to background sources of these elements: 1) the STXM sample holder where the Si_3N_4 windows sat was made of Al and was inserted into the SEM as well, 2) the mounting stage that holds samples inside the microscope was fabricated from beryllium-

copper alloy, 3) the EDX data was collected using a Si(Li) detector with a 10 mm^2 active area.

Each of these circumstances could contribute background signal for the elements in question.

After data has been collected from both SEM and STXM, individual particle mass

information is contained in two sets of images: one from STXM and one from SEM. Due to

differing contrast mechanisms, image resolution, and other factors, particles do not necessarily

appear the same between images taken with the two techniques. The manual matching of

particles was performed using pattern recognition to ensure proper alignment of the image sets

from both techniques.

3.3.5 Quantifying Higher Z Elements. Using the aforementioned methods, STXM

yields quantitative, absolute mass information on a sub-particle basis. SEM/EDX is more

limited in this aspect, being quantitative for elements with Z>11 (Na) but only semi-quantitative

for C, N, and O.[113] Due to the EDAX software used for EDX data collection and analysis, there

is an additional caveat to the quantitation of Z>11 elements: the software reports only the relative

mass percentages compared to the elements chosen during data processing. In order to properly

quantify the mixing state, the absolute mass of each element in each particle is necessary. To

determine these absolute masses, a system of equations was set up using the following equation

types:

$$OD_i = \rho t \sum_{a=1}^{A} f_a \mu_{a,i} \tag{3.3}$$

$$\frac{f_x}{f_y} = \frac{rel.\%_x}{rel.\%_y} \tag{3.4}$$

$$\sum_{a=1}^{A} f_a = 1 \tag{3.5}$$

For each pixel, OD_i is the optical density taken at energy i, ρ is the density and t is the thickness

of the sample (at that pixel), f_a is the mass fraction of element a, and $\mu_{a,i}$ is the mass absorption

coefficient of element a at energy i. Equation 3.4 is a general relationship which equates the

ratio of two absolute mass fractions (f_x and f_y) with the ratio of relative mass percentages ($rel.\%_x$

and $rel.\%_y$) produced by the EDAX software. Equation 3.3 utilizes the quantitative nature of

STXM whereas the relative mass percent of elements with Z>11 were used in equation 3.4 to

combine the quantitative abilities of SEM/EDX. This system was then solved for the 14 absolute

mass fractions (f_a) of each element chosen in this study.

Equation 3.5 is an assumption which is valid when the 14 elements analyzed comprise

close to 100% of the particle's composition. Here, systematic error in the calculated mass

fractions of specific particles can be introduced in particles where elements not considered

represent a significant portion of that particle's mass (e.g. mineral dust and Si or Al). During the

Amazonian dry season, Al and Si represent 0.3% and 0.4% of the average fine mode particle

mass.[176] This mass fraction error becomes negligible, however, when the ensemble diversity

values or mixing state index is considered due to the overwhelming mass of C, N, and O in each

particle.

After both sets of images are matched and the corresponding light and heavy element

information has been processed, quantitatively, mass information for each FOV is contained in

sets of maps, one for each element analyzed.

3.3.6 Mixing State Parameterization. The method of parameterizing mixing state used

here is based on calculating mass fractions for different groupings of the individual components

defined and is reproduced from Riemer and West.[41] The absolute mass of a given component a,

within a given particle i, is labeled as m_i^a where $a = 1, ..., A$ (and A is the total number of

components) and $i = 1, ..., N$ (the total number of particles). From this, the following relationships are established:

$$\sum_{a=1}^{A} m_i^a = m_i \ (Mass \ of \ i^{th} \ particle) \tag{3.6}$$

$$\sum_{i=1}^{N} m_i^a = m^a \ (Mass \ of \ a^{th} \ component) \tag{3.7}$$

$$\sum_{a=1}^{A} \sum_{i=1}^{N} m_i^a = m \ (Total \ mass \ of \ sample) \tag{3.8}$$

Mass fractions are then established from these relationships with:

$$f_i = \frac{m_i}{m}, \ \ f^a = \frac{m^a}{m}, \ \ f_i^a = \frac{m_i^a}{m_i} \tag{3.9}$$

Where f_i is the mass fraction of a particle within a sample, f^a is the mass fraction of component a within a sample, and f_i^a is the mass fraction of component a within particle i.

These mass fractions are used to calculate the Shannon entropy (also called information entropy) for each particle, each component, and for the bulk using Equations 3.10, 3.11, and 3.12 respectively.

$$H_i = \sum_{a=1}^{A} -f_i^a \ln f_i^a \tag{3.10}$$

$$H_\alpha = \sum_{i=1}^{N} f_i H_i \tag{3.11}$$

$$H_\gamma = \sum_{a=1}^{A} -f^a \ln f^a \tag{3.12}$$

Each type of mass fraction can be thought of as a probability, and thus the collection of mass fractions defines a probability distribution. The Shannon entropy of a probability distribution quantifies how uniform the distribution is. Shannon entropy is maximized if every element in the distribution is equally probable, and the entropy decreases the more likely any individual element becomes.[41] With this information entropy, diversity values are defined with the following equations

$$D_i = e^{H_i}, \ D_\alpha = e^{H_\alpha}, \ D_\gamma = e^{H_\gamma} \tag{3.13}$$

The diversity values contain the same type of information, but represent it in another way. Each diversity value represents the effective number of species (weighted by mass) within a given population (i.e. D_i represents the number of species within a specific particle, D_α is the average number of species within any given particle, and D_γ represents the number of species within the entire sample). From these diversity values the mixing state index is defined as

$$\chi = \frac{D_a - 1}{D_\gamma - 1} \tag{3.14}$$

This definition compares how many species exist, on average, within individual particles, with the total number of species identified in the sample. χ is at a minimum of 0 when D_α is 1, corresponding to each particle being comprised of exactly one species. A mixing state index of 1 occurs when D_α and D_γ are equal, meaning that each particle has the same composition as the bulk sample.

3.3.7 Error in Mixing State Index, χ. The measurement uncertainty of χ due to STXM, EDX, or the system of equations was found to be insignificant compared to the statistical uncertainty of χ within each cluster and thus statistical uncertainty is all that is considered here. To determine this uncertainty, the statistical uncertainty in D_α, and D_γ were found separately.

Determining statistical uncertainty in D_γ starts with f^a from Equation 3.9. From Riemer and West,[41] f^a is a ratio of the total mass of the ath component and the total mass of the sample, however this is equivalent to the ratio of the mean mass of the ath component and the mean mass of particles within the sample:

$$f^a = \frac{m^a}{m} = \frac{\sum_{i=1}^{N} m_i^a}{\sum_{i=1}^{N} \sum_{a=1}^{A} m_i^a} = \frac{\frac{1}{N}\sum_{i=1}^{N} m_i^a}{\frac{1}{N}\sum_{i=1}^{N} \sum_{a=1}^{A} m_i^a} = \frac{\overline{m^a}}{\overline{m}} \tag{3.15}$$

where $\overline{m^a}$ is the mean mass of the ath component and $\overline{m}$ is the mean mass of particles within the sample. From this, the standard error (for a 95% confidence level) can be determined for $\overline{m^a}$ and $\overline{m}$ which is then propagated through Equations 3.9 - 3.13.

The statistical uncertainty in D_α was found by first rearranging and combining Equations 3.11 and 3.13:

$$H_\alpha = \sum_{i=1}^{N} f_i \ln D_i \tag{3.16}$$

and, because this takes the form of an expected value $E(x) = \sum f_x x$, the error in H_α can be found with Equation 3.15 and then propagated with Equation 3.16 to determine the error in D_α.

3.3.8 k-Means clustering. All analyzed particles were combined and a k-means clustering algorithm was then used to group particles into clusters.[177] A vector of 18 variables were used for k-means clustering: the quantitative elemental mass fractions composition of the 14 elements chosen, Area Equivalent Diameter (AED),[1] D_i, the mass fraction of carbon attributed to soot, and the area fraction of the particle dominated by inorganics. In this way particles were clustered based on size, elemental composition, as well as on how carbon speciation was distributed. The square root of these parameters was used in the clustering algorithm to enhance trace elements in accordance with Rebotier *et al.*[178]

The correct number of clusters was initially chosen based on a combination of two common methods: the elbow method, and the silhouette method.[179] Using these two methods, 12 clusters were identified.

3.4 Results

As a general trend, during the dry season, the whole Amazon Basin experiences a significantly higher aerosol number concentration and $CO_{(g)}$ concentration compared to the wet season, largely due to in-Basin fires.[166, 175] Furthermore, in addition to biomass burning, emissions from Manaus are often observed at the T3 site (downwind of Manaus), sporadically at the ZF2 site (upwind but near the city) and rarely at ATTO (upwind and ~170 km away). The aerosol and $CO_{(g)}$ concentrations on 14/Sept are elevated, suggesting that this sampling period experienced a heavier pollution plume. Nitrate concentrations do not show much difference between site T3 and ATTO. The night of 12/Sept does exhibit a slightly greater nitrate concentration, however. Ammonium levels for all sampling periods were fairly consistent whereas particle chloride levels exhibited more variability. The 12/Sept night sample had an elevated chloride concentration owing, in part, to decreased temperature and increased relative humidity allowing the condensation of $HCl_{(g)}$ onto aerosols.[180] Site T3 also contains particles with enhanced sulfate and organic concentrations compared to the ATTO site. Levels of ozone at T3 vary significantly, both from each other and from the monthly sample-time average. The BC levels at ZF2 are similar to those at ATTO and both sites exhibit BC levels consistently lower than those seen at T3. However, temporary enhancements in BC due to emissions from Manaus have been observed previously at ZF2.[181]

Table 3.2 Peripheral data during sampling times for each sampling site. Averages listed are for the given sampling period, averaged over the entire month (e.g. the average particle concentration between 8am and 12am averaged over the entire month). Ammonium, Chloride, Organics, Sulfate, and Black Carbon (BC) pertain to aerosol measurements whereas CO(g) and O3(g) are gas phase measurements.

	T3						ZF2				ATTO	
	12/Sept (pm)	Avg.	13/Sept (am)	Avg.	14/Sept (am)	Avg.	3-6/Oct	Avg.	6-8/Oct	Avg.	15/Oct	Avg.
Particle Conc. (cm-3)	2365[10]	3444[10]	2356[10]	3444[10]	5770[10]	3421[10]	-	-	-	-	1143[11]	1431[11]
Ammonium (µg m-3)	0.28[1]	0.45[1]	0.33[1]	0.42[1]	0.34[1]	0.42[1]	-	-	-	-	0.23[2]	0.20[2]
Chloride (ng m-3)	24[1]	20[1]	14.9[1]	27[1]	17.0[1]	27[1]	-	-	-	-	14.4[2]	14.9[2]
Nitrate (µg m-3)	0.28[1]	0.16[1]	0.11[1]	0.19[1]	0.20[1]	0.19[1]	-	-	-	-	0.16[2]	0.15[2]
Organics (µg m-3)	14.1[1]	10.7[1]	7.9[1]	10.0[1]	7.6[1]	10.0[1]	-	-	-	-	3.8[2]	4.4[2]
Sulfate (µg m-3)	0.71[1]	1.4[1]	1.0[1]	1.1[1]	0.86[1]	1.1[1]	-	-	-	-	0.53[2]	0.61[2]
CO(g) (ppb)	178[3]	210[3]	211[3]	257[3]	558[3]	254[3]	178[4]	169[4]	159[4]	168[4]	141[4]	138[4]
O3(g) (ppb)	7[5]	19[5]	17[5]	7[5]	4[5]	8[5]	17[6]	13[6]	12[6]	13[6]	-	-
BC (µg m-3)	0.8[7]	0.9[7]	1.0[7]	1.0[7]	1.2[7]	1.0[7]	0.5[8]	0.4[8]	0.6[8]	0.4[8]	0.5[9]	0.4[9]

[1]Aerosol Mass Spectrometer (AMS), [2]Aerosol Chemical Speciation Monitor (ACSM), [3]ARM/Mobile Aerosol Observatory System (MAOS) Los Gatos ICOS™ Analyzer, [4]Picarro Cavity Ringdown Spectrometer (CRDS), [5]ARM/MAOS Ozone Analyzer, [6]Thermo 49i, [7]ARM/AOS Aethalometer, [8]MultiAngle Absorption Photometer (MAAP)-5012, [9]MAAP, [10]ARM/MAOS Scanning Mobility Particle Sizer (SMPS), [11]SMPS

Figure 3.2 shows an example FOV and the type of data calculated for all three sites. Each particle has an OD map (which is proportional to mass, refer to Equation 3.2) for C, N, and O as well as a C speciation map. In Figure 3.2 the STXM grayscale image shown is the average intensity map over the four C edge images. There is a correlation between the brightest spots and the identification of soot in the C speciation map. This speciated image is possible due to the sub-particle spatial resolution achievable with STXM mapping, which is highlighted in the C, N, and O maps. Potential inter-site differences can be seen in this figure: the ATTO sample shows large inorganic inclusions coated by organics along with Na, Mg, and Cl representing the bulk of the higher Z elements. The particles present at ATTO also often look like either inorganic aerosols from biomass burning events or small biogenic K salt particles (due to the KCl or NaCl inorganic cores), or secondary organics, with a few particles appearing to be sea spray.[182-184] The ZF2 sample has a consistent circular morphology with appreciable mixing between the three carbon species. ZF2 particles often look amorphous with some particles appearing to be sulfate based aerosols.[185] Lastly, the T3 sample is the most varied in terms of

morphology and in elemental composition with S, P, and K all present in many of the particles sampled. Unsurprisingly, soot inclusions are much more common in the T3 sample. Particles from this site often look like biomass burning particles with a few fractal soot particles as well.[186] It is important to keep in mind that the particle morphologies presented have possibly changed from their original state when collected. This change could be due to the impaction of particles during sampling, or the changes in relative humidity experienced as these particles are collected, stored, transported, and placed in vacuum before STXM or SEM images can be obtained.

The SEM grayscale image shows the slightly different views presented by the two techniques, with particle shapes appearing different between them along with a higher spatial resolution image (10 nm vs. 40 nm with STXM). Soot inclusions identified in the C speciation map are also seen as bright spots in the SEM grayscale image in addition to many of the inorganic inclusions.[113] From the EDX data collection, mass fraction maps for each element (on a per-particle basis) were used to calculate individual particle diversity (D_i) values for each particle. Another aspect of the maps is the varying background level between SEM images, seen especially in the high background of the ZF2 image. This is a consequence of the brightness and contrast levels being set before EDX acquisition and was performed to ensure the maximum number of particles were detected by the CCSEM particle detection software.

(a)

(b)

(c)
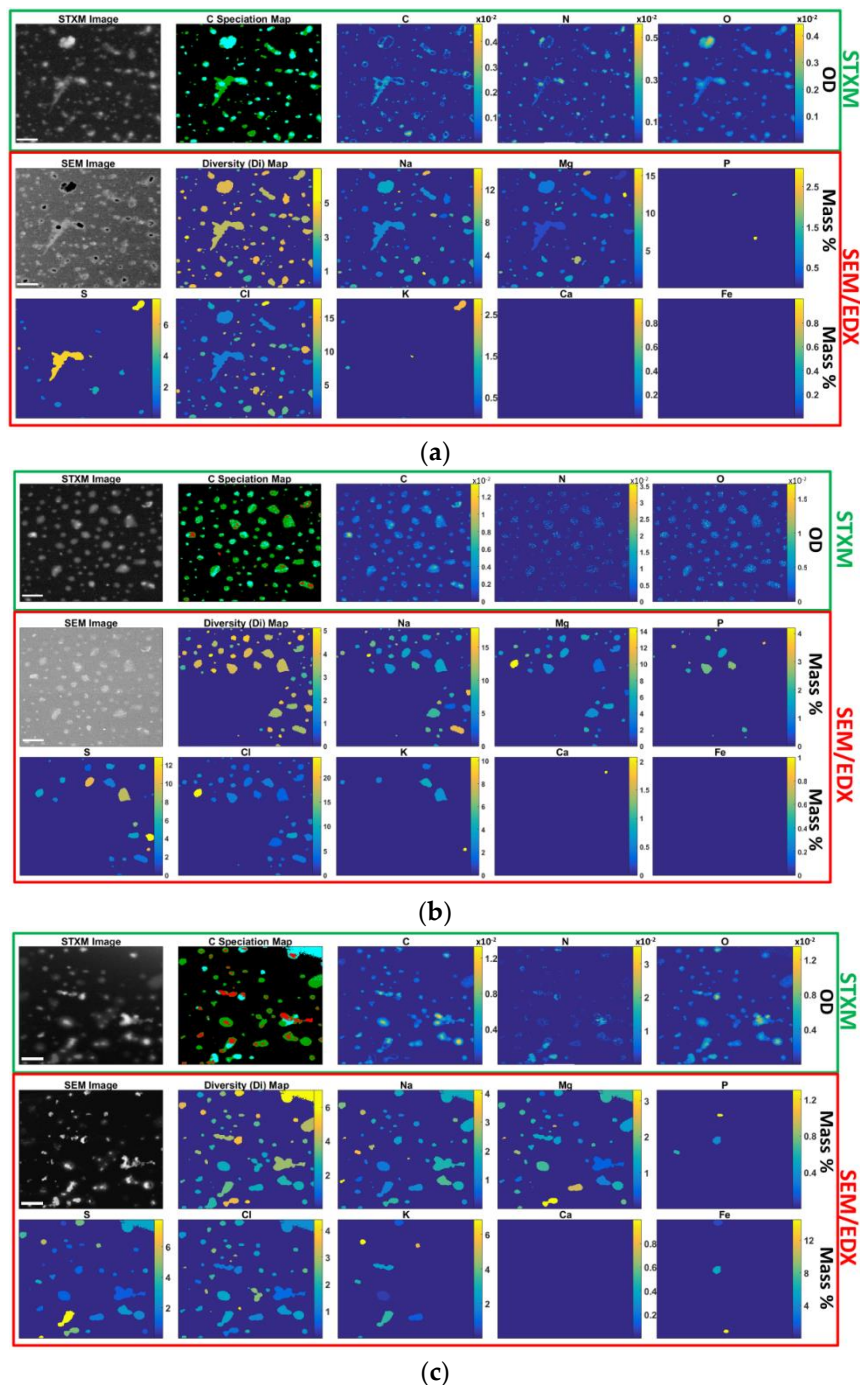
Figure 3.2 Raw and processed image maps for selected FOVs from each site. a) the ATTO site collected on 15/Oct/2014, b) the ZF2 site collected on 3-6/Oct/2014, and c) the T3 site collected on 13/Sept/2014. Raw images for STXM and SEM are shown (with 2 µm scale bar in bottom left) along with false color maps showing the sub-particle (for C, N, and O) or per-particle (for higher Z elements) mass distribution. Also shown is a color coded carbon speciation map showing soot (red), inorganic (teal), and organic (green) carbon. The calculated individual particle diversity (Di) is also shown. Note the large spot in the upper right corner of the T3 sample, this was most likely the edge of the Si_3N_4 window and the spot was removed from calculations. Also note the empty lower left corner in the ZF2 sample EDX data lacking for those particles, because of this they were removed. Zn, Mn, and Ni maps are omitted here as they were not detected in these FOVs.

3.4.1 Clustering and source attribution. For each of the 12 clusters, determined by the

k-means algorithm, a random representative sample of 40 particles (taken from any sample or

sampling site) was selected for the images shown in Figure 3.3. The average elemental

composition of each cluster is shown in Figure 3.4 along with the fraction of each cluster

collected at the three sampling sites. Finally, Table 3.3 outlines the assigned colors and labels, as

well as some relevant descriptive statistics for each cluster. As can be seen in the average

particle diversity column in Table 3.3, most clusters have a D_α value near either 2.4 or 3.6 (with

a single exception). These two values define the "low" or "high" diversity referred to in the

cluster names and are discussed in more detail in section 3.4.5. A similar source apportionment

was discussed in a previous SEM based study, however, it was conducted during the wet season

when biogenic aerosols dominate.[129] During the dry season, these biogenic particles are still

present but are overwhelmed by biomass burning derived aerosols.

One aspect of Figure 3.4 that is notable is the ratio of elemental Cl to S in each of the

clusters shown. From the EDX spectroscopy data presented here, the mass fraction of Cl is often

greater or at least similar to that of S. This is apparently contradicted by Table 3.2, where the

concentrations of chloride are an order of magnitude less than the concentrations of sulfate.

There are, however, a few extenuating circumstances for this comparison. Firstly, the chloride

level in Table 3.2 is that of non-refractory material owing to the AMS's method of volatilizing

particles with ~600 °C. This is well below the vaporization temperature for NaCl and KCl, two

major sources of Cl (and inorganics in general). Hence, Table 3.2 AMS data underestimates Cl

mass fractions. Another correction to allow direct comparison is to change concentration of

sulfate to S by multiplying by the ratio of molar masses (~32/96), reducing the concentrations

seen in Table 3.2 to about one third. The second circumstance is the potential for beam damage

using the two sequential microscopy techniques here. Some of the inorganic inclusions/cores

detected using STXM/NEXAFS spectroscopy may be particularly sensitive to electron beam

damage. These sensitive inorganics (particularly ammonium sulfate) could have been volatilized

during the scanning/locating phase of SEM and therefore would not be well characterized with

subsequent EDX spectroscopy. This carries two consequences: a possible underestimation in the

mass fraction of S, and the identification of inorganic regions with STXM without the detection

of many inorganic elements to explain the inclusions. This issue of S quantification is further

highlighted when the S/Cl ratios in Figure 3.4 are compared with previous Particle Induced X-

ray Emission (PIXE) measurements which report aerosol S concentrations an order of magnitude

greater than Cl concentrations.[57, 187] In addition to PIXE, they used factor analysis to determine

broad particle classes including soil dust, biogenic, marine, and biomass burning classes. One

finding of relevance is the high degree of correlation between biogenic particles and S

concentration.[187] For the current work, this could suggest an underestimation in the number of

clusters hypothesized to contain biogenic particles.
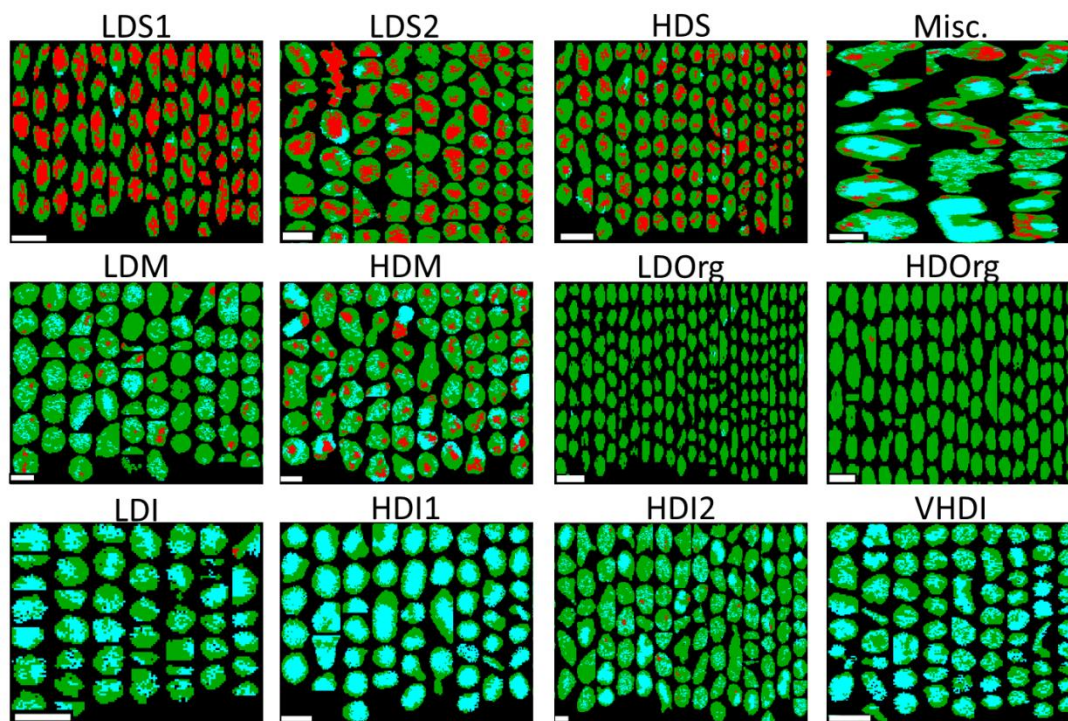
Figure 3.3 Random sample of ~40 particles from each cluster. This shows sub-particle carbon speciation as either soot (red), inorganic (teal), or organic (green). 1 μm scale bars are shown in the bottom left of each image. Cluster identification (image labels) is provided in Table 3.3.
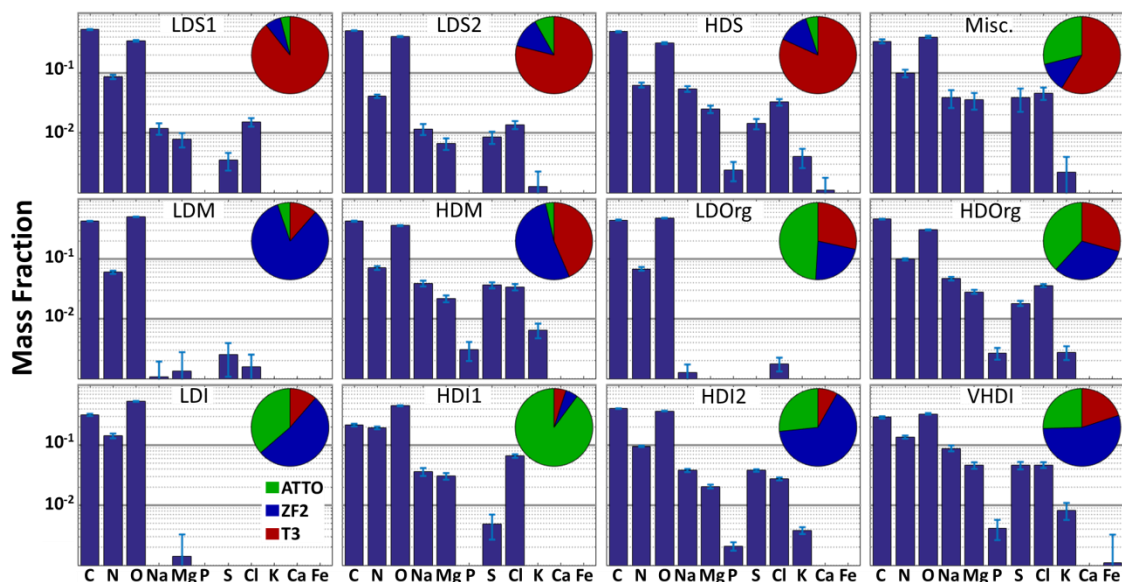
Figure 3.4 Average elemental composition of each cluster. Each plot has an inset pie chart showing each cluster's representation at the three sampling sites: ATTO (green), ZF2 (blue), and T3 (red). Al and Si were not included due to the background from the Al sample holder and the Si_3N_4 substrate. Cluster identifications (image labels) are provided in Table 3.

Table 3.3 Cluster identifying information

Cluster Name	Label	Avg. Diversity, Dα (Std Err)	CED, μm (Std Err)	O/C Ratio [2]	N
Sub-μm Low Diversity Soot	LDS1	2.67 (0.24)	0.37 (0.01)	0.49	261
Super-μm Low Diversity Soot [1]	LDS2	2.74 (0.29)	1.04 (0.06)	0.60	180
High Diversity Soot	HDS	3.49 (0.51)	0.52 (0.02)	0.48	183
Low Diversity Organics	LDOrg	2.36 (0.08)	0.29 (0.01)	0.81	540
High Diversity Organics	HDOrg	3.49 (0.36)	0.34 (0.01)	0.50	647
Low Diversity Inorganics	LDI	2.57 (0.17)	0.39 (0.02)	1.26	160
High Diversity Coated Inorganics	HDI1	3.87 (0.60)	0.62 (0.03)	1.57	201
High Diversity Inorganics	HDI2	3.75 (0.26)	0.75 (0.02)	0.69	655
Very High Diversity Inorganics	VHDI	4.83 (1.92)	0.45 (0.03)	0.86	212
Low Diversity Mixed	LDM	2.43 (0.13)	0.91 (0.04)	0.88	221
High Diversity Mixed	HDM	3.73 (0.72)	0.94 (0.04)	0.63	209
Miscellaneous	Misc.	3.83 (2.10)	2.35 (0.22)	0.89	47

3.4.1.1 Soot clusters (LDS1, LDS2, HDS). The HDS cluster is characterized by a thick organic coating around a soot core. The elevated levels of S and K could indicate that this cluster originated from biomass burning[34] This combined with the overwhelming majority of particles being found at site T3 suggest these are anthropogenic in nature. This cluster's

enhanced mass fraction of Na, Cl, Mg, and S as well as the appreciable amount of P and K contribute to the higher particle diversity seen in this cluster.

In addition to LDS1 lacking the P, K, and Ca that HDS has, LDS1 also has a smaller amount of Na, Mg, S, and Cl which results in the lower average particle diversity. The decreased abundance of K and Cl may indicate urban combustion sources such as diesel engines as opposed to biomass burning.[182] The coatings of organics around the soot cores seen in this cluster are much thinner compared to other soot containing clusters suggests that particles in this cluster are less aged.[188] The vast majority of particles from this cluster type are found at site T3; given that T3 is downwind of Manaus, this suggests fresh urban soot emissions as this cluster's source.[171]

The large and multiple soot inclusions and the presence of fractal soot are indications that LDS2 is comprised of particles with a contribution from combustion.[46, 189] Particles in LDS2 are found mostly at site T3 which points towards Manaus being the source of these aerosols. The sometimes substantial organic coating on many of these particles is most likely due to condensation as fresh aerosols from Manaus travel to the T3 sampling site. With the exception of the one night time sample, all T3 samples were collected during the mid to late morning (~9am to 12pm) which has been seen in other urban cities to correspond to an increased in aged soot over fresh soot owing to the increase in photochemistry.[154]

3.4.1.2 Organic Clusters (LDOrg, HDOrg). HDOrg is comprised of small particles with their carbon being entirely organic dominant. This cluster has a substantial amount of the heavier elements (Z=11 (Na) and above) driving the diversity up. The presence of P specifically is important as these elements, coupled with the carbon speciation, suggest that the particles from this cluster are biological in origin.[57] The HDOrg cluster also contains an appreciable amount of

K and, given that one sample was taken at night, could include biological particles derived from fungal spores.[184]

LDOrg is similar in carbon speciation, morphology, and size but lacks the heavier elements contained in HDOrg. The almost entirely C, N, and O composition, small size, and the organic carbon speciation suggest that particles in this cluster are secondary organic aerosols. This is supported by a slight majority of particles in this cluster coming from the general direction of the ATTO site, where a dominant appearance of biogenic secondary organic aerosols and a smaller influence from anthropogenic emissions is expected.

As discussed further on in section 3.4.2, both organic clusters are unique in that they make up a sizeable fraction of particles at all sampling sites.

3.4.1.3 Inorganic clusters (LDI, HDI1, HDI2, VHDI). Other than C, N, O, and trace levels of Mg, no other elements are observed in the LDI cluster. Carbon speciation, however, shows a clear inorganic core with an organic coating. This leaves only a few options for the identity of the inorganic cores seen here. One possibility is that the inorganic core is composed of elements not analyzed here, such as Si or Al. Due to the Al mounting plate and the Si(Li) detector used, we are not able to quantitatively detect Al and Si. However, a more likely possibility is that, as mentioned above, the inorganic cores that were initially detected with STXM were particularly sensitive to electron beam damage leading to these sensitive inorganics (possibly ammonium sulfate) being poorly characterized by EDX.

HDI1 is characterized by large, vaguely cubic, inorganic inclusions coated with organics. This cluster has a fairly high fraction of O, Na, and Mg while containing the highest amount of Cl of any cluster. The HD1 cluster is also unique in that particles in it were collected almost exclusively at the ATTO site. Because of this, we suspect these particles represent marine

aerosols.[190-192] Another possibility is that these particles represent primary biological particles associated with spore rupturing.[193] The organic coating here is substantial and is likely due to aging as aerosols are transported inland to the ATTO site.

HDI2 is characterized by many small inorganic inclusions speckled throughout the particles which are not as localized as with the HDI1 cluster. There are small soot inclusions and an increased presence of P, K, and S as compared to HDI1. These particles are mainly seen at the ZF2 site with a smaller portion present at ATTO. Thus it is possible that this cluster is also associated with spore rupturing but further investigation is needed to apportion this cluster.

The VHDI cluster is unique in that it possesses the highest D_α value of any of the clusters at 4.83, well above both the nominal "high diversity" value of 3.6 and the second highest D_α value of 3.83. This cluster also has a large statistical error of 1.92 (at a 95% confidence level) which could indicate multiple disparate groups are present in this cluster. This cluster is comprised mostly of particles from ZF2 but ATTO and T3 particles contribute substantially as well. The VHDI cluster's elemental composition is similar to that of HDI2 but with a decreased C and O mass fraction and an enhancement of the other elements, especially K (often seen in inorganic salt grains from biomass burning).[166, 194] Inorganics are seen both as large localized inclusions, and as many small inclusions speckled throughout the particle. This cluster's high diversity and larger statistical spread may also be indicative of the varied biomass burning fuels and burning conditions present.

3.4.1.4 Mixed clusters (LDM, HDM). The LDM cluster is characterized by all three carbon speciation types being present in many of the particles. The presence of inorganic inclusions along with the lack of heavier elements suggests ammonium nitrate (and possibly ammonium sulfate) as the identity of the inorganics. This cluster is seen almost entirely at the

ZF2 site which, along with its low diversity and few elemental constituents, may indicate a local aerosol source near site ZF2. In which case, particles would have little time or distance to age and scavenge new elements. The presence of soot in the LDM cluster might suggest these aerosols come from the same source as the HDM cluster.

The species of carbon found in the HDM cluster's particles are well mixed with soot, non-carbonaceous inorganic, and organic carbon found in varying ratios. The large soot inclusions, high diversity, and substantial presence of higher Z elements may point to an industrial or automotive origin. Although the sizeable representation of the HDM cluster at T3 supports this, a slightly larger representation is seen at site ZF2. This raises the possibility that some emissions from service vehicles driving to or past the ZF2 site, or nearby generators may be collected at the ZF2 site. Emissions from Manaus are not uncommon either and could account for this cluster's presence at ZF2.[173]

3.4.1.5 Miscellaneous (Misc.) Clusters. Particles placed in this cluster were most likely grouped due to their supermicron size rather than their composition or diversity. This cluster is comprised of some large rectangular crystals, particles which did not fit well into the other clusters, as well as cases of particles with multiple large inclusions (inorganic or soot) each encased within individual lobes.

This last particle type is possibly due to nearby particles being erroneously deemed a single particle by our detection algorithm because of overlap of the organic coating upon impaction. This grouping of multiple individual particles into agglomerations much larger than expected for the given MOUDI stage caused them to be placed in the Misc. cluster.

One notable particle type seen in this cluster is the collection of particles with a rectangular inorganic core with a small patch of organic carbon in the center. Some of these

inorganic cores wrap around the carbon center while some others have a side missing but they all retain the same basic shape. The elemental composition of the inorganic portion contains small amounts of Na and Mg, a relatively large amount of S along with most of the particle's N and O mass fraction. Looking back on the sample specific data, these particles are observed on the only night time sample that was collected. This, along with the particles being found mainly at site T3 could suggest an industrial process whose emissions become easier to identify at night when other sources of aerosols (automotive) experience a decrease. Fragments of ruptured biological particles also may be a possibility based on their elemental composition.[193]

3.4.2 Cluster type dependence on sampling site. The cluster contributions at each sampling site are shown in Figure 3.5 separated by stage. Although particles from all cluster types were seen at each location, some particle types were predominantly associated with a particular sampling site. The clusters labeled LDOrg, HDOrg, HDI1, and HDI2 account for a majority of the particles seen at the ATTO site. To account for a similar share of particles at site ZF2 one must consider the clusters labeled: HDI2, VHDI, LDOrg, HDOrg, LDM, and HDM. Site T3 requires: LDS1, LDS2, HDS, LDOrg, HDOrg, and HDM to be accounted for to define a similar portion of particles.
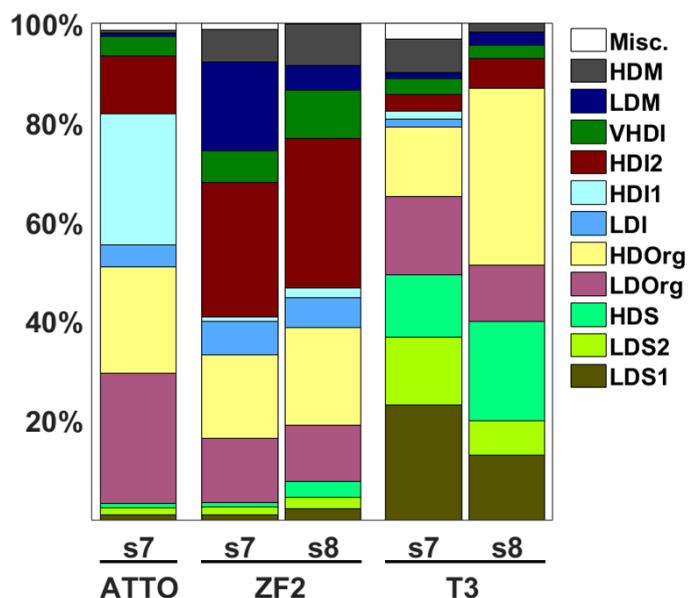
Figure 3.5 Contribution of the twelve particle-type clusters at each sampling site. Clusters were identified in the samples from stage 7 (nominal aerodynamic size range: 560-320 nm) and stage 8 (320-180 nm).

As the ATTO sampling site is less polluted and representative of biogenic aerosols, the presence of both organic clusters as well as two inorganic clusters with possible biogenic origins is expected. Conversely, the relative absence of soot clusters or the mixed clusters further highlights the ATTO site's remoteness from anthropogenic (urban) influences.

While the ZF2 site contains many of the same clusters present at the ATTO site, there are some notable differences. The presence of the HDI1 cluster is diminished (~1% as compared to ATTO's 26%), and both mixed clusters are seen in substantial amounts. The largest difference between the two stages is the enhancement of the LDM cluster in stage 7 data and the minor increase in all three soot clusters in stage 8 particles.

Site T3 shows the presence of many clusters, with all three soot clusters present in substantial amounts. This is expected as automotive exhaust or energy production through fuel oil burning will produce soot particles which travel to site T3.[195] Both organic clusters are

present with a slight enhancement in stage 8 particles. Because both organic clusters are seen in reasonable amounts at each sampling site, these particles may be part of the aerosol background inherent to sampling in a heavily forested region. Stage 8 particles are also devoid of LDI, HDI1, and Misc. clusters, but few of these were seen in stage 7 and so this absence may be due to insufficient sampling.

Another aspect of Figure 3.5 is how many clusters make up most of each site's aerosol population for which we use the following metric. Each site's cluster contribution is sorted in descending order and an effective number of clusters is found using $E(r) = \sum r f_r$ where r is the rank of each cluster's contribution to that site's population (with 1 assigned to the cluster with the largest contribution), f_r is the fraction of that site's population which cluster r accounts for, and E(r) is the effective number of clusters. This metric will vary, in this case, from 1 to 12 where the lower the effective number of clusters, the better a given site is characterized by fewer clusters. The values calculated from this metric are listed in Table 4. This metric highlights the increased diversity of sites T3 and ZF2 with respect to the ATTO site. Site ZF2's cluster composition is more varied. This is possibly due to specific events occurring during sampling, or by virtue of being closer to Manaus and therefore more susceptible to anthropogenic emissions. Site ZF2 samples were also collected over multiple days meaning some of the cluster variability may be due to the inclusion of both day and nighttime aerosols. This higher cluster variety could also be attributed to a local aerosol source as mentioned previously. Site T3 shows the highest cluster diversity due to its proximity to (and location downwind of) the anthropogenic center of Manaus.

Table 3.4 Effective number of clusters for the available sampling site and stage data. The lower the value, the fewer clusters needed to characterize a majority of the sample.

Stage Number	ATTO	ZF2	T3
Stage 7	2.90	3.46	3.80
Stage 8	-	3.37	2.86

3.4.3 Cluster Size Dependence. Although relatively few supermicron particles were collected, most clusters included some fraction of both sub- and supermicron particles. Only 1 cluster (Misc) was exclusively supermicron in size whereas three clusters (LDS1, LDI, LDOrg) included exclusively submicron particles. Referencing Figure 3.6, the only clusters observed in the supermicron size range were those labeled: Misc (located around 2 μm with a very small percentage), LDM, HDM, HDI2, LDS2, and HDI1. Supermicron particles in the clusters HDS, HDOrg, and VHDI particles were also observed, but in very small numbers. Many clusters that make up the supermicron range represent more aged species.

The submicron range is composed of many more clusters relative to the supermicron range. Many clusters in the submicron range were often labeled as less aged than the ones found in the supermicron range. This qualitative observation is supported by Figure 3.7 where there is an increasing trend in individual particle diversity (D_α) with increasing particle size and the notion that D_α is correlated with the extent of particle aging.
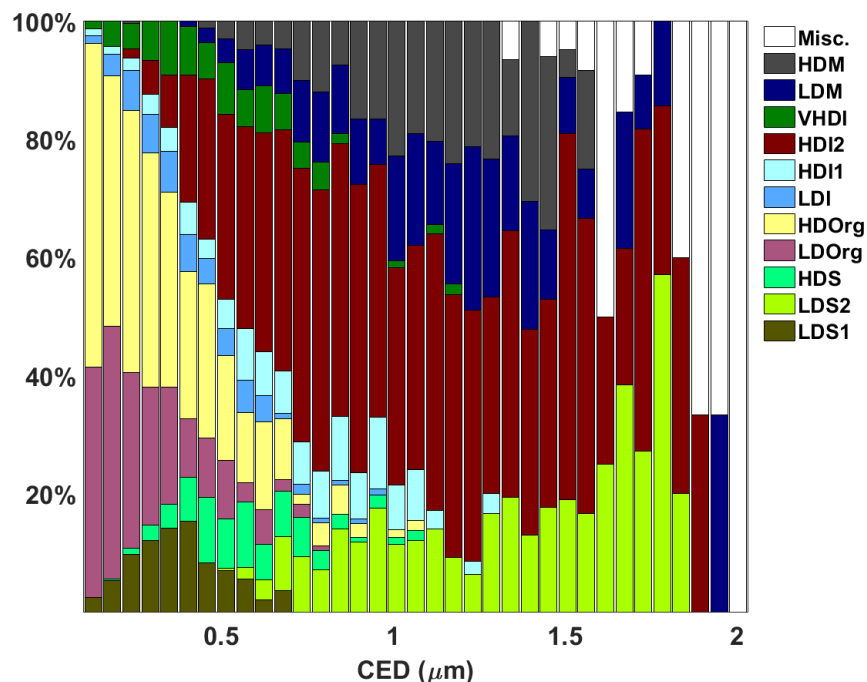
Figure 3.6 Cluster contribution overlain on a size distribution. Particles >2 μm have been omitted due to their very small abundance and to highlight submicron cluster composition.

3.4.4 Composition and diversity size dependence. Submicron particles, as seen in Figure 3.7, have a high fraction of C, N, and O. With Dα values, calculated for both sub- and supermicron particles being 3.3 and 3.4 respectively, submicron particles appear to be the least diverse. However, error analysis described below, renders this merely suggestive rather than conclusive. As particle size increases two things are observed: 1) average particle diversity increases slightly and 2) the fraction of inorganics increases. Because of the ubiquity of C, N, and O in aerosol particles, the average particle diversity will almost always be slightly above 3. Given the relatively constant ratios of C, N, and O, individual particle diversity is not dependent on these elements; with the exception of soot. Rather, it is mainly the presence of heavier elements which are responsible for any increase in diversity. These larger particles, often represented by more aged clusters like LDM, HDM, or HDI2, have had sufficient time and travel distance to acquire additional elements during the aging process. A similar conclusion was observed during the

Carbonaceous Aerosol and Radiative Effects Study (CARES) conducted in 2010 in California, where heavier elements appreciably affected the mixing state of particles and increased with size, while C, N, and O remained constant.[124, 129]
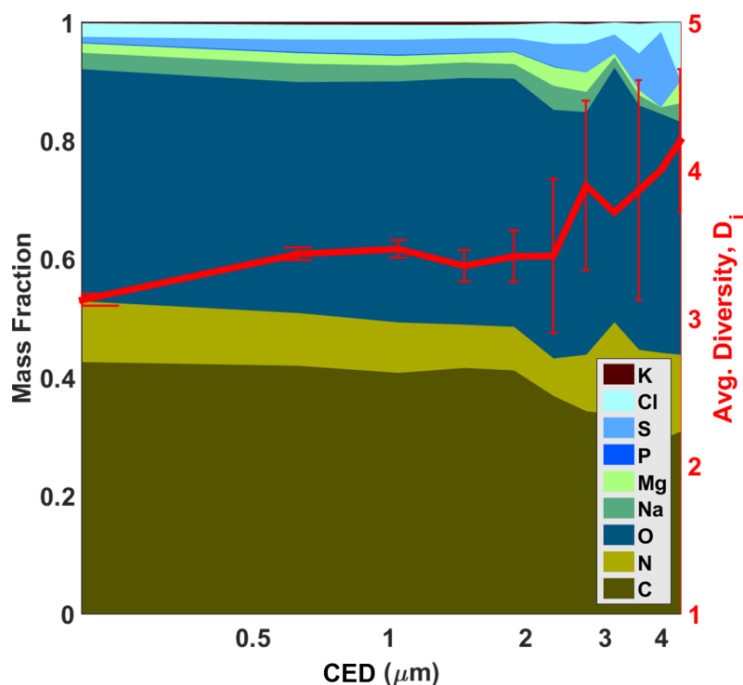
Figure 3.7 Elemental composition and average individual particle diversity Di (red trace) as a function of CED. Of note is that only 32 particles with diameters >2 µm were analyzed which is why this region is fairly noisy. Error bars are not shown when only a single particle of that size was measured. Only 9 elements are labeled (with P and K seen as small slivers) whereas the others are too small to be seen in the figure.

After clustering, most clusters were assigned so that their average particle diversity (D_α) was close to one of the two modes present in Figure 3.8. This clear distinction between the two diversity modes is what the high and low diversity cluster names are referring to.

The bimodality seen here may represent the separation between fresh and more aged aerosol particles. The diversity values of the lower and upper mode of the combined data set were 2.4 and 3.6, respectively. Considering that the 3 elements C, N, and O dominate the mass fractions of most particles, it is fitting for one mode to be below and one mode to be above 3. Particles in the lower diversity group are mostly C, N, and O with very little presence of other

elements. The differing mass fraction between each of these elements causes the diversity to drop below 3.

This bimodality is absent in the T3 samples, having only the less diverse mode. The production of soot from transportation or fuel combustion is most likely the cause of this enhancement of lower diversity particles because of soot's relative elemental purity.

The two dimensional histograms between D_i and AED in Figure 3.8 serve to reinforce the idea that smaller particles tend to be less diverse. These smaller, less diverse particles are also less spread out whereas the more diverse particles show a wider spread in both diversity and size.

The increased spread seen in the aged aerosol group may be due to the variety of ways that aerosols can age and differences in distances traveled from the aerosols origin. Because the same variability isn't seen in the smaller, less diverse, fresh aerosol group we suspect these particles have sources close to where they were sampled. By sampling particles with nearby sources, the elemental composition and, by extension, particle diversity will be determined by the method of production and therefore be much less variable.
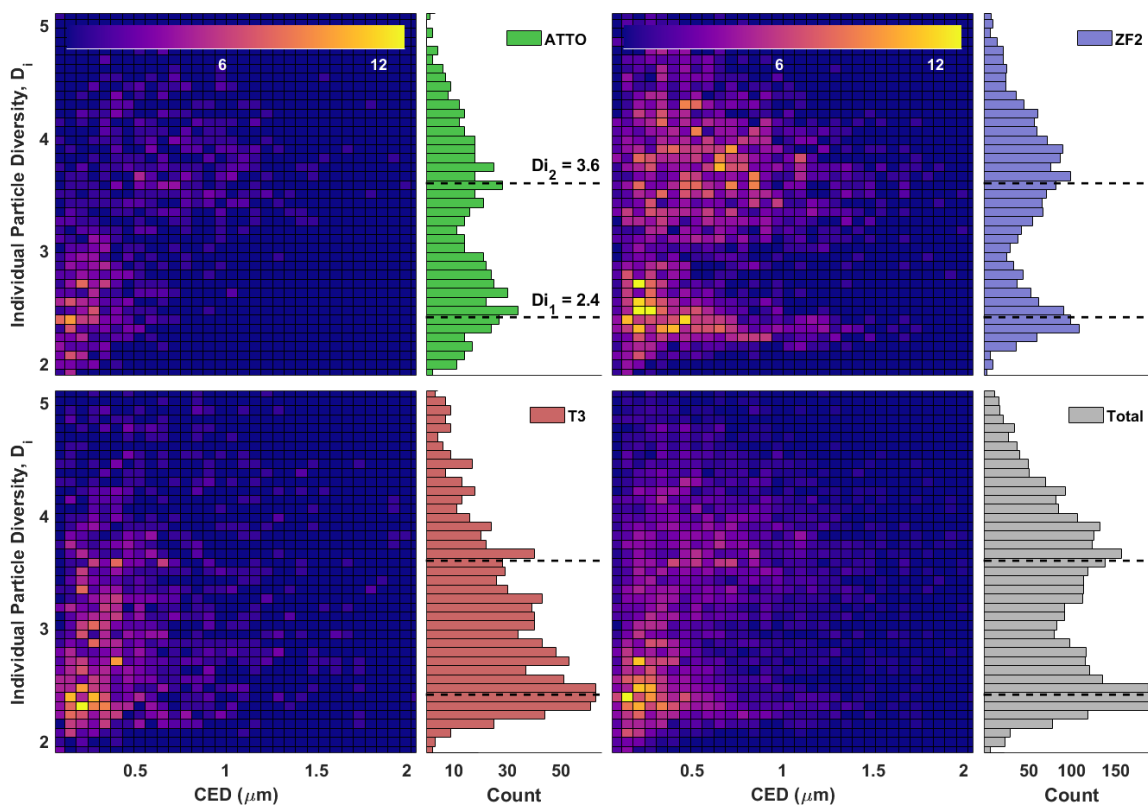
Figure 3.8 Histograms of individual particle diversity values for each sampling site. Histogram also shown for the combined data set of all three sites. The individual diversity value for the two modes are indicated with dashed lines and were calculated by fitting two Gaussian distributions to the total data set histogram.

3.4.5 Mixing state of particles at different sampling sites. Entropy metrics were used to quantify mixing state for each sample analyzed here. Figure 3.9 shows the mixing state index (χ) corresponding to particles in each sample. In this case, the variation in mixing state index is small, with all samples having a χ bounded between 0.8 and 0.9. This is a result of $D\alpha$ and $D\gamma$ consistently being around 3.4 and 3.9 respectively.
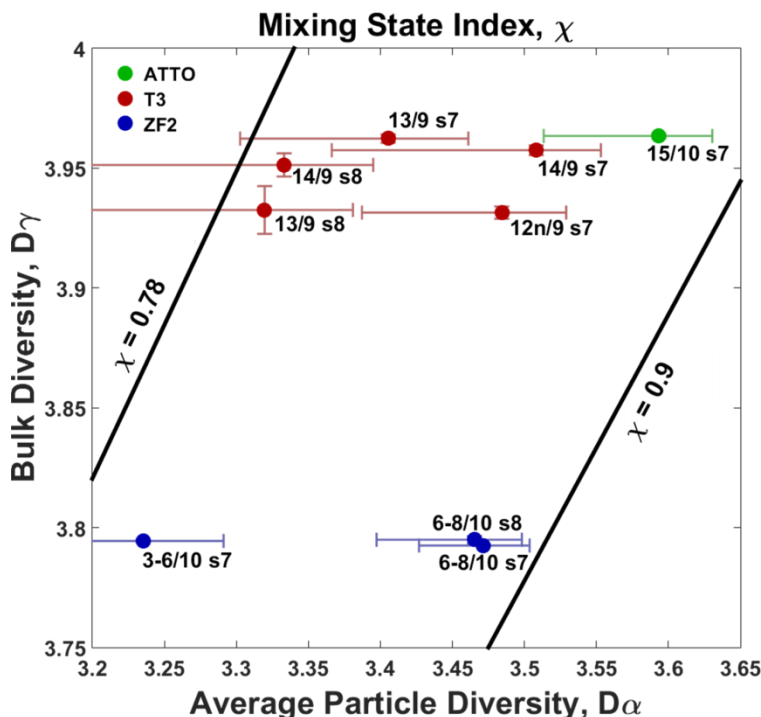
Figure 3.9 Mixing state index of each sample (color coded by site) with associated error bars. Error bars are adjusted to one-tenth of their size for readability. All average particle diversities are not significantly different. The site ZF2 bulk diversities are significantly different from the T3 and ATTO bulk diversities. Samples are labeled with day/month and stage number. The horizontal and vertical axes are essentially the numerator and denominator of the definition of χ (refer to Equation (14)).

In the previous study by O'Brien *et al.*,[124] similar sets of STXM and SEM/EDX data were collected for the CARES field campaign. In that study, the same diversity and mixing state parameterization was used except STXM data (elements C, N, and O) and SEM/EDX (elements Na, Mg, S, P, Cl, K, Fe, Zn, Al, Si, Mn, and Ca) data were analyzed independently. They found that mixing state index values for heavier elements usually ranged from $0.4 - 0.6$ with some values as high as 0.9. χ for C, N, and O generally ranged from 0.75 to 0.9. The mixing state indices retrieved from exclusively STXM data closely matches the values determined in this paper. This suggests that χ is almost entirely determined by C, N, and O due to these three elements dominating the mass of the individual particles and the sample as a whole.

A point of note is the small spread of D_γ values among a given sampling site. With D_γ representing bulk diversity, these values serve to compare the average elemental composition (for the 14 elements chosen) of all aerosols, condensed down into one number. For a given site, samples analyzed were taken during the same season of the same year with similar wind trajectories, sampling times and sampling duration. It is expected then, that there will be a consistency in how much of any given element is present in the aerosol population, based on how much of each element is produced. For D_γ to vary wildly from one day to another, or from one sampling period to another, would require an event or aerosol source producing substantially more of one element than usual.

The spread in D_α values among samples within a sampling site is much wider than that of D_γ. A large spread in D_α is expected when a singular diversity value is calculated from samples containing the variety of distinct particle types seen in Figure 3.3. This value is more susceptible to change from one sampling date to another compared to D_γ and depends on how much of each aerosol type is collected during a given sampling time.

The increase in the average particle diversity (D_α) with respect to increasing particle size is hinted at here, albeit in less certain terms. Focusing on samples collected where both stage 7 and 8 data were analyzed, average D_α values appear to be larger for stage 7 particles.

Samples collected at site T3 were expected to have a lower mixing state than either the ATTO or the ZF2 site. This hypothesis was borne from the quantity of fresh emissions in Manaus, specifically soot production from combustion which would serve to drive the mixing state downwards towards total external mixing. However, the end result of the error calculations in section 2.7 is that the values of χ for each point in Figure 3.8a become statistically unresolvable as can be seen from the large error bars. This is also not an issue that would be

solved with any reasonable amount of extra data collection but is instead mainly the consequence of the intrinsic spread in D_α.

3.5 Conclusions

Presented here is a quantitative combination between two complementary per-particle spectromicroscopy techniques, STXM/NEXAFS and SEM/EDX, on the exact same data set. STXM/NEXAFS data was collected at C, N, and O K-edges on a sub-particle level. This allowed not only the quantitative determination of C, N, and O absolute masses, but also carbon speciation and morphology. SEM/EDX allowed the approximate composition of the inorganic fraction to be determined and then quantified along with the STXM data. The combination of these two techniques enables almost all atmospherically relevant elements to be quantitatively probed on a per-particle basis. The potential issue with S detection discussed above could be mitigated entirely in future measurements by conducting STXM measurements at the S L-edge to obtain S mass fractions. This combined technique could be especially useful for identifying aerosol sources using elemental tracers or unique elemental compositions.

Using particle specific elemental composition, size, carbon speciation, and individual particle diversity (D_i), k-means clustering was used to separate particles into 12 clusters. The cluster average of these same parameters allowed for potential sources to be assigned. It was found that the stage 7 of the T3 site had a more varied population of particles (as defined by the effective cluster number) and contained more soot containing clusters than either the ATTO or ZF2 site. Clusters also exhibited size dependence, with a large portion of supermicron particles assigned to high diversity clusters which have been hypothesized to represent more aged particles. This approach could be used for even larger data sets, especially those located at long-standing measurement facilities. From this, diurnal, seasonal, or yearly changes in the aerosol

population could be monitored directly. Application of this combined technique would be especially fruitful near large pollution sources as these anthropogenic sources are difficult to model without the size-resolved composition presented here.[196] The clustering presented here offers an opportunity not only to classify particles but also to identify sources which can be invaluable in determining the effects of trade or environmental protection policies. The largest detriments to the utility of this composite technique are the long analysis times needed and the requirement for two separate instruments as well as time at a synchrotron light source.

Utilizing the composite data set to determine a quantitative mixing state index revealed that particles at site T3 were more externally mixed than at the other two sites. Error analysis, however, shows a fairly large uncertainty in the elemental mixing state for all samples, with statistical errors in χ ranging from 0.3 to 0.8. These error estimates do show that when calculating mixing state by using the 14 elements listed here, mixing state values are close together and show most samples to be highly (between 80 and 90%) internally mixed. Size dependent trends were also observed in individual particle diversity with larger particles being slightly more diverse (3.3 and 3.4 for sub and supermicron particles respectively). This size dependent trend in diversity was seen even more drastically within the fine mode with particles < 0.5 µm having an average D_i value of around 2.4 and particles > 0.5 µm having about a 3.6 diversity value, with a much larger spread of diversity values for larger particles. This difference may identify a separation between fresh and aged aerosols in terms of diversity. This result and the experimental method could be useful for climate models, allowing an experimental mixing state and size-resolved particle composition to be used rather than assumed to improve model performance.[197-199] Even though this type of individual particle microscopy study is time

consuming, regions which are important to global climate models (such as the Amazon) may benefit from the improved accuracy of an experimentally determined mixing state.

The quantitative mixing state index presented is a useful tool, but its utility can be readily expanded. Two of the advantages that this combined spectromicroscopy technique has are the ability to identify morphology both of the particles as a whole and of the constituents within the particle. Due to the general nature of the mixing state parameterization, the mixing state index and its interpretation is heavily dependent on what components were used. In this study 14 elements were used, however the omission or addition of just a few elements (especially abundant elements such as carbon) could drastically alter the value of χ. Because of this, specifics about which parameters were used and how relevant they are to the samples being studied must be examined before interpreting the value of χ. How well mixed individual elements are also may have limited usefulness to modelers or in general. With the exception of elemental carbon, mass fractions of specific elements (like nitrogen) are less chemically relevant than the molecules or ions they may be found in (sulfate vs. ammonium for example). Future work will build upon this composite technique to instead determine masses and a molecular mixing state for chemically and atmospherically relevant species such as nitrate, carbonate, sulfate, soot, and organics. Modification in this way could allow our current combined technique to determine an aerosol population's radiative forcing contribution due to both direct and indirect effects. Specific aspects about the indirect effect like hygroscopicity or the number of effective Cloud Condensation Nuclei (CCN) within a population of aerosols could also be gleaned from this method.[200] This type of modification would bolster the usefulness of this technique as well as the usefulness of χ for climate modelers.

Chapter 4: Optical and Spectral Properties of Airborne Soil Organic Particles and Tar Balls Found in the Southern Great Plains ARM Site During HI-SCALE

4.1 Synopsis

Spherical particles (SP) have been observed during April and May 2016 during the Hi-Scale field campaign in the Southern Great Plains (SGP) of the United States. They have been classified as airborne soil organic particles or tar balls based on smoke and precipitation data. These SPs are strongly correlated ($R^2 = 0.85$) with the absorption Ångström exponent (AAE). Extending this correlation to 100% SP yields an AAE of 2.6, similar to previous observations of BrC. NEXAFS spectra of ASOPs have smaller –COH peaks compared to tar balls as well as a smaller –COOH/C=C peak ratio. Samples with ASOPs are able to be separated from those with tar balls based on the –COOH/C=C and –COOH/COH peak ratios, with ASOPs having lower peak ratios. Near edge absorption X-ray fine structure (NEXAFS) spectra of particles generated from mud puddles show a previously observed ASOPs only when generated by bubbling, but not by nebulizing the mud puddle liquid. Nebulized samples carry with them dissolved soil inorganics that aren't present during bubbling or through the raindrop generation mechanism responsible for ASOPs. These results highlight the similarities between ASOPs and tar balls and show how they may be differentiated. These results also support the bubble bursting mechanism of generation during rainfall resulting in the ejecting of organics from the soil surface into the atmosphere.

4.2 Introduction

Regional and global chemical transport models are commonly used to better understand the significant impact that aerosols have on radiative forcing.[201] The efficacy of these models relies on estimates of the types, amounts, and influence of aerosols. Soot, one of the most well-

studied anthropogenic aerosols, has been named the second biggest radiative forcing factor behind carbon dioxide.[50] Soot is not the only light absorbing carbon aerosol of concern, however. While all organic carbon aerosols scatter visible light, some types of organic carbon absorbs light as well.[202] These absorbing organic carbon aerosols are referred to as brown carbon (BrC) aerosols as they tend to more efficiently absorb shorter wavelength light, giving them a brown appearance. Ongoing research on the role Brown Carbon (BrC) plays in global radiative forcing suggests it is underrepresented in models.[201-203]

BrC particles are not well defined, however.[50, 202] BrC refers to a broad category of particles which are comprised of many different light absorbing organic compounds (other than soot) originating from a variety of sources.[204] Sources of BrC include, but are not limited to, biomass burning particles[202, 205] and particles of biogenic origin such as fungi and soil humics.[43, 204] One example of BrC particles are tar balls which are found downwind of fires, especially smoldering ones.[42] These organic particles have been observed as having a spherical morphology resulting from their viscous or "glassy" composition, and have been noted to be resistant to changes due to electron beam exposure.[186] Recently, similar spherical BrC particles have been observed in rural Oklahoma, thought to be biogenic in origin, these newly discovered BrC particles have been coined airborne spherical organic particles (ASOPs).[43] This study observed the formation of submicron highly viscous particles following the impaction of rain droplets on the soil surface which serves to eject these ASOPs into the ambient air.[43] As falling water droplets make contact with the porous surface, air is trapped beneath the rapidly expanding droplet. These bubbles rise to the surface of the droplet bringing soil organics with them where a cavity forms and then ruptures producing film and jet droplets.[37] The numerous jet droplets results in what Joung and Buie call frenetic aerosol generation.[206-207]

A defining characteristic of BrC particles (like ASOPs) is their spectral dependence on absorption at visible wavelengths. One way of characterizing this spectral dependence, or the color of the particles, is to measure the absorption coefficient (σ_{ap}) as a function of wavelength, in order to calculate the absorption Ångström exponent (AAE). The AAE is essentially the slope of a log-log plot of absorption coefficient and wavelength, with higher values corresponding to enhanced absorption in shorter wavelengths compared to longer wavelengths. Because soot absorbs approximately equally across the entire visible spectrum (although there is a slight enhancement in absorption at short wavelengths) it has a fairly low AAE of 1. Compare this with reported AAE values for BrC of 2.5,[205] 3.5,[208] 6,[209] or as high as 9.[204] An AAE value of 2.5 or greater has been used previously to attribute absorption, at least in part, to BrC.[210] In addition to the AAE, absorption due to BrC has also been investigated through calculation of the complex refractive index.[211]

To better characterize these SPs, samples were taken from the atmospheric radiation measurement (ARM) facility in Lamont, Oklahoma located in the southern great plains (SGP) as part of the holistic interactions of shallow clouds, aerosols, and land ecosystems (HISCALE) field campaign. Two types of samples were collected: ambient aerosol microscopy samples and the collection of the surface layer of muddy puddles. The liquid suspension from the mud puddles was filtered and aerosolized before being impacted onto microscopy samples. The intent of these samples was to compare ambient AAE values with the morphology and composition of ASOPs collected on microscopy substrates. To this end, the microscopy samples were analyzed with both scanning electron microscopy (SEM) and scanning transmission X-ray microscopy coupled with near-edge X-ray absorption fine structure (STXM-NEXAFS) spectroscopy. SEM images were taken at a 75° angle to identify spherical particles (SP) suspected to be ASOPs.

Carbon STXM was also used to obtain speciated carbon maps and to identify potential ASOPs. When these potential ASOPs were found, a full NEXAFS spectra was taken to determine the composition of the organics present.

The present work seeks to understand the unique formation of these new particles observed following rain events and how they can be distinguished from biomass burning, SOA, or other anthropogenic sources.[212-213] The use of multiple experimental techniques (both bulk and single-particle) on the different types of data sets prepared here has allowed for an improved understanding of these underreported ASOPs. Using these techniques in tandem with longstanding atmospheric measurements will also help advance knowledge of how ASOPs fit into the broader class of BrC particles and how ASOPs affect aerosol climatology as a whole.

4.3 Experimental

4.3.1 Sample collection. Samples were collected at the ARM SGP field site located in north central Oklahoma [36° 36' 18.0" N, 97° 29' 6.0" W], at an altitude of 320 meters.[214] Sampling was performed before forecasted and after observed rain events, from April 26th through May 17th, during day and night periods separately. Within this time, 17 samples were collected between 8:00 to 21:00 local time. The sampling duration was roughly eight hours (unless interrupted by a major rain event) in intervals of 30 minutes on/30 minutes off. Similarly, 4 nighttime samples were collected between the hours of 18:00 and 6:00 local time in intervals of 1 hour on/30 minutes off. Rain events interrupted two sampling days, May 8th and May 16th, in which no sampling took place. The primary objective was to observe particle types during sunny days following major rain events, where a threshold precipitation rate of 10 mm/hr was used to define a rain event.

Particles were collected by impaction using a Micro-Orifice Uniform Deposit Impactor (MOUDI, MSP 100) attached to a rotating motor that rotates the stages to facilitate more uniform particle deposition. The impactor was connected to a ¾ max horsepower (0.56kW) vacuum pump (General Electric Motors & Industrial Systems, 10 PSI rating). With a 30L/min sampling flow rate, the micro-orifice nozzles reduce jet velocity, pressure drop, particle bounce and re-entrainment. This MOUDI was connected to a mesh covered sampling inlet which was tilted downward, avoiding unwanted collection of descending debris, insects, and other sources of contamination, and was positioned ~6 meters above the ground.

Samples were selected from two stages with the following particle size cutoff ranges: stage 7 (0.32 to 0.56 μm) and stage 8 (0.18 to 0.32 μm) because they span the average size range of ASOPs[43]. Substrates of both Si_3N_4 film supported by a silicon wafer (0.5 X 0.5 mm^2 Si_3N_4 window, 100 nm membrane thickness, 5 X 5 mm^2 Si frame; Silson, Inc.), and filmed copper grids (Carbon type B film, Copper 400 mesh grids; Ted Pella, Inc.) were used as impaction substrates.

In addition to impaction samples of ambient aerosols, soil organic matter (SOM) brine was collected in 50-200 mL aliquots via syringes from mud puddles surrounding the SGP field site. This was performed in attempt to draw a connection between brine samples, the hypothesized source of ASOPs, and ambient ASOPs. Three samples (S1, S2, S3), were collected from SOM brine on May 17th 2016. The brine samples were nebulized using a Collison nebulizer (3 jet MRE, CH Technologies USA) and collected on stage 8 of a 10-stage impactor (110-R, MSP, Inc.) to produce 300-500 nm diameter particles, where ASOPs comprised up to 80% of the particles by number. In addition, a portion of sample S1 was used to generate

particles by bubbling N_2 gas through the liquid using a fritted glass bubbler in an attempt to better recreate the hypothesized mechanism.

    4.3.2 STXM Measurements and Image Processing. The STXM instrument (beamline 5.3.2.2 ALS, Berkeley, CA, USA) used in this work is located in the Advanced Light Source (ALS) at the Lawrence Berkley National Laboratory. [91] The ALS houses a synchrotron, which is capable of accelerating electrons to 299,792,447 meters/sec (99.999996% the speed of light). A bending magnet is used to produce and direct photons of light towards an X-ray monochromator, where a narrow band of photon energies are selected. A Fresnel zone plate then focuses the monochromatic soft X-ray beam down to a spot size ranging from 20 to 40 nm in diameter. The sample is positioned at the focal point, and raster scanned, thereby generating an image. Any incident light that is not absorbed by the sample is transmitted to a detector, comprised of a Lucite light pipe thinly coated by phosphor and coupled to a photodiode. After a region of sufficient particle concentration is found, an image is captured at a selected energy before the process is repeated at a new photon energy. STXM analysis of ARM SGP samples include spectral images (several images at different energies; also known as a "stack"), roughly 100 images taken at unevenly spaced energies to capture wide-ranging chemical composition, and "maps", where only a few images are taken at key energies. In this case, 8 energies were selected around elemental absorption K-edges, 4 energies corresponding to C (278.0, 285.4, 288.6, and 320.0 eV), 2 to N (398.0 and 430.0 eV), and 2 to O (525.0 and 550.0 eV). These energies are used to identify and characterize the chemical composition of each aerosol particle on a pixel-by-pixel basis. The two extra C energies at 285.4 and 288.6 eV are used for the identification of soot or elemental carbon (EC). The absorption peak at 285.4 eV occurs due to the excitation of the C 1s $\rightarrow \pi^*_{C=C}$ transition (* distinguishing the excited state) which is indicative of sp^2 hybridized

carbon-carbon bonds (C=C). This excitation of sp^2 hybridized carbon is prominent for soot and elemental carbon (EC)[203]. To identify soot or EC, the intensity of the sp^2 peak (relative to the pre-edge at 278 eV) must equal or exceed 35% of that of highly ordered pyrolytic graphite (HOPG).[100] The transition at 288.6 eV is representative of the C 1s $\rightarrow \pi^*_{R(C^*=O)OH}$ transition for carboxylic acid groups (COOH), and is nearly always present in atmospheric organic carbon. These photon energies aid in accurately differentiating individual particles based on the molecular speciation of carbon, making this method convenient for analysis of the spring 2016 sampling period.[100] Spatial displacement between images within a stack does occur and can be corrected for by utilizing the image registration algorithm developed by Guizar-Sicarios'.[97, 114]

4.3.3 SEM measurements. The microscopy samples were taken separately to the Environmental Molecular Sciences Laboratories (EMSL) at Pacific Northwest National Laboratory (PNNL) where they were imaged using a computer-controlled scanning electron microscope (FEI, Quanta 3D FEG, Hillsboro, AL, USA). SEM images were initially taken orthogonally to the substrate until a particle-laden region on the substrate was identified. The substrate mount was then tilted by 75° in order to identify any spherical particles. From this tilted view, particles which had an aspect ratio (height divided by width) greater than 0.8 were identified as Spherical Particles (SP). The SP% for each sample was calculated by visually identifying and counting SP and non-SP particles after approximately 400 total particles had been examined. This was done for both ambient and lab-generated samples.

4.3.4 PSAP Measurements. The Particle Soot Absorption Photometer (3-λ PSAP) instrument measures light transmission through aerosol filter samples at three wavelengths: red (660 nm), green (522 nm) and blue (470 nm).[215] PSAP measurements were taken at the SGP ARM facility, and are available for use from the ARM data archive.[216] Equation 1 shows how

absorption coefficients σ_{ap} are calculated from raw PSAP data using spot size (A), sample volume (V), and average filter transmittances for incident (I_O) and transmitted (I) light through particle laden filter.

$$\sigma_{ap} = \frac{A}{V} \ln\left[\frac{I_o}{I}\right] \tag{4.1}$$

Implementing appropriate corrections specified in Bond *et al.*, 1999, helps minimize noise present in the PSAP data, which is a result of inherent unit-to-unit variability in field instrumentation. Additionally, these corrections mitigate systematic error from filter loading. The absorption reported by the PSAP instrument (σ_{PSAP}) includes an inherent calibration for a given measurement period which monitors the change in transmission by using the previous sample as a blank.

$$\sigma_{PSAP} = \frac{\sigma_{ap}}{2(0.5398\tau + 0.355)} \tag{4.2}$$

The raw absorption coefficient of a sample (σ_{ap}) at a given time is normalized by filter transmission (τ), which is reset after the installation of a new filter ($\tau = 1$ for an unloaded filter). Together, these equations (4.1) and (4.2) smoothen out the absorption time series. These absorbance time series were initially collected with 1-minute time resolution and were subsequently averaged over 30-minute windows. Low absorbance values were also filtered that would normally interfere with noise and calibration drift.[217] The CO_2 scattering coefficient was experimentally determined by Anderson *et al.* (1998) using the same model air/He calibrated nephelometer utilized in this study. These noise predictions were validated using measured refractive indices and depolarization factors, discussed by Anderson *et al.* (1996).[218] Additionally, equations (1) and (2) can also remove artifacts such as the underestimation of σ_{ap} due to noise peaks or overestimation of σ_{ap} due to abnormally high red absorbance or abnormally

low blue absorbance. Finally, gaps in transmission (τ) that would occur between filter changes can be removed by this correction as well.

After obtaining the corrected absorption coefficients, they are then used to calculate the AAE. Backman *et al.* (2014), documented the following equation relating Ångström Exponent (AE, which relates light extinction to wavelength), to AE which is specific to light absorption:[219]

$$\ln\left[\sigma_E(\lambda)\right] = -AE\ln[\lambda] + C \tag{4.3}$$

here, σ_E refers to the extinction coefficient at wavelength λ. While the AE represents the spectral dependence of all light interactions, the AAE is specific to absorption and is obtained by substituting σ_{ap} for σ_E.[219] By taking Equation 4.3 at a given wavelength and subtracting Equation 1 at another wavelength, the constant C can be removed, resulting in a more practical equation:

$$AAE = \frac{-\ln\left[\frac{\sigma_{ap}(\lambda_1)}{\sigma_{ap}(\lambda_2)}\right]}{\ln\left[\frac{\lambda_1}{\lambda_2}\right]} \tag{4.4}$$

With this equation, PSAP data can be used to calculate the AAE of ambient particles (possibly containing BrCs).

4.4. Results

4.4.1 Optical properties of spherical particles (SP). SP are hypothesized to be a form of BrC that show an increased absorption for shorter wavelengths of visible light compared to longer wavelengths. During periods where SP are prevalent, bulk optical properties should start to resemble those of BrC. To investigate the presence of BrC using this wavelength dependence, PSAP data was used to calculate the AAE and is shown in Figure 4.1 alongside the corrected absorption coefficients. CO and particle number concentrations are also shown in Figure 4.1 to provide further information on the air mass. Figure 4.1 shows how both red and blue absorption coefficients and AAE change over the course of this IOP. Note that during many of the rain

events (denoted by vertical red stripes) the absorption coefficients decreases rapidly due to a decrease in aerosol concentration. Rain events were defined as any period of unbroken rain (disregarding breaks less than 30 minutes long) where rainfall exceeded 10 mm/hr. Typically, this decrease in aerosol concentration can be attributed to a "wash out", also known as precipitation scavenging, which is the suspension and transport of ambient aerosols to the earth's surface by rain droplets.[220] The vertical gray bars show sampling dates from which substrates were imaged with STXM.
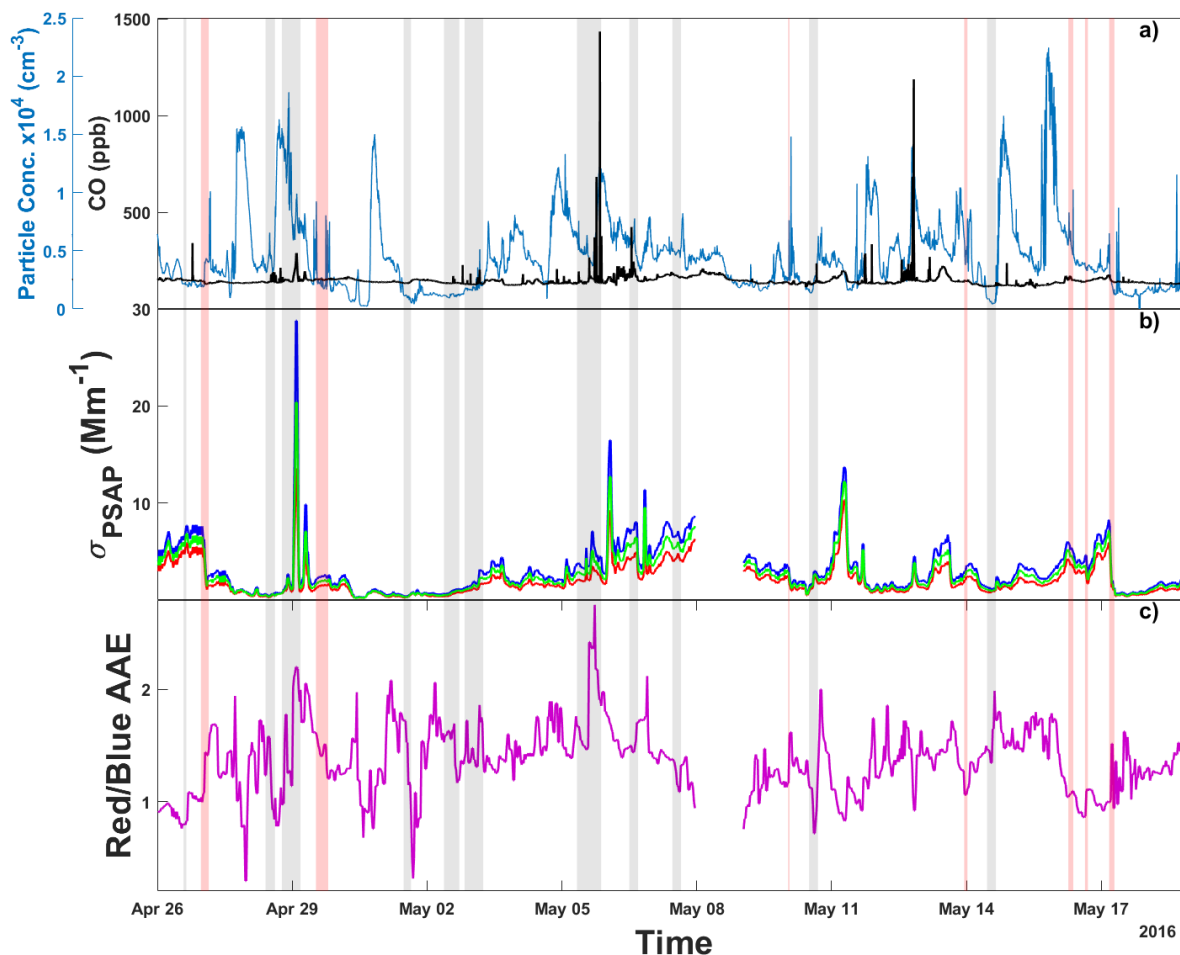
Figure 4.1 Time series CO, particle concentration, absorption, and AAE. Labeled plots are for a) CO and ambient particle concentration, b) red (660 nm), green (522 nm), and blue (470 nm) absorption coefficients, and c) absorption Ångström exponent (AAE) calculated from red and blue absorption coefficients. Grey vertical bars represent aerosol sampling periods and red vertical bars represent periods of rainfall. PSAP data for May 8th is not available due to instrument error.

Both the absorption coefficient and AAE time series data were collected with minute time resolution; the data shown below has been averaged over 30-minute time windows and then smoothed to emphasize data trends over short-term fluctuations. The AAE sometimes shows an increase after rain events, like on April 27th or May 14th, but it is not consistent. From this, a few samples stand out: May 14th, May 5th and the night of April 28th as these samples had an elevated AAE. An AAE value greater than 2.5 has been used in previous work to signify BrC, which may suggest the presence of BrC in the May 5th and April 28th samples at least and warrants further analysis.[210] While the May 14th sample doesn't have a particularly high AAE compared to the entire time series, it is unique in that it shows an AAE elevation shortly following a rain event. One thing to note is that the lower the σ_{ap} drops, due to rain or otherwise, the more pronounced the effect PSAP noise has on the calculated AAE. In addition to having high AAE values, both the May 5th and April 28th sample have elevated particle and CO concentrations suggesting the influence of biomass burning for these samples.

4.4.2 Spherical Particle (SP) Classification. Bulk optical properties, like an elevated AAE, can suggest the presence of spherical BrC particles, therefore these measurements were used to select samples for a detailed analysis of particle morphology using microscopy. To this end, tilted SEM images were taken and a wide range of SP% values were observed, from less than 5% to near 70%. Figure 4.2 shows representative microscopy and spectromicroscopy images for three days where the SP% was high. The top row shows the tilted SEM images used to identify SPs. Pink arrows point to a few identified SPs to highlight how much they stick out above the substrate compared to the others. Also of note in the SEM images is the presence of what looks like fractal soot in the April 28th and May 5th samples.

The middle and bottom row of images shown in Figure 4.2 are STXM images and they are both of the same field of view. The middle row shows carbon speciation maps where each pixel is assigned as either inorganic dominant, organic dominant, or as a region with high C=C bonding in accordance with Moffet, *et al.* 2010.[100] The bottom row shows the thickness of each of the particles (as calculated using previously published thickness equations[124, 221]) normalized by the individual area equivalent diameter. Values close to 0 represent flat particles while values closer to 1 represent taller, possibly spherical particles. As was suggested in the SEM images, soot is present in both the April 28th and May 5th sample, while the May 14th sample has only organic and inorganic particles. In the April 28th and May 5th sample, it is these soot particles which are the tallest and look the most spherical. In contrast, the May 14th sample has a possibly spherical particle which is only comprised of organic dominant pixels.
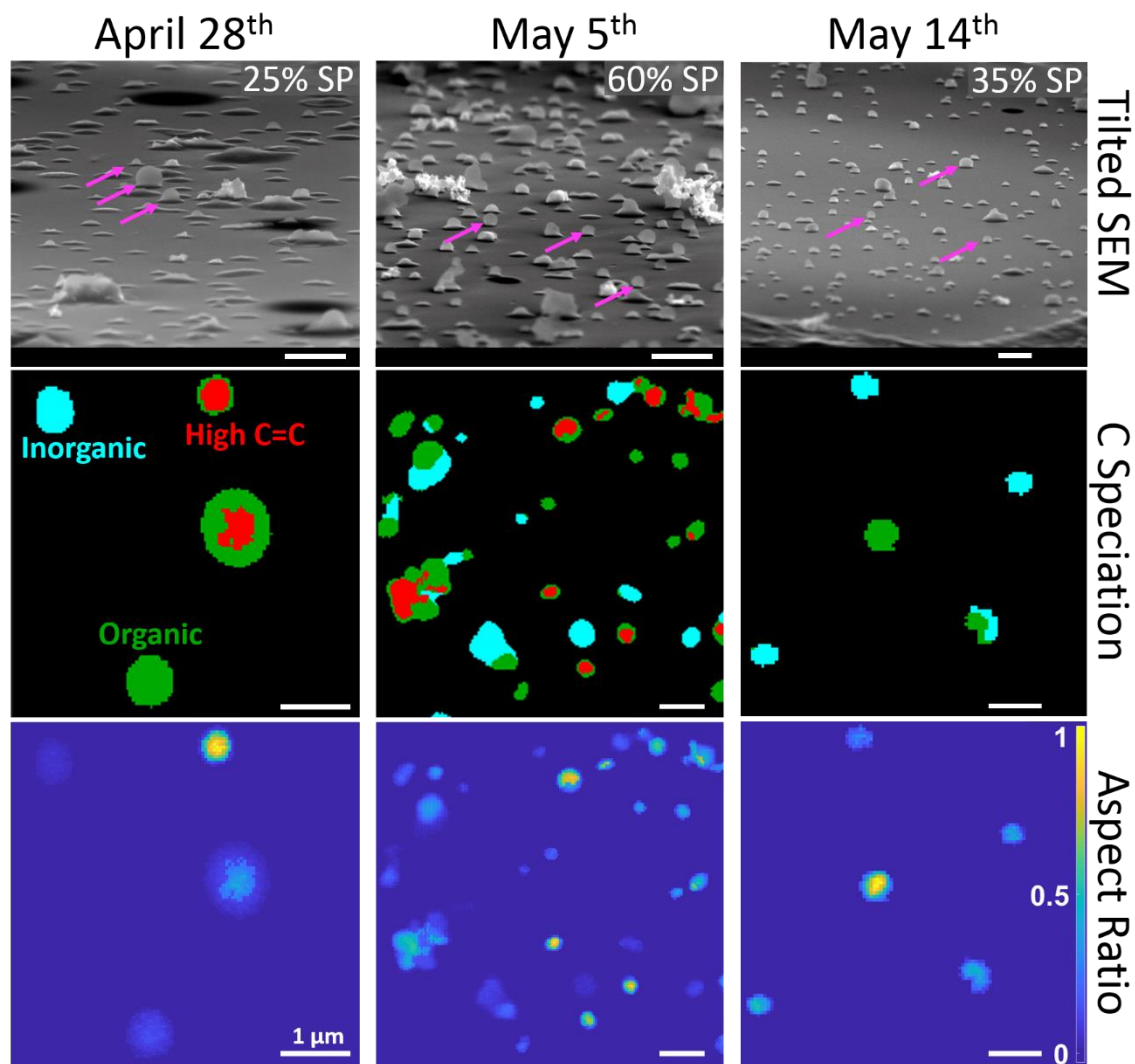
Figure 4.2 SEM and STXM micrographs of 3 sampling dates. (top) Tilted (75°) SEM images show differences in SP concentration between three samples with elevated SP%. Each of these samples were collected on a MOUDI stage 8, which selected for particles in the 150-360 nm size range. Pink arrows point to a few example SPs. (middle) Carbon speciation maps with red representing regions with enhanced C=C bonding, green representing organics, and teal representing inorganics. (bottom) Aspect ratio images calculated from dividing thickness by the area equivalent diameter of each particle.

Sample collection information from the 7 samples where the SP% was calculated is presented in Table 4.1 below. The highest SP% was observed with the samples taken on May 5th. The prevalence of these particles can be seen in Figure 4.2 in the top row. An elevated SP% was also found for the April 28th night sample taken at 18:30 as well as for the May 14th sample. While the April 28th and May 5th sample show elevated SP% for both stage 7 and 8 substrates,

the May 14th sample is unique in that a higher SP% was only found for the smaller stage. In addition, the April 28th and the May 5th sample both have elevated particle concentrations and CO levels, suggesting more polluted conditions possibly due to biomass burning. In contrast, the May 14th sample shows the lowest particle concentration and CO levels. Also of note is that the April 28th and May 5th samples were both taken long after the last rain, with May 5th being taken multiple days afterwards whereas the May 14th sample was taken 10 hours after the last rain.

Samples from this data set has been analyzed previously by Veghte, *et al*. in 2017.[211] There, the complex refractive index from 200 to 1200 nm was calculated for the April 28th sample using electron energy loss spectroscopy (EELS). The imaginary part (k) of the refractive index is related to light absorption and can be related to the absorption coefficient using $\sigma_{ap} = 4\pi k/\lambda$.[222] Absorption coefficients over the $200 - 1200$ nm wavelength range were calculated from the published imaginary refractive index plot. From this plot, the AAE was calculated using the σ_{ap} values for 660 and 470 nm and a value of 1.41. This is close to the value calculated in the present work (1.42, Table 4.1) for the April 28th sample (a difference of only 0.01) showing that the two methods agree, at least for the one sample.

Table 4.1 Ambient samples collected during IOP1

Start Date (CDT)[1]	Stage	Duration (hr)	SP %	AAE (Red/Blue)[2]	Hours Since Last Rain[3]	Particle Conc. (cm^{-3})[4]	CO (ppb)[5]
26 Apr 14:00	7	1.5	<5%	0.808	>72	2100	150
28 Apr 9:45	7	5	3%	1.20	30	4100	140
28 Apr 18:30	7	10	23%	1.42	39	10300	160
-	8	-	25%	-	-	-	-
1 May 11:30	7	4	12%	1.23	45	1000	130
-	8	-	15%	-	-	-	-
2 May 20:00	7	10	13%	1.15	80	1900	130
5 May 8:00	7	13	70%	2.01	140	6000	170
-	8	-	60%	-	-	-	-
14 May 11:00	7	5	10%	1.29	10	650	120
-	8	-	35%	-	-	-	-

[1]Central Daylight Time (UTC -5) [2]Particle Soot Absorption Photometer (PSAP) [3]Video Disdrometer [4]Condensation Particle Counter (CPC) [5]ARM/Aerosol Observatory System (AOS)

From Table 4.1 a correlation plot was made between AAE and SP% and a strong correlation was found ($R^2 = 0.85$) as seen in Figure 4.3 below. Extrapolating this linear correlation to 100% SP's yields an expected AAE of 2.6, comparable to previously recorded AAE values for BrC. This not only suggests that the SP's found here are BrC, but that they are numerous enough to warrant consideration by models due to their measureable effect on bulk aerosol-radiation interactions. This also shows that, on certain days, BrC particles can occupy significant fractions of the aerosol fine mode.
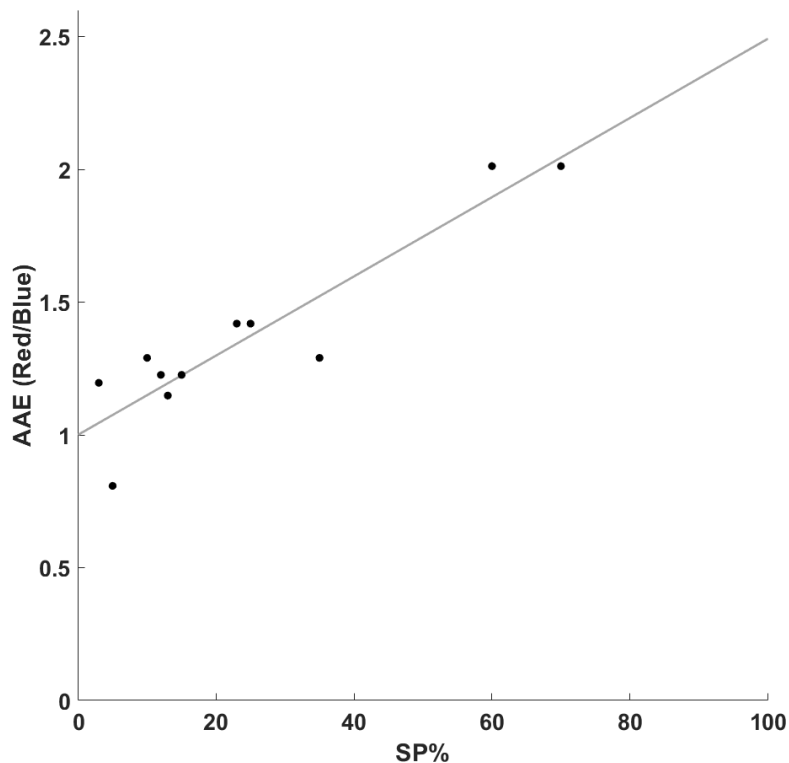
Figure 4.3 Linear correlation between SP percent and AAE. A linear fit is shown, having an R^2 value of 85%. Extrapolated to 100% SP yields an expected AAE of about 2.5. Brown carbon has been previously associated with AAE values greater than 2.5[210]

So far, the above analysis applies to the more general class of SP, which can include ASOPs and tar balls. Additional considerations are necessary, however, before any conclusions are tied to ASOPs exclusively. The two highest SP% samples, with the highest AAE values, were seen in samples collected more than 39 hours after a rain event. Because ASOPs have been shown to be collected after rain falls upon the soil surface, the SP's found in the April 28th and May 5th samples may not be ASOPs.

To investigate the nature and source of the SPs and determine which can be confidently classified as ASOPs, smoke,[223] fire,[223] and precipitation data,[224] were used along with hybrid single particle Lagrangian integrated trajectory model (HYSPLIT) back trajectories were calculated.[225-226] This data for the events when the three samples had elevated SP% are shown in Figure 4.4 below: Apr 28th, May 5th, and May 14th.
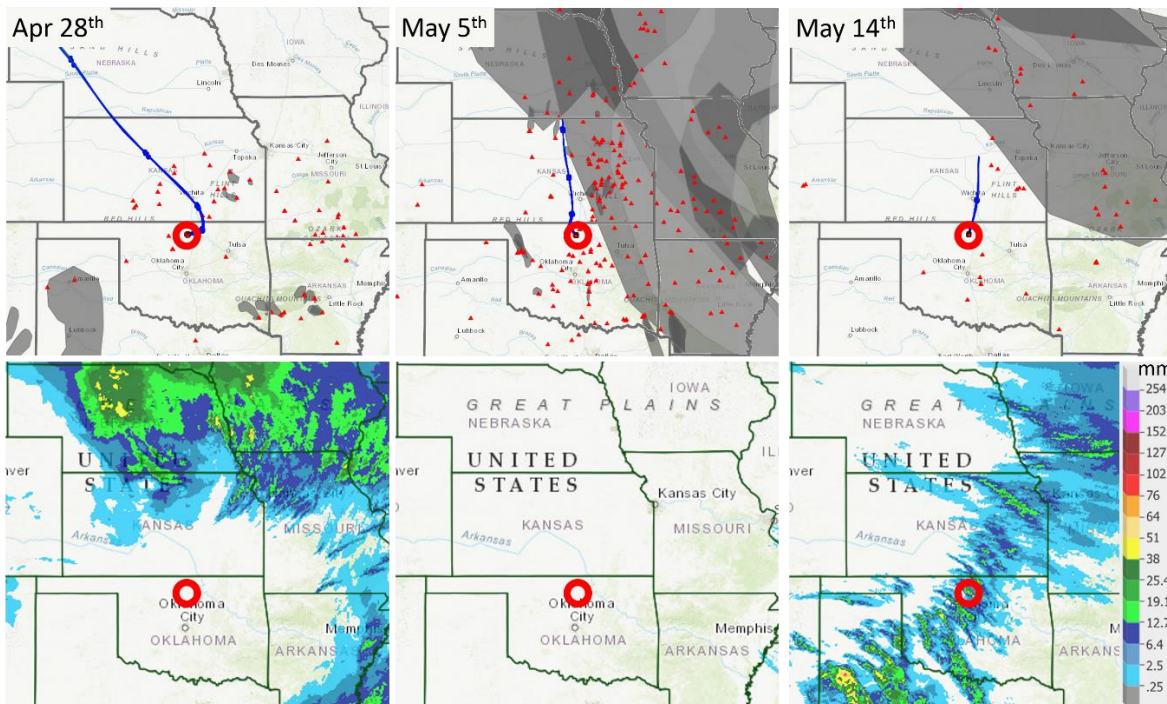
Figure 4.4 Smoke, fire, and precipitation data and HYSPLIT back trajectories for three sample dates. The red circle represents the sampling site while the small red triangles represent fires. The gray overlay seen in the top row represents detected smoke particles. The bottom row shows the 24-hour average precipitation amount over the sampling date. The top row maps were obtained using the AirNow-Tech navigator.[227] HYSPLIT trajectories for April 28th and May 5th are for 24 hours. The May 14th back trajectory was truncated at 10 hours due to a rain event with significant precipitation scavenging. Precipitation maps were made using the NWS AHPS.[224]

April 28th had a moderate SP% along with the second highest AAE over the sampling periods studied here. This sample was also taken about 39 hours after the last rain event which makes ASOPs less likely to be found. Figure 4.4 shows that air mass trajectories passed over a few burning fires. Smoke was present in some of the fires surrounding the sampling site but air mass trajectories did not pass through these regions. Precipitation data shows rainfall in some of the surrounding states but none at the sampling site. This is in tandem with an elevated particle concentration and slightly enhanced CO concentration, both of which are related to biomass burning emissions.[24]

May 5th has the highest SP% and the highest average AAE but it too had been days (140 hours) since the last rain event making ASOPs unlikely. There were many fires surrounding the

sampling site compared to the other sampling periods and the back trajectories show air masses passing directly over some of these fires and their associated smoke plumes. Precipitation data shows that no rainfall was observed anywhere near the sampling site. Figure 4.1 also shows that this sampling date coincided with a slight particle concentration enhancement and the highest CO concentrations observed over this period of the field campaign. Because tar balls are found within smoke plumes, the high SP% seen in the April 28th and May 5th samples may be primarily (or exclusively) due to tar balls.[186] The presence of combustion byproducts like tar balls and soot is supported by the three STXM carbon speciation maps shown in Figure 4.2, where particles with elevated C=C bonding are often attributed to soot.

The last sample date shown (May 14th) has regions of smoke away from the sampling site with back trajectories heading from just outside the smoke filled region. However, because a rain event was recorded 10 hours prior to sampling where significant precipitation scavenging was observed (see the particle concentration decrease in Figure 4.1), no influence from biomass burning was present during this sample. The precipitation map shows that precipitation was observed over the sampling site as well as many of the surrounding areas. Because the microscopy samples were taken so soon after it had rained, the 35% SP observed here is likely to be from ASOPs. With the SP's observed in the microscopy images being around 0.6 μm in diameter, it is expected that they would be aloft and present for the sampling period after 10 hours.

The influence of smoke shown in Figure 4.4 may account for the enhancement of SP% without rainfall in the April 28th and May 5th samples, likely due to tar balls. The carbon STXM spectrum of tar balls have been recorded previously and is shown in Figure 4.5 below.[228] Figure 4.5 also compares the STXM spectra for both ambient particles collected during this study and

lab generated ASOPs. On the right of Figure 4.5, three spectra are shown for the April 28th and May 5th samples along with one spectrum for May 14th. Even though May 5th and April 28th had the highest AAE and SP%, the many hours since the last rain along with the presence of smoke suggest they might be tar balls. Three clear peaks are common for these spectra: the C=C peak at 285.3 eV, the COH (or ketone) peak at 286.7 eV, and the -COOH peak at 288.6 eV, all of which are present in the previously reported tar balls spectrum. Both May 5th spectra also show a small bump around 289.5 eV which is present (and more prominent) in the tar balls spectrum, a peak which is associated with alkyl carbon bonded to oxygen, often alcohols. This similarity reinforces the idea that May 5th contains a large amount (70%) of SP attributable to tar balls.

Upon comparison with the April 28th and May 5th samples, the May 14th sample (taken 10 hours after raining) shows a slightly enhanced C=C peak and an almost absent COH peak. These same features can be seen in the previously reported average ASOP spectrum by Wang, et al and have been remarked upon by Veghte, *et al* as well.[43, 211] One reason for the difference in COH peak intensity may be due to the presence of levoglucosan or levoglucosan-like molecules (which contains 3 –OH groups) in the samples affected by smoke plumes, a common product of biomass burning from the pyrolysis of carbohydrates.[229] Another differentiating factor looks to be the ratio of intensities between the –COOH peak at 288.6 eV and the C=C peak at 285.3 eV. In the tar balls spectrum, the –COOH peak is much higher than the C=C peak compared to the Wang, et al average ASOP spectrum and this difference is borne out in the spectra collected for the current study as well. Also shown is a spectrum from organics not associated with SPs. This spectrum is characterized by small C=C and COH absorptions with an intense –COOH peak. The presence of a large carboxylic acid peak observed with the flat, non-SP aerosols may be due to water soluble organics. The particles carrying these organics may be wet particles which carry

the soluble organics with them to the sampling plates and then experience spreading upon impaction. The particles then dry from storage or in the vacuum of the STXM chamber, leaving only the organic behind.
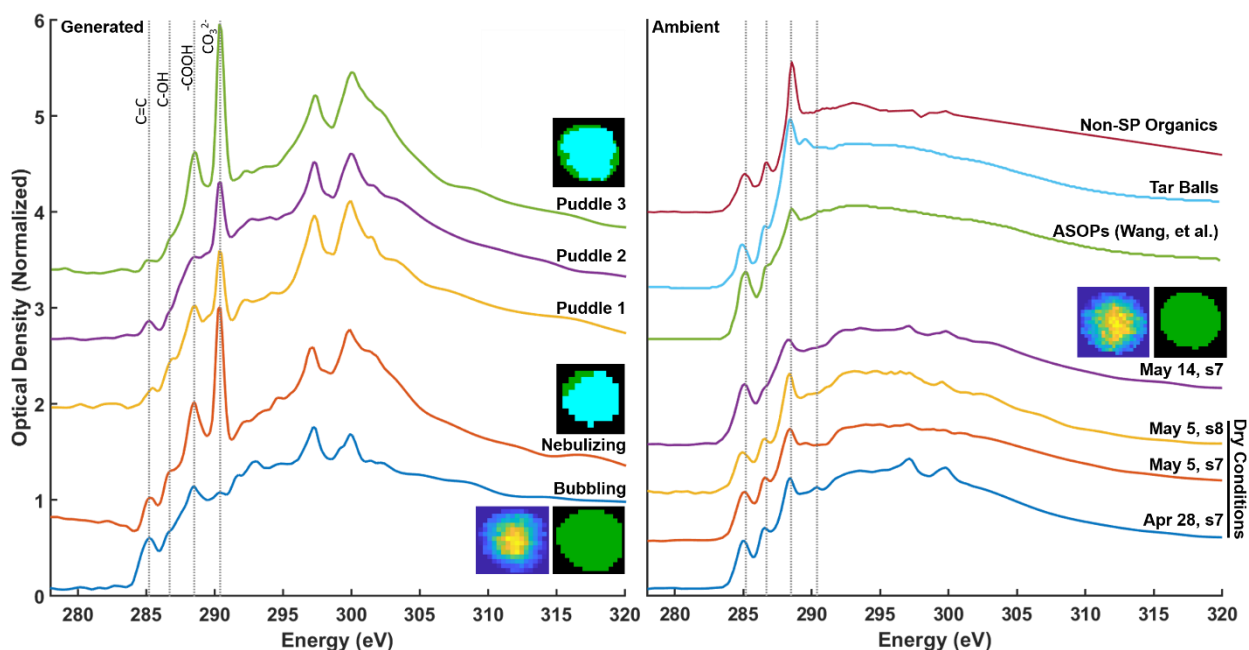
Figure 4.5 Comparison between laboratory generated ASOPs (left) and ambient ASOPs (right). Carbon speciation maps are shown for representative particles with green representing organic dominant regions and teal representing inorganic dominant regions. Aspect ratio images, like the ones shown in Figure 2 are shown as well. Only one image is shown for the ambient samples as they all look similar.

The left-hand plot of Figure 4.5 shows laboratory generated ASOPs from the SOM brine. The top three spectra from the three puddle samples all show a fairly strong carbonate signal at around 290.1 eV along with two broad potassium peaks (L_2 and L_3) at about 298 eV. In addition, the carbon speciation maps showed large regions which were inorganic dominant which didn't fit with the mainly organic particles seen previously. However, because these samples were aqueous to begin with, carbonate salts from the soil must have been present upon nebulization. In an effort to better recreate the bubble bursting mechanism of generating ASOPs, dry N_2 gas was bubbled through one of the solutions. Particles collected from the bubbling

sample showed almost a complete reduction of the carbonate peak and a small reduction in the potassium peaks, plus the carbon speciation map showed an entirely organic dominant particle. From this, generating aerosols by bubbling seems to better imitate the hypothesized ASOP generation mechanism. Comparing the bubbling sample spectrum with the ambient spectra on the right, this matches the post-rain spectrum from May 14th and the previous ASOP spectrum. This includes the diminished –COOH/C=C peak ratio and the relative absence of a COH peak.

For better comparison, two sets of peak ratios were calculated. The first between the –COOH and C=C absorptions and another between the –COOH and COH peaks. The peak ratios were then plotted in Figure 4.6 below for all of the ambient samples and the two literature spectra. The three puddle spectra and the nebulized puddle spectra were excluded for being less comparable with the ambient samples than the bubbling spectra. As noted above, the tar ball spectrum has a high –COOH/C=C peak ratio along with a high –COOH/COH peak ratio. The separation between these two ratios is also the largest for the tar ball spectrum. While the April 28th and May 5th peak ratios are not quite as high, they all bear a strong resemblance to the tar ball spectrum. Perhaps alone the similarity wouldn't be enough to define these ambient samples as tar balls; however, coupled with the other data presented here the peak ratios support the SPs seen in the Apr 28th and May 5th samples being tar balls. The May 14th sample peak ratios are much different and are more comparable to the ASOP literature peak ratios. The –COOH/C=C ratio is much lower in both cases and the –COOH/COH ratio is almost the same value. From the lab generated aerosols, the bubbling sample peak ratios are also quite similar to the ASOP literature peak ratios, offering further evidence that bubbling reproduces the natural ASOP generation mechanism more faithfully than the other methods. Another noteworthy observation is the difference between the April 28th or May 5th peak ratios and the May 14th peak ratios.

Although each of these samples showed the presence of SPs and each sample's AAE suggested that these SPs were BrC, there is a stark contrast between the smoke influenced samples (Apr 28th and May 5th) and the rainfall influence samples (May 14th).
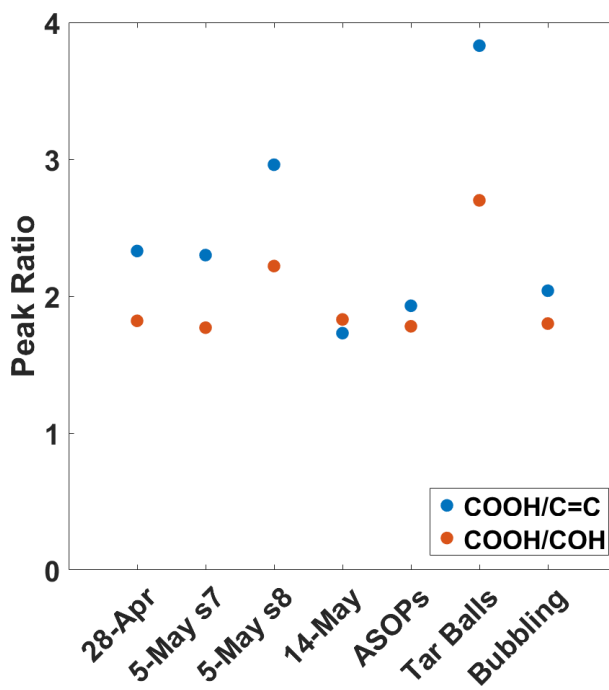
Figure 4.6 Plot of peak ratios for COOH/C=C and COOH/COH. (blue dots) carboxylic acid peak at 288.6 eV divided by carbon double bond peak at 285.3 eV (red dots) carboxylic acid peak divided by alcohol peak at 286.7 eV

4.5 Conclusion

BrC particles like tar balls or ASOPs and their place in the global aerosol budget are not yet fully understood. Here, BrC has been shown to measurably affect bulk optical properties such as the AAE and on multiple days SPs were observed to comprise a significant fraction of the fine mode aerosols.

Tilted SEM was used to identify SP on a number of samples taken during this IOP, and the approximate percentage of SP present for each sample was manually determined by their aspect ratio. This SP% showed a strong correlation with the average AAE over the sampling

periods, with an R^2 of 0.85. When extrapolated to 100% SP an AAE of 2.6 was calculated, close

to previous calculations of pure BrC AAE values which supports the idea that BrC can be

identified using aspect ratio and chemical composition together. These samples were further

classified into samples with tar balls and samples with ASOPs by comparing smoke and

precipitation data during their collection periods.

Further analysis into the differences between supposed ASOP and tar ball laden samples

was performed with STXM/NEXAFS. Samples unaffected by recent rain, but that were

collected while smoke plumes were present showed a higher –COOH/C=C peak ratio and

showed an elevated –COH peak. The elevated –COH peak may be due to the presence of sugars

such as levoglucosan or other less oxidized molecules. The sample from May 14th was collected

a short 10 hours after a recent rain event and had less influence from smoke plumes. This

sample showed a much more subdued –COH peak and a smaller –COOH/C=C peak ratio.

Comparing the ambient spectra collected here with previously collected spectra supported the

presence of tar balls in the smoke-affected samples and also supported the presence of ASOPs in

the sample taken after a recent rain event. Peak ratios between –COOH and C=C and between –

COOH and COH were calculated, emphasizing the difference between tar balls and ASOPs and

between the smoke-affected samples and the samples with recent rainfall.

STXM/NEXAFS was also performed on particles generated from liquid taken from mud

puddles on the ground at the SGP sampling site. A strong signal of carbonate was observed in

the NEXAFS spectrum if particles were simply nebulized but when dry N_2 was bubbled through

the liquid (imitating the hypothesized ASOP generation mechanism) the carbonate peak was

greatly diminished. In addition, the NEXAFS spectra of particles generated by bubbling

matched the previously collected ASOP spectra both in the –COOH/C=C peak ratio and in the diminutive –COH peak, giving further credence to the rainfall generation mechanism.

SPs are a subclass of BrC particles which can potentially have a large influence on aerosol-radiation interactions during time periods when they are prevalent. Differentiating between types of SP like tar balls or ASOPs can be time-consuming and rely on subtle differences (such as NEXAFS peak ratios). More study may be needed to be able to differentiate these SP types based on atmospheric and meteorological conditions. Further questions still exist about ASOPs specifically. How do soil characteristics affect the composition of ASOPs? How are ASOPs transformed as they travel through the atmosphere? What are the emissions factors of ASOPs? Answering questions like these may improve the quality of models in rainy areas or during rainy seasons when ASOPs are most prevalent.

Chapter 5: Speciation and Elemental Correlation of Lead Aerosols Collected in Northern Mexico City

5.1 Synopsis

To investigate lead speciation and mixing state of urban aerosol collected in Mexico City, X-ray Fluorescence (XRF) imaging and X-ray Absorption Near Edge Structure (XANES) spectroscopy performed at the Submicron Resolution X-ray (SRX) beamline at the National Synchrotron Light Source-II. These techniques were both used in tandem in order to locate and speciate lead rich particles. Calibration standards were used to obtain mass quantitative maps from elemental XRF images of Pb and Zn. Afterwards, k-means clustering was applied to the individual pixel XRF spectra where Pb, Zn, and Fe rich clusters were found where a slight correlation ($R^2 = 0.5$) was found within the Pb rich cluster between zinc and lead. Linear combination fitting and k-means clustering were applied to XANES spectra taken of Pb rich particles. Fitting of the overall average spectrum, using 10 lead standard spectra taken at the beamline, showed lead (II) sulfate and hydrocerussite as the main components. K-means clustering found 5 unique cluster types which, when the cluster averages were fit, showed the presence of 6 lead species: lead (II) sulfate, lead (II) nitrate, lead (II) carbonate, hydrocerussite (lead (II)), lead (II) chloride, and lead (II) sulfide, although the sulfate and nitrate spectra were difficult to distinguish. The lead particles here originate from garbage burning to the northwest of Mexico City. Each lead species present was hypothesized to be the result of reactions beginning with the combustion of printed circuit boards. The ability to speciate lead (or other metals within the energy range of a beamline like SRX at NSLS-II) as shown here can to help identify unique sources and inform regulatory bodies about harmful lead aerosol production. This speciation can also help determine how harmful a given lead aerosol will be depending on the solubility of the lead species found.

5.2 Introduction

Aerosol particles have been extensively documented to impart negative health effects upon those who inhale them.[14, 101, 230] Aerosol phase lead represents a significant concern for chronic exposure – especially by children and socioeconomically disadvantaged groups.[19, 231] Studies show that children with elevated blood lead levels consistently show small cognitive deficits after adjusting for social confounders.[232] The negative health effects of lead have been extensively documented and it has been suggested that the exact form of lead can influence bioavailability and interferes with normal, healthy function.[233-235] Moreover, the morphology of the particles dictate how deep into the lung they penetrate and therefore the effectiveness with which they enter the bloodstream.[236] Sources of lead aerosol are continually changing and becoming less significant as regulatory bodies push for decreased emissions. In the past 30-40 years leaded gasoline has been phased out of many developed and developing countries. Prior to that, gasoline combustion was a major source of aerosol phase lead emissions. Given all of the evidence linking the chemical and physical properties of lead aerosol to negative health effects, more detailed information regarding their speciation, sources, and morphology should lead to a better understanding of their negative effects on human health.

Mexico City is an example of a megacity in a developing country that continues to have relatively high atmospheric lead concentrations, particularly in the northern portions of the city.[237-239] Moreover, children living in these portions of the city were found to have an elevated blood lead level.[240] Early studies suggested that lead-glazed ceramic use and production was responsible for the increased blood lead levels.[241-242] In 2006, major field campaigns (MILAGRO/MAX-MEX/MCMA 2006) were conducted in Mexico City where it was found that lead aerosol in the northern part of the city was associated with zinc, chloride, and nitrate.[243] Due to the chemical associations of lead with chloride and zinc within individual particles, it was

hypothesized that lead may also be emitted in the process of garbage burning. Follow-up studies investigating garbage burning emissions in Mexico City were carried out and it was found that lead, zinc, and chloride were enhanced in garbage burns compared to cooking fires, brick and charcoal kilns, and stubble burns.[244] As hypothesized in our 2008 study, the source of chloride in the garbage burns was likely due to the combustion of polyvinyl chloride present in many electronics. Moreover, chloride from garbage burning may be a major contributor to particulate chloride in Mexico City.[245]

The association of lead with chloride in the particle samples from our 2008 study caused us to assert that lead was likely also present as $Pb(NO_3)_2$ by way of the reaction between $PbCl_2$ and nitric acid; this type of heterogeneous chemistry is common with other metal (sodium, zinc, potassium) chlorides. Zinc nitrate was measured directly using Scanning Transmission X-ray Microscopy Coupled with Near Edge X-ray Fine Structure (STXM/NEXAFS) spectroscopy at the zinc L-edge. However, the same sort of speciated measurements were not possible with lead due to the limitations of the synchrotron source employed. Here, we present speciation of the MILAGRO/MAX-MEX samples at the lead L-edge using the new Submicron Resolution X-ray (SRX) spectroscopy beamline at Brookhaven National Laboratory's National Synchrotron Light Source II in order to provide direct measurements of aerosol lead composition.

5.3 Experimental

5.3.1 Sample collection. Particles analyzed in this study were collected as part of the MCMA field campaign at the "T0" site located in northern Mexico City. The samples collected for this analysis have been extensively described elsewhere.[243, 246] All particles analyzed in this study were sampled by impaction onto Si_3N_4 membranes (Silson, LTD) using a Time Resolved Aerosol Collector (TRAC) with a flow rate of 0.8-0.9 SLPM .[247] The sample analyzed here was

collected by the TRAC on March 24th, 2006 at 09:29 GMT (04:29 LST) over a 15 minute period to prevent overloading. The sample period was selected due to heavy precipitation occurring the night before that served to deplete the background aerosol, leaving a large fraction of freshly emitted metal-bearing particles.[243]

5.3.2 Sub-micron resolution X-ray spectroscopy at NSLS-II. These samples were imaged at the Sub-micron Resolution X-ray (SRX) spectroscopy beamline (operating in high-flux mode) at the new National Synchrotron Light Source-II. Data was collected over the course of three separate beamtimes. At the SRX beamline, particle loaded regions were first located with a visual light microscope mounted along the beam bath. Selected regions were then scanned with an incident energy of 13,435 eV (400 eV above the Pb L edge to enable optimal contrast for Pb particles) focused down to ~0.5 μm (FWHM). Sample substrates were mounted and then raster scanned using stages with a range of 50 x 40 mm (H x V) and 5 nm resolution. At each pixel an X-ray fluorescence (XRF) spectrum was collected with an energy dispersive detector, creating an XRF map for each element detected. After Pb rich regions were found, a representative number of points were chosen for Pb X-ray absorption near edge structure (XANES) spectroscopy. At each point an absorption spectrum was collected over the Pb L edge from ~12.9 - 13.2 keV to gain more information regarding the oxidation state and speciation of Pb in the aerosol samples. Beamline fluctuations are accounted for in both XRF and XANES scans by an ion chamber situated before the sample.

5.3.3 X-Ray fluorescence mapping. After XRF images were taken, the images were processed using the open-source, python-based PyXRF program (https://github.com/NSLS-II/PyXRF).[248] The average fluorescence spectrum over all pixels of a given image was first fit with fluorescence peaks from elements found with the automatic element detection feature.

Elements were then added or removed based on prior knowledge of sample composition to fine tune the fit. From this, K-edge peaks for 13 elements were observed: Ar, Ca, Cl Cr, Cu, Fe, K, Mn, Ni, S, Si, Ti, and Zn as well as L-edge peaks for Pb. This collection of fitting parameters was applied to the individual XRF spectrum for each pixel of a given XRF image, allowing the contribution of each element to be determined on a pixel-by-pixel basis. From this, spatial distribution "maps" of raw intensity can be determined for each element observed. Each of these maps were then normalized by the (per-pixel) incident photon count determined by the ion chamber.

The raw, unfit XRF images of a single region were then clustered using the k-means algorithm (using sample correlation as a distance metric). Multiple regions of the XRF spectra showed little to no pixel-to-pixel variation across different regions of the sample. To better differentiate the XRF spectra, only specific regions of the spectra were used which corresponded to real elemental fluorescence peaks and excluding flat regions or peaks arising from the experimental setup. A small window of energies (about 200 eV wide) was used to clip out the 9 fluorescence peaks used in the clustering which corresponded to the elements: Cl, Ca, Cr, Mn, Fe, Ni, Cu, Zn, and Pb. This produced a piecewise spectrum with only regions of interest included. In addition to clustering only regions of the XRF spectra, the square root of the fluorescence intensity was used.[178] This was done to emphasize less abundant elements whose small variations would otherwise be ignored during clustering when compared to variations in more abundant elements.

5.3.4 Quantitative imaging. During the final set of measurements, a small 3x3 μm (36 points) XRF image was taken of two calibration standards (Micromatter, Canada. Serial #: 41152 and 41148) which contained a thin layer of well-mixed powdered salts and metals, with known

area densities, for the elements: Ca, Mn, Cu, K, Cl, Ti, Fe, Zn, and Pb. The normalized intensity XRF image for a given element was averaged and converted into ratios with the nominal area density for that element from the calibration standard. This ratio was then applied to the ambient aerosol samples to obtain quantitative area density maps for the 9 elements listed above. This procedure was only applied to data taken during the final beamtime as all scan parameters, such as aperture to sample distance and pixel exposure time, were kept constant.

5.3.5 Pb XANES spectroscopy. A set of 10 Pb standards were prepared to characterize the response of the SRX microscope to samples of known composition. The 10 standards used are listed below in Table 5.1. To prepare the standards, a small amount of each powdered standard was applied separately to the adhesive side of a piece of Kapton (DuPont, Delaware) tape, the excess was shaken off, and another piece of tape was used to seal the powder. Pb XANES spectra for each standard were collected, at least, in duplicate.

Table 5.1 Lead standards for XANES analysis

Standard	Formula	K_{sp}	Purity	Source
Lead (II) Sulfate	$PbSO_4$	1.6×10^{-8}	99.0%	Alpha Aesar
Lead (II) Nitrate	$Pb(NO_3)_2$	5.88	>99%	Fisher
Lead (II) Carbonate (Cerussite)	$PbCO_3$	7.4×10^{-14}	n.a.	Alpha Aesar
Hydrocerussite (Lead (II))	$2PbCO_3 \cdot Pb(OH)_2$	3.88×10^{-36}	99.0%	Alpha Aesar
Lead (II) doped Calcite (Synthetic)	Pb doped $CaCO_3$	3.8×10^{-9}	n.a.	Reeder lab
Lead (II) doped Calcite (Natural)	Pb doped $CaCO_3$	"		Tsumeb Mines
Lead (II) sulfide (Natural)	PbS	3×10^{-29}		
Lead (II) Chloride	$PbCl_2$	1.6×10^{-5}	99.0%	Alpha Aesar
Lead (II) oxide	PbO	1.2×10^{-15}	99.0%	Alpha Aesar
Lead (IV) oxide	PbO_2			

All Pb XANES (standards and ambient) spectra were imported into the Athena data

analysis software (https://bruceravel.github.io/demeter/).[249] Each replicate spectrum of a given

Pb standard was shifted in energy so that the absorption edge energies (E_0, measured by the

inflection point of a spectrum) were aligned. After alignment, the replicates were averaged.

Ambient aerosol spectra were individually checked and ones which were too noisy were

excluded from analysis (~5 spectra). Spectra with erroneous data points such as large positive or

negative spikes had those outlier points removed. The XANES spectra were then aligned, in two

steps, to facilitate averaging and further analysis. First, systematic calibration error during the

second beamtime needed to be corrected. All Pb spectra taken during this beamtime had an E_0

around 13,011 eV. Because this value is lower than the bare Pb E_0 value of 13,035 eV, these

spectra needed to be shifted higher in energy. To do this, the spectrum of $Pb(NO_3)_2$ (which was

collected during each beamtime) was used to calibrate the spectra from the second beamtime.

All spectra were then adjusted visually by aligning the first noticeable rise in the pre-edge region.

The 58 processed spectra were then exported to MatLab where they were interpolated over a

common energy vector to allow further processing.

The k-means clustering algorithm was applied to the 58 spectra in order to group them[177].

In an effort to cluster only the most distinct features of each spectra, the clustering was

performed over the energy range 13045 – 13094 eV. With the exception of the PbO_2 standard,

this range captures the E_0 value, the first, most intense, broad absorption peak (white line), and a

portion of the second absorption peak (if present). The appropriate number of clusters was

initially selected based on two common methods: the elbow method and the silhouette method[179].

With this, 5 unique spectral types were identified. Linear correlation coefficients between each

of the clusters and the standards were calculated to determine the major identity of each cluster.

Using the lead standards, linear combination fitting was applied to the overall average

spectrum and the average spectrum of each cluster to separate the components present. In order

to limit overfitting of the clusters, only a few of the lead standard spectra were used in each

fitting. This was determined for each cluster by first performing the fitting with the two most

correlated standards (from Table 5.3). Fitting was then repeated multiple times, each time

adding the next highest correlated standard. The fitting whose residuals had the smallest

standard deviation was chosen. Table 5.4 shows the fitting weights of the selected standards

with each of the average cluster spectra. As with the clustering, the fitting was also performed

over the same energy range of 13045 – 13094 eV. PbO_2 and both of the calcites were excluded

from both clustering and linear fitting analysis based on visual comparison with individual

spectra.

5.4 Results

5.4.1 Elemental Associations and Fluorescence Mapping. An example average XRF

spectrum from the Mexico City sample is shown in Figure 5.1. As expected for this sample, the

XRF spectrum shows a significant amount of zinc and lead. Other elements detected were:

copper, nickel, iron, manganese, chromium, calcium, and chlorine. The silicon peak is a result of

the Si-based XRF detector and the Ar peak due to the large sample-to-detector distance which

detects the fluorescence from atmospheric Ar. Chlorine, while observed and expected to be

present is difficult to quantify due to being overlapped by the large Ar peak. Previous

comparison of Mexico City aerosols have suggested Cl, Cr, Pb, and Zn originating from garbage

burning.[243] Mass spectrometry has observed Cu, Fe, Mn, Cr, and Ca before for this sampling

period.[250] Nickel was seen in previous proton induced X-ray emission (PIXE) data, where it was

observed in a 1:5 ratio with Vanadium.[239] This ratio has been linked to crude oil burning in

another study.[251] Vanadium, while absent here (with the Kα peak for Vanadium located at about

5 keV), was detected in mass spectrometry data by Moffet, *et al*. in 2008 which further supports

garbage incineration being the source of metal particles over oil burning for this sample.
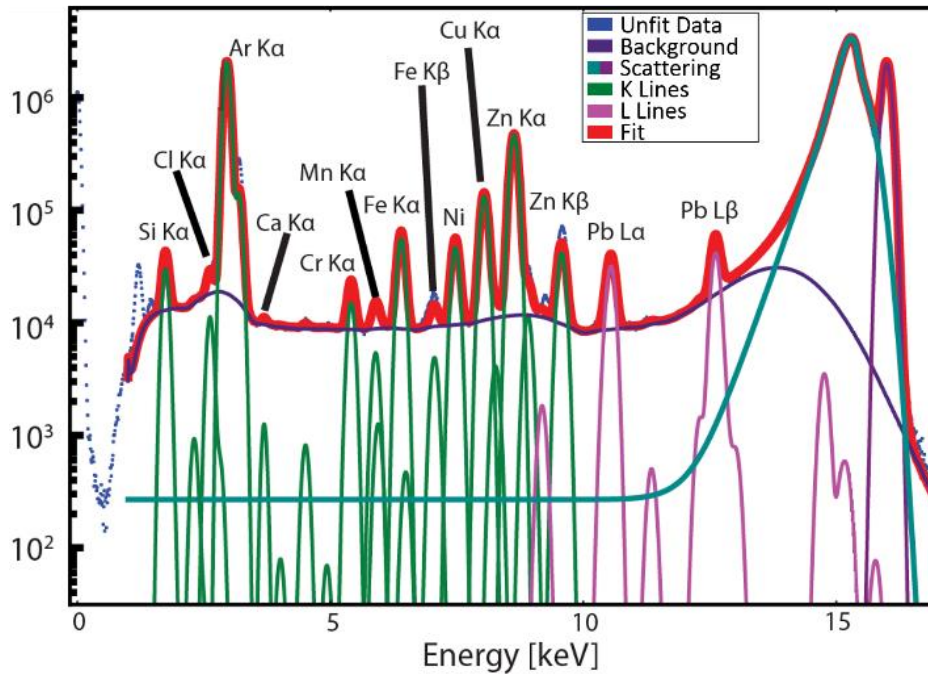
Figure 5.1 Example of a typical XRF spectrum and fit.

To help understand the types of particles present as well as their composition and

elemental associations, the per-pixel XRF spectra of one image were clustered using the k-means

algorithm. Four clusters were found with this method, 3 clusters rich in Zn, Fe, and Pb

respectively, and 1 cluster with moderate amounts of all elements. The average spectrum for

each cluster can be seen in Figure 5.2 below.
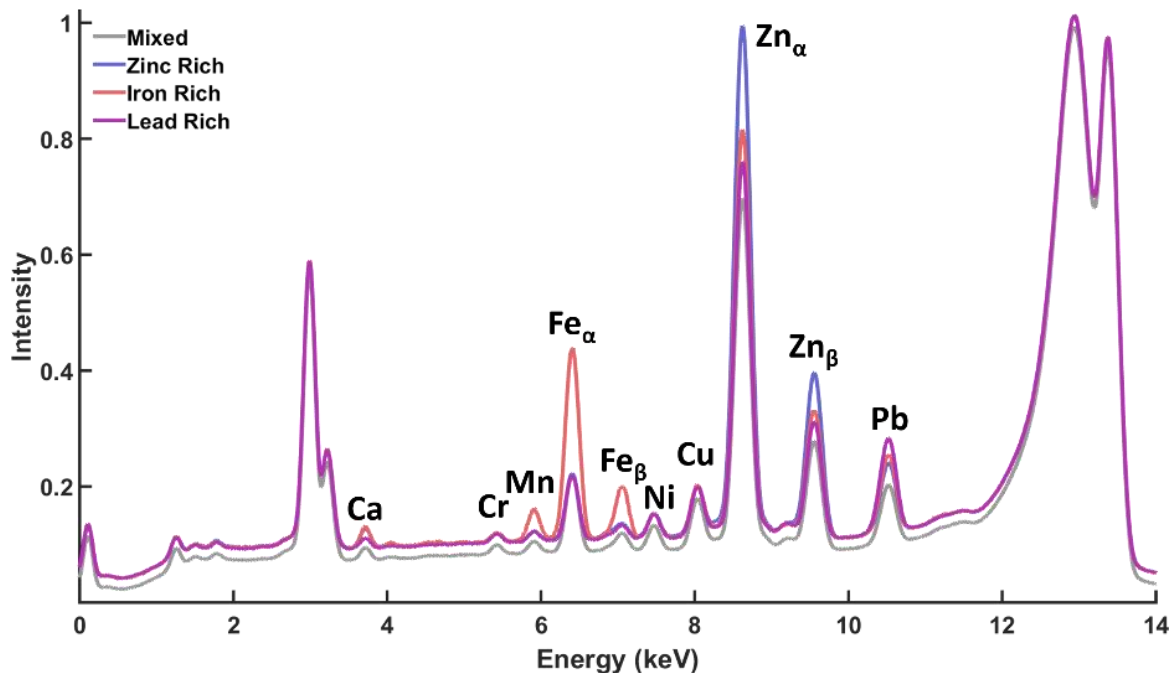
Figure 5.2 Average XRF spectra for 4 clusters identified with k-means. The mixed cluster is offset to highlight the other 3 clusters. The individual spectra that make up each cluster are all normalized to the highest peak (elastic scattering).

The mixed cluster was largely similar to the average spectrum for the sample. Regions assigned to this cluster may be more homogeneously mixed than other regions. In addition, the inability to resolve single particles will result in some homogenization of spectra like this. The Zn-rich cluster shows an elevated amount of Zn over what is present in the other clusters, although Zn is the most abundant element for the other clusters regardless. The Zn-rich cluster does not show elements other than Zn in different amounts than the mixed cluster. The Pb-rich cluster has a slightly elevated level of Pb compared to the other clusters while, like the Zn-rich cluster, no other elements vary when compared to the mixed cluster. Lastly, the Fe-rich cluster shows not only elevated Fe levels, but also elevated levels of Mn. This Fe-rich cluster may be associated with airborne dust produced from vehicles,[239, 252] the enhancement of both Fe and Mn could specifically suggest brake-dust.[253] The spatial distribution of each cluster identified above is shown in Figure 5.3 alongside quantitative maps of Pb, Zn, and Fe.
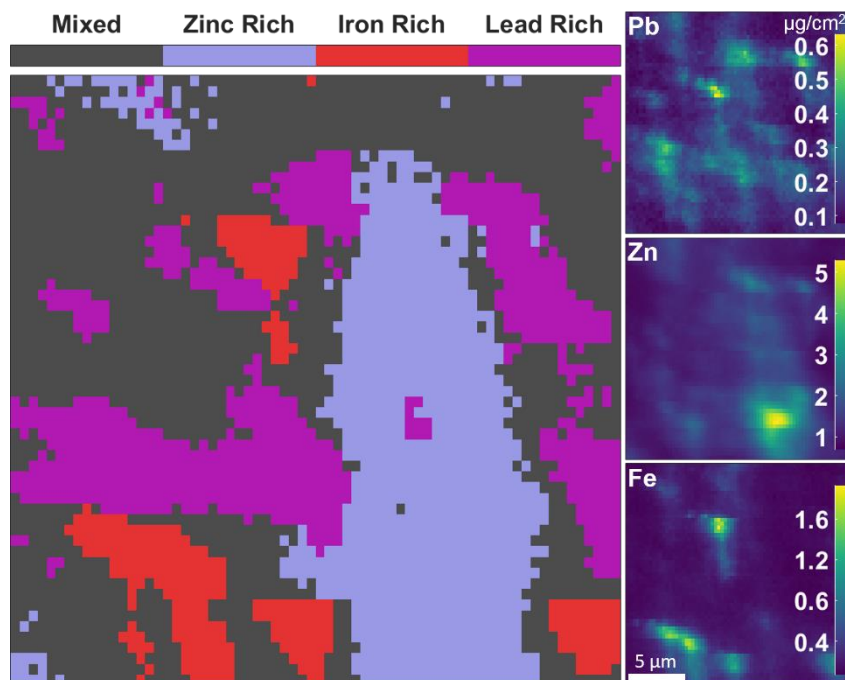
Figure 5.3 Distribution of clusters and quantitative mapping. (left) Spatial distribution of 4 clusters identified with k-means clustering. (right) Quantitative elemental maps for Pb, Zn, and Fe taken from the same XRF image.

The Pb and Fe rich clusters are scattered while the Zn cluster occupies a large continuous region. As expected from the average cluster XRF spectra, the Pb map shows the presence of Pb in regions with elevated Zn levels. To probe the relationship between these two elements, Figure 5.4 shows a correlation plot between Zn and Pb, color coded by cluster type. The mixed, zinc-rich, and iron-rich clusters all showed some colocation with lead, although the lead concentration was fairly constant. The lead-rich cluster, however, shows a slight positive correlation ($R^2 = 0.5$) between Pb and Zn. This association between Pb and Zn was been previously observed with single particle mass spectrometry data where waste incineration was implicated due to the strong presence of chlorine and nitrate.[243] More recent work on the common components of garbage suggests electronics (specifically printed circuit boards) as a major producer of Pb within a waste incinerator.[254] The Pb XANES spectra used below were chosen from these maps, with care taken to choose spots with the highest Pb concentration for clean spectra.
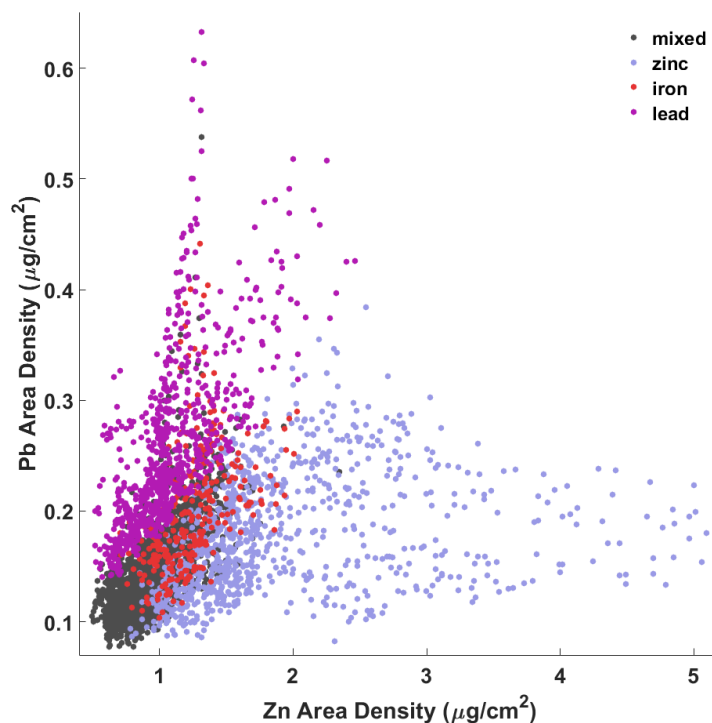
Figure 5.4 Correlation plot between Zn and Pb. Each data point is representing a pixel from the XRF map shown above in Figure 5.3.

5.4.2 Lead Speciation in Ambient Particles. To speciate the lead, 10 standard spectra

were taken on the SRX beamline. Shown in Figure 5.5, most of the standards are of the 2+

oxidation state with the exception of PbO_2. Because of this, most of the E_0 values were around

13,047 eV with the exception of the +4 standard, which had an E_0 5 eV higher at 13,052 eV. The

first peak after the absorption edge is known as the white line peak and it was significant in most

samples, with only hydrocerussite having a short and broad peak and $PbCl_2$ not having a defined

white line at all. This peak arises from 1s→np (continuum) transitions and its shape is defined

by the neighboring atoms, with strongly bound atoms and symmetrical atom arrangements

serving to broaden the absorption peak.[255] There is a second noticeable peak in most of the

standards which is shorter and broader than the white line located about 50 eV higher in energy.

This peak is the beginning of the Extended X-ray Absorption Fine Structure (EXAFS) region

where peaks and troughs correspond to interference patterns produced by neighboring atoms.

The further this peak is from the white line peak, the closer the distance between the central lead atom and its neighbors.[96]

While some of the smaller peaks or shoulders are difficult to resolve with the spectra in Figure 5.5, comparison with previous XANES spectra of the same standards is in fair agreement. $Pb(NO_3)_2$ shows a fairly sharp white line (~10 eV) along with a small second peak at about 13,080 eV whereas hydrocerussite has a short and broad white line and is fairly flat afterwards. Both of these spectra agree with Barrett, *et al.* (2010). The spectrum of $PbCl_2$ is relatively flat, save for the EXAFS peak at 13,090 eV which is the most intense peak in the spectrum. The spectra of $PbSO_4$ and $PbCO_3$ both look very similar to that of $Pb(NO_3)_2$ in many ways, however, while $PbSO_4$ has a sharp white line at 13,050 eV like $Pb(NO_3)_2$ it also has a more intense second peak at 13,090 eV. The $PbCO_3$ spectrum shows a white line shifted to higher energy (13,060 eV) than either the sulfate or nitrate standard. These three standards are in line with XANES spectra taken beforehand, though it remains difficult to differentiate the spectra.[255-256] Higher resolution spectra of $PbCO_3$ and $PbSO_4$ shows that the carbonate compound has a sharper, more intense white line and that the second peak is shifted about 5 eV higher in energy. In Figure 5.5, the spectrum for PbS shows a white line peak with a slight shoulder on the low energy side; in addition, a sharp drop can be seen beginning at around 13,100 eV. Lastly the lead oxides show a fairly broad white line peak and, in the PbO_2 spectrum, another broad peak at around 13,130 eV can be seen. The PbO_2 standard is the only one where a small pre-edge shoulder can be seen. In the higher resolution XANES spectra collected by Tan, *et al.* (2014) a small peak can be seen instead. This pre-edge peak corresponds to p/d orbital mixing when there is low inversion symmetry, like in the case of the tetragonal PbO_2.[96]
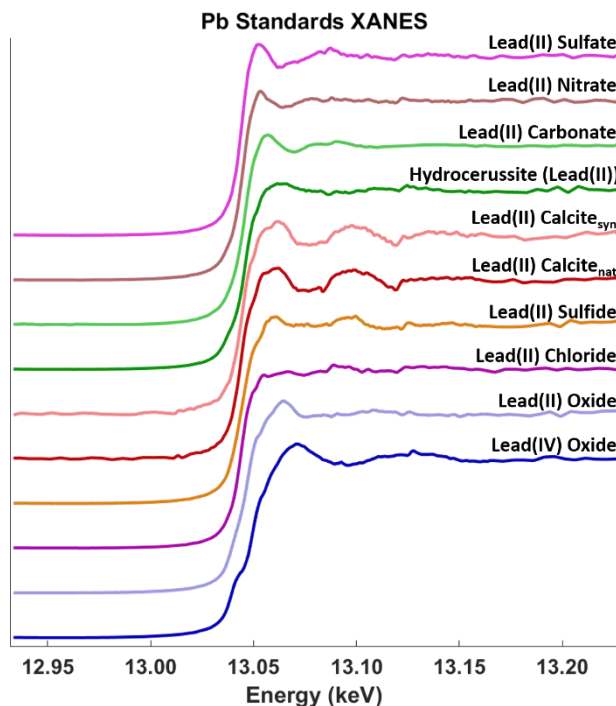
Figure 5.5 Lead XANES spectra for 10 standard compounds, taken on the SRX beamline.

5.4.2.1 Linear Combination Fitting. Prior STXM/NEXAFS measurements were not able to provide information regarding Pb speciation due to the limitations in the energy range available.[93] Figure 5.5 shows XANES spectra of 10 standard compounds, of which 7 (listed in Table 5.2) were hypothesized to be in the samples based on visual inspection of ambient XANES spectra and the elemental mixing state derived from our previous studies.[243, 250] Linear combination fitting was then performed on the overall average XANES spectrum. The resulting fitting weights, shown below in Table 5.2, represent the fraction each standard contributes to the fit spectrum.

Table 5.2 Linear combination fitting weights for the normalized overall average. Values in parentheses represent the size of the 95% confidence interval.

Standard	Weights (±Error)
Lead Sulfate	0.25 (0.19)
Lead Nitrate	0 (0.12)
Lead Carbonate	0.07 (0.05)
Hydrocerussite	0.25 (0.10)
Lead Sulfide	0.19 (0.06)
Lead Chloride	0.09 (0.05)
Lead (II) Oxide	0.15 (0.07)

The fitting of the overall average suggests $PbSO_4$ and hydrocerussite are the most prevalent components, with significant amounts of PbS and PbO. The weightings for $PbCO_3$, $PbCl_2$, and $Pb(NO_3)_2$ are low but the uncertainty in their weights makes their presence inconclusive from this linear fitting.

This type of analysis suffers from two main drawbacks with this data set. First, the difference between spectra, even with pure standards in high concentrations, is subtle. Figure 5.5 shows the similarity between $PbSO_4$ and $Pb(NO_3)_2$ which can be difficult to differentiate given noisy spectra from ambient samples. Second, the Pb XANES spectra taken here were taken from different points on the sample and from different particles. This heterogeneity may suppress some of the less prevalent components when only the overall average is considered.

5.4.2.2 K-Means Clustering. To remedy some of the issues considering only the overall average, the 58 individual spectra taken from different points on the sample substrate were clustered using the k-means algorithm. From this, 5 cluster types were found and linear correlation coefficients (shown in Table 5.3) were calculated between the averaged spectrum for each cluster and each of the Pb standards. The 5 clusters were most strongly correlated with $PbSO_4$, $Pb(NO_3)_2$, $PbCO_3$, $2PbCO_3 \cdot Pb(OH)_2$ (hydrocerussite), and $PbCl_2$.

Table 5.3 Correlation coefficients between average cluster spectra and lead standards. The highest correlation within a cluster type is bolded.

Standard	Cluster 1 N=20	Cluster 2 N=12	Cluster 3 N=10	Cluster 4 N=8	Cluster 5 N=8
Lead(II) Sulfate	**0.92**	0.71	0.11	-0.50	-0.04
Lead(II) Nitrate	0.80	**0.87**	0.51	0.03	0.35
Lead(II) Carbonate	0.51	0.81	**0.96**	0.60	0.73
Hydrocerussite (Lead(II))	-0.23	0.25	0.78	**0.99**	0.84
Lead(II) Sulfide	-0.07	0.36	0.88	0.90	0.91
Lead(II) Chloride	0.10	0.49	0.80	0.75	**0.97**
Lead(II) Oxide	-0.34	0.12	0.70	0.97	0.86

Although the linear correlation above shows that each cluster is associated with a major species, it is likely that multiple species are present within any given cluster. While this could be due to the association and mixing of different lead species in the atmosphere, the experimental conditions here must also be considered. Because the spot size of the beam used here is ~0.5 μm, which is larger than many of the aerosols present on this sample, any individual XANES spectrum is comprised of the signal from multiple different lead particles. In addition, because this sample was collected with a TRAC sampler, particles with a broad range of sizes (and therefore a broad range of potential sources) are present and so some homogenization of spectra is expected.

Even so, there is likely some degree of internal mixing between the lead species. Figure 5.6 shows visually how similar each cluster spectrum is with its major species by overlaying the highest correlated lead standard. While the clusters seem to match the standards shown fairly well, there are a few spots, which are clearly different, pointing to the presence of multiple species within each cluster.

Cluster Average XANES
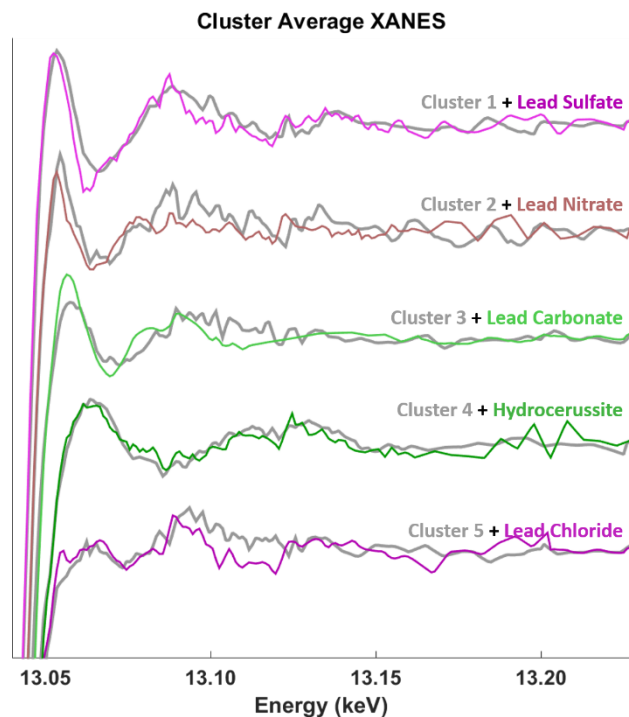
Figure 5.6 Average cluster spectra overlaid with the highest correlated lead standard spectra. Scaled to show detail, no discernable features (i.e. pre-edge peaks) are hidden from view.

5.4.2.3. Linear Combination Fitting of Clusters. To investigate the presence of multiple

species within each cluster, linear combination fitting was again performed, except this time on

the average cluster spectra.

Table 5.4 Linear Combination Fitting of Cluster Averages. Values in parentheses represent the size of the 95% confidence interval.

Standard	Cluster 1	Cluster 2	Cluster 3	Cluster 4	Cluster 5
Lead Sulfate	0.75 (0.06)	0.23 (0.06)	---	---	---
Lead Nitrate	0.25 (0.06)	0.78 (0.06)	---	---	---
Lead Carbonate	---	---	0.58 (0.06)	---	---
Hydrocerussite	---	---	---	0.70 (0.06)	---
Lead Sulfide	---	---	0.28 (0.03)	---	0.24 (0.07)
Lead Chloride	---	---	0.14 (0.05)	---	0.61 (0.09)
Lead (II) Oxide	---	---	---	0.30 (0.06)	0.16 (0.03)

Cluster 1 was most strongly associated with $PbSO_4$ while also being the most numerous, with 20 individual spectra. The previous mass spectrometry work on this sample showed that over half of the particles identified by the presence of Pb and Zn also had the HSO_4^- ion.[250] However, STXM/NEXAFS study of these same particles found no evidence of $ZnSO_4$, which reinforces $PbSO_4$ as the dominant form of the sulfate ion in these particles.[243] Additionally, in humid conditions PbO can react with $SO_{2(g)}$ via thin layer aqueous chemistry to form $PbSO_4$ according to the heterogeneous reaction:

$$PbO_{(s)} + SO_{2(g)} + H_2O_{(l)} \rightarrow PbO_{(s)} + HSO_{3(aq)}^- + H_{(aq)}^+ \rightarrow PbSO_{4(s)} + 2H_{(aq)}^+ \qquad \text{R5.1}$$
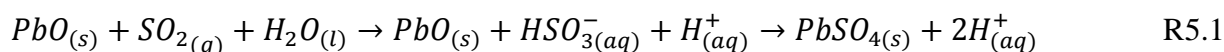
which, considering that these samples were taken after a rain event, may also explain the large presence of $PbSO_4$ in the ambient average.[257] While $Pb(NO_3)_2$ was also reportedly found in this cluster, the similarity between the two spectra makes the exact amount more uncertain.

Pb(NO_3)_2 was found in much greater abundance in cluster 2 however, along with a small amount of $PbSO_4$. In a similar fashion to sulfate ion, previous mass spectrometry data found that almost 100% of the particles containing Pb and Zn were also associated with nitrate and nitrite ions.[250] Although a greater correlation was observed with nitrate nitrite ions, only 12 spectra were present in this cluster. The greater number of $PbSO_4$ spectra found in the current work compared to $Pb(NO_3)_2$ spectra could suggest that while much of the sulfate is found associated with lead, the nitrate ions were preferentially associated with Zn. Because of the aforementioned similarity between the XANES spectra of $PbSO_4$ and $Pb(NO_3)_2$ however, more investigation is necessary. The use of Transmission Electron Microscopy (TEM) with Selected Area Electron Diffraction (SAED) would be well suited to answering this question which, because of the vastly different K_{sp} values between $PbSO_4$ and $Pb(NO_3)_2$, is an important piece in determining the health effects of these particles.

The presence of both $PbCO_3$ and hydrocerussite together in clusters 3 and 4 respectively is suggestive given their similar composition. Hydrocerussite (also called white lead or basic lead carbonate) can occur via the acid catalyzed reaction of $PbCO_3$ (also called cerussite) with $CO_{2(g)}$. $PbCO_3$ can result from similar thin layer aqueous chemistry as discussed with $PbSO_4$ in Reaction 5.1.[257] This two-step process, occurring especially under humid conditions, may account for the presence of hydrocerussite.

The main lead species found in Cluster 5 is sample $PbCl_2$ which, along with $Pb(NO_3)_2$, was hypothesized to exist in this sample. Based on single particle mass spectrometry data, it was hypothesized that $ZnCl_2$ was likely present in addition to $ZnNO_3$. Because this data also showed that almost 100% of the particles containing Pb and Zn also had nitrate and nitrite, a significant amount of $Pb(NO_3)_2$ was also hypothesized.[250] In general, divalent metal chlorides can be transformed into their nitrate counterpart via the following heterogeneous reaction:

$$MCl_{2(s)} + 2HNO_{3(g)} \rightarrow M(NO_3)_{2(s)} + 2HCl_{(g)} \quad\quad\quad\quad\quad R5.2$$
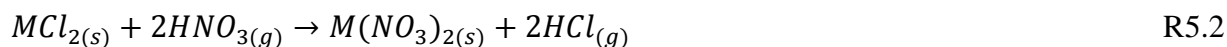
5.5 Conclusions

Here we provide direct evidence of the presence of both $PbCl_2$ and $Pb(NO_3)_2$ as was hypothesized in our previous study. We assert that the mixing of $PbCl_2$ and $Pb(NO_3)_2$ in the same regions of the particles is evidence of the common chloride chemistry shown in R2. These measurements confirm that when present as in the same particles, Pb and Zn exhibit similar chemistries.

As mentioned above, the lead and zinc-rich aerosols found here are thought to come from about 60 km northwest of Mexico City near Tula, Mexico where industrial emissions have been observed.[250] Lead and zinc rich particles are often emitted by metal smelting,[256, 258, 259] however the presence of chlorine and phosphates in Mexico City samples points to waste incineration as a

source instead.[243-244, 260] This chlorine is largely from the burning of PolyVinyl Chloride (PVC) plastics and is emitted initially as gaseous HCl.[244, 261-262, 262] The amount of chlorine released from burning increases from 3% to 30% when the trash is damp, as would be expected after a rain event.[263] The gaseous HCl will readily react with the Zn and Pb released from these garbage burns from the burning of printed circuit boards (from electronic waste in general).[254, 264, 265] This gives a clear pathway for Pb to first become $PbCl_2$, and then $Pb(NO_3)_2$ via Reaction 2 above. In the high temperatures used for waste incineration PbO can be formed from lead metal as well as from PbO_2.[144] From here PbS, $PbSO_4$, $PbCO_3$, and hydrocerussite are all potential reaction products with PbO as a reactant through aqueous layer reactions.[257] The result is the conversion of lead into multiple lead salts which tend to become more soluble (hydrocerussite is the most insoluble in water but becomes more soluble in acidic environments). The presence of nitric acid allows lead to be converted to the readily soluble $Pb(NO_3)_2$ which presents the greatest danger for health effects when inhaled.[266]

Here we demonstrate the use of combined XRF imaging and XANES spectroscopy to study Pb rich aerosols. XRF imaging allowed for Pb rich regions of a sample to be identified and selected for XANES spectroscopy in addition to probing spatial correlations between Pb and Zn. Quantitative elemental maps were also obtained from XRF imaging when a calibration standard was imaged under the same experimental conditions. Linear combination fitting of the overall average XANES spectrum identified the predominant lead species in the sample. More detailed lead speciation was achieved through k-means clustering followed by linear combination fitting of cluster averages, using only a narrow energy region of the Pb XANES spectrum for the analysis. This indicated the presence of exclusively lead (II) components: lead (II) sulfate, lead (II) nitrate, lead (II) chloride, lead (II) carbonate, lead (II) oxide, lead (II)

sulfide, and hydrocerussite found across different regions of the sample. This work supports the previous hypothesis that the Pb chemistry present in Mexico City aerosols follows the observed Zn chemistry. The improved understanding of Pb and its forms is a necessary step in mitigating or preventing the health hazards that it is associated with. Knowing the major forms of airborne lead can also bolster the predictive power of models to estimate lead's damaging effects or the potential benefit gained from new policies.

Chapter 6: Conclusions

Aerosols, especially those of human origin, can plague our environment and have disastrous effects on our health. It is for these reasons that a full understanding of aerosols, their compositions, and their sources is a pressing scientific issue. Of the many barriers to overcome in answering this issue, one of the largest is the complexity of individual aerosol particles. Knowing the bulk composition of particles can be useful in a number of ways but it is not sufficient. The degree to which components within individual particles are distributed and mixed can play a large role in how the aerosol population behaves. Properly studying the mixing state of aerosols and how various components are spatially distributed within them, requires single-particle techniques sensitive to composition. X-ray spectromicroscopic measurements like STXM/NEXAFS, SEM/EDX, and XRF/XANES are all ideally suited to tackle this problem.

The STXM/NEXAFS technique allows for the quantitative determination of component masses within aerosols; however, certain aspects of aerosol interactions, such as hygroscopicity, rely on volumes and volume fractions rather than mass. The ability for STXM/NEXAFS to measure both mass and volume quantitatively was validated experimentally using known standards. Particles created from standard solutions of inorganic/organic mixtures were made in the laboratory and used to test the OVF calculations under two circumstances: knowing the organic and inorganic composition *a priori*, and using proxies for the organic and inorganic components when they are not known. When the correct values for molecular formulae and densities are used, OVFs can be calculated to within 1% for organic-rich and inorganic-rich systems while equal mass systems of inorganic and organic aerosols can be calculated to within 4%. If the organic composition is not known beforehand, using adipic acid as a proxy can increase the error in OVF calculation by a very small (0.5%) amount showing that OVF is fairly insensitive to the assumed identity of the organic. A much larger error of 25% was observed if

NaCl is used as a proxy for the inorganic. Some of the standard solutions showed a large amount of phase separation which, although maintained an average OVF consistent with the OVF calculated from the bulk solution, greatly broadened the OVF distribution.

To make use of quantitative STXM/NEXAFS measurements, ambient particles from three different sites in the Amazon Basin near the megacity of Manaus were analyzed using STXM/NEXAFS and SEM/EDX. STXM/NEXAFS offered a quantitative measurement of light elements like C, N, and O whereas SEM/EDX allowed for heavier elements like Na, Mg, P, S, Cl, K, Ca, Mn, Fe, Ni, and Zn. Both of these techniques were combined in the same exact particles, yielding a near-complete elemental composition for each individual particle. Combining the two techniques in this way allowed the quantitative nature of STXM/NEXAFS to transform the semi-quantitative SEM/EDX measurements into a fully quantitative mass fraction for all 14 elements studied. From this, k-means clustering was performed to separate particles into 12 classes based on their elemental mass fractions. Clusters from the sampling site downwind of Manaus showed greater variety while the other sites had fewer clusters with less anthropogenic influence. A quantitative mixing state parameter was also applied to this 14 element mass fraction set, providing particle diversities and the mixing state parameter χ. The sampling site affected by Manaus had a low average particle diversity of about 2.4, while the less polluted sites showed a bimodal diversity distribution with a lower mode at 2.4 and a higher mode at approximately 3.6. The presence of this more diverse mode was suggestive of more aged particles and the less diverse mode suggested fresh emissions, which is to be expected from a large city with constant aerosol emissions.

While the mixing state of multi-component aerosols is worthy of investigation, another equally important aspect is how components within new particles are mixed upon formation.

Recently observed particles from the long-term ARM site in Lamont, Oklahoma are being emitted from the soil surface as purely organic particles. STXM/NEXAFS and SEM was used to investigate the formation and chemical properties of these spherical organic particles seen in the Southern Great Plains of Oklahoma. These particles are thought to be a heretofore unreported source of BrC. The SPs found using tilted SEM imaging were shown to be BrC based on a positive correlation between the %SP and the AAE for different samples. This correlation not only fit well for ambient samples ($R^2 = 0.85$) but when extrapolated to 100% SP it predicted AAE values of 2.5, consistent with previous observations of BrC samples. The influence of rainfall was also investigated, with some of the SPs observed being classified as tar balls and others classified as ASOPs based on meteorological data. ASOPs were observed in at least one sample with 35% SP showing that ASOPs can be an important aerosol type to consider immediately following rainfall. NEXAFS spectra were taken of both types of SP and compared with previously published literature spectra. Particles from the sample with a high % of ASOPs had smaller –COH peaks and a smaller –COOH/C=C peak ratio, consistent with published spectra. Lastly particles were generated from mud puddles to investigate the hypothesized source of the particles. When filtered and nebulized, particles from the mud puddles had a lot of inorganics, especially carbonate salts, compared to the purely organic particles that ASOPs are hypothesized to be. It was only when the aerosols were generated by bubbling N_2 gas through the liquid were organic spherical ASOPs seen, thereby reinforcing the rainfall generation mechanism for ASOPs.

Toxic particles have been previously observed in Mexico City containing mixtures of zinc and a high concentration of lead. Knowledge of the species (and therefore solubility) of lead comprising these particles is paramount to understanding their bioavailability and potential

for harm to the local population. In addition, studying the relationship between these mixed zinc

and lead particles may help determining their source. To this end, these previously studied

ambient particles from Mexico City were taken to the brand new XRF beamline at Brookhaven

National Laboratory. These particles were analyzed previously using mass spectrometry

methods and hypothesized to originate from garbage burning. At Brookhaven, both XRF

mapping and XANES spectra were taken of these lead particles. Quantitative mass maps were

created using XRF images of both ambient samples and standards, showing the spatial

distribution of metals like Pb, Zn, and Fe. Pixels in these quantitative maps were clustered to

investigate any metal colocation and a slight ($R^2 = 0.5$) correlation between lead and zinc were

found. XANES was performed on Pb-rich regions to determine the oxidation state and species

of Pb present. The XANES spectra were clustered together using the k-means algorithm and 5

cluster types were found. When compared with powder lead standards, 6 species of lead were

determined to be present: lead (II) sulfate, lead (II) nitrate, lead (II) carbonate, hydrocerrusite

(lead(II)), lead (II) chloride, and lead(II) sulfide. All of these lead compounds have been

observed previously in the burning of printed circuit boards, which supports the hypothesis that

garbage burning is the origin of these lead particles.

The work discussed in this dissertation gives only a small window into the variety and

complexity of aerosols and how composition can affect their behavior. Its purpose is to highlight

how aerosol origin, level of aging, and potential for harm can be deduced, in part, by the mixing

state of an aerosol sample. Expanding upon this work could involve longitudinal studies of

aerosol plumes to evaluate component mixing throughout the lifetime of groups of aerosols.

Towards the problem of climate modeling, further work could also be done to define the type of

mixing state that is most impactful. This may motivate a concerted effort to categorize aerosol

populations in these terms which would ultimately result in models with increased predictive

power and decreased uncertainty.

References

1. Seinfeld, J. H.; Pandis, S. N., *Atmospheric chemistry and physics: from air pollution to climate change*. John Wiley & Sons: 2006.
2. Lee, H.-H.; Bar-Or, R. Z.; Wang, C., Biomass burning aerosols and the low-visibility events in Southeast Asia. *Atmospheric Chemistry and Physics* **2017,** *17* (2), 965-980.
3. Cao, J.-j.; Wang, Q.-y.; Chow, J. C.; Watson, J. G.; Tie, X.-x.; Shen, Z.-x.; Wang, P.; An, Z.-s., Impacts of aerosol compositions on visibility impairment in Xi'an, China. *Atmospheric Environment* **2012,** *59*, 559-566.
4. Stocker, T.; Qin, D.; Plattner, G.; Tignor, M.; Allen, S.; Boschung, J.; Nauels, A.; Xia, Y.; Bex, V.; Midgley, P., Contribution of Working Group I to the Fifth Assessment Report of the Intergovernmental Panel on Climate Change. *Climate Change* **2013**.
5. Ramanathan, V.; Crutzen, P.; Kiehl, J.; Rosenfeld, D., Aerosols, climate, and the hydrological cycle. *science* **2001,** *294* (5549), 2119-2124.
6. Köhler, H., The nucleus in and the growth of hygroscopic droplets. *Transactions of the Faraday Society* **1936,** *32*, 1152-1161.
7. Pham, D. Q. The Effects of Sea Water Composition Aand Biological Activity on Individual Sea Spray Aerosols: Determination of Morphology, Composition, Organic Volume Fraction, and Hygroscopicity of Individual Particles Through X-Ray Microscopy. University of the Pacific, 2017.
8. CAICE Introduction to Aerosols. https://caice.ucsd.edu/research/introduction-to-aerosols/ (accessed 4/28).
9. Ramanathan, V.; Barkstrom, B. R.; Harrison, E. F., Climate and the Earth's radiation budget. *Physics Today* **1989**, 20.
10. IPCC AR6 Synthesis Report: Climate Change 2022. https://www.ipcc.ch/report/sixth-assessment-report-cycle/ (accessed May 28th).
11. Love, R. G.; Muir, D. C., Aerosol deposition and airway obstruction. *American Review of Respiratory Disease* **1976,** *114* (5), 891-897.
12. Salvaggio, J. E., Inhaled particles and respiratory disease. *Journal of Allergy and Clinical Immunology* **1994,** *94* (2), 304-309.
13. Dockery, D. W.; Pope, C. A.; Xu, X.; Spengler, J. D.; Ware, J. H.; Fay, M. E.; Ferris Jr, B. G.; Speizer, F. E., An association between air pollution and mortality in six US cities. *New England journal of medicine* **1993,** *329* (24), 1753-1759.
14. Laden, F.; Schwartz, J.; Speizer, F. E.; Dockery, D. W., Reduction in fine particulate air pollution and mortality: extended follow-up of the Harvard Six Cities study. *American journal of respiratory and critical care medicine* **2006,** *173* (6), 667-672.
15. Pope III, C. A.; Dockery, D. W., Health effects of fine particulate air pollution: lines that connect. *Journal of the Air & Waste Management Association* **2006,** *56* (6), 709-742.
16. EPA, America's Children and the Environment: Criteria Air Pollutants. Third ed.; 2015.
17. Cooper, R. G., Zinc toxicology following particulate inhalation. *Indian journal of occupational and environmental medicine* **2008,** *12* (1), 10.
18. Neuberger, J. S.; Hollowell, J. G., Lung cancer excess in an abandoned lead-zinc mining and smelting area. *Science of the Total Environment* **1982,** *25* (3), 287-294.
19. Lanphear, B. P.; Hornung, R.; Ho, M.; Howard, C. R.; Eberly, S.; Knauf, K., Environmental lead exposure during early childhood. *The Journal of Pediatrics* **2002,** *140* (1), 40-47.
20. Reist, P. C., *Introduction to aerosol science*. Macmillan publishing company: 1984.
21. Finlayson-Pitts, B. J.; Pitts Jr, J. N., *Chemistry of the upper and lower atmosphere: theory, experiments, and applications*. Elsevier: 1999.
22. Hodzic, A.; Jimenez, J. L.; Madronich, S.; Canagaratna, M.; DeCarlo, P. F.; Kleinman, L.; Fast, J., Modeling organic aerosols in a megacity: potential contribution of semi-volatile and intermediate volatility primary organic compounds to secondary organic aerosol formation. *Atmospheric Chemistry & Physics* **2010,** *10* (12).
23. Pandis, S. N.; Harley, R. A.; Cass, G. R.; Seinfeld, J. H., Secondary organic aerosol formation and transport. *Atmospheric Environment. Part A. General Topics* **1992,** *26* (13), 2269-2282.
24. Koppmann, R.; Czapiewski, K. v.; Reid, J., A review of biomass burning emissions, part I: gaseous emissions of carbon monoxide, methane, volatile organic compounds, and nitrogen containing compounds. *Atmospheric Chemistry and Physics Discussions* **2005,** *5* (5), 10455-10516.
25. Watson, C. E.; Fishman, J.; Reichle, H. G., The significance of biomass burning as a source of carbon monoxide and ozone in the southern hemisphere tropics: A satellite analysis. *Journal of Geophysical Research: Atmospheres* **1990,** *95* (D10), 16443-16450.

26.   Whitby, K. T., The physical characteristics of sulfur aerosols. In *Sulfur in the Atmosphere*, Elsevier: 1978; pp 135-159.

27.   Jillavenkatesa, A.; Dapkunas, S. J.; Lum, L.-S. H., *Particle size characterization*. National Institute of Standards and Technology Washington, DC: 2001; Vol. 960.

28.   Koçak, M.; Mihalopoulos, N.; Kubilay, N., Chemical composition of the fine and coarse fraction of aerosols in the northeastern Mediterranean. *Atmospheric Environment* **2007,** *41* (34), 7351-7368.

29.   Aitken, J., On some nuclei of cloudy condensation. *Transactions of the Royal Society of Edinburgh* **1898,** *39* (3), 15-25.

30.   Kondratyev, K. Y.; Ivlev, L. S.; Krapivin, V. F.; Varostos, C. A., *Atmospheric aerosol properties: Formation, processes and impacts*. Springer Science & Business Media: 2006.

31.   Ramabhadran, T.; Peterson, T.; Seinfeld, J., Dynamics of aerosol coagulation and condensation. *AIChE Journal* **1976,** *22* (5), 840-851.

32.   ParticleMeasuringSystems Particle Transportation. https://www.pmeasuring.com/blog/particle-transportation/ (accessed May 28).

33.   Jaenicke, R., Tropospheric aerosols. In *International Geophysics*, Elsevier: 1993; Vol. 54, pp 1-31.

34.   Andreae, M. O., Soot carbon and excess fine potassium: Long-range transport of combustion-derived aerosols. *Science* **1983,** *220* (4602), 1148-1151.

35.   Simoneit, B. R.; Schauer, J. J.; Nolte, C.; Oros, D. R.; Elias, V. O.; Fraser, M.; Rogge, W.; Cass, G. R., Levoglucosan, a tracer for cellulose in biomass burning and atmospheric particles. *Atmospheric Environment* **1999,** *33* (2), 173-182.

36.   McDonald, J. E., Homogeneous nucleation of vapor condensation. I. Thermodynamic aspects. *American Journal of Physics* **1962,** *30* (12), 870-877.

37.   Pham, D. Q.; O'Brien, R.; Fraund, M.; Bonanno, D.; Laskina, O.; Beall, C.; Moore, K. A.; Forestieri, S.; Wang, X.; Lee, C., Biological Impacts on Carbon Speciation and Morphology of Sea Spray Aerosol. *ACS Earth and Space Chemistry* **2017,** *1* (9), 551-561.

38.   Zaveri, R. A.; Barnard, J. C.; Easter, R. C.; Riemer, N.; West, M., Particle-resolved simulation of aerosol size, composition, mixing state, and the associated optical and cloud condensation nuclei activation properties in an evolving urban plume. *Journal of Geophysical Research: Atmospheres* **2010,** *115* (D17).

39.   Jacobson, M. Z., GATOR-GCMM: A global-through urban-scale air pollution and weather forecast model: 1. Model design and treatment of subgrid soil, vegetation, roads, rooftops, water, sea ice, and snow. *Journal of Geophysical Research: Atmospheres* **2001,** *106* (D6), 5385-5401.

40.   Weingartner, E.; Burtscher, H.; Baltensperger, U., Hygroscopic properties of carbon and diesel soot particles. *Atmospheric Environment* **1997,** *31* (15), 2311-2327.

41.   Riemer, N.; West, M., Quantifying aerosol mixing state with entropy and diversity measures. *Atmospheric Chemistry and Physics* **2013,** *13* (22), 11423-11439.

42.   Chakrabarty, R.; Moosmüller, H.; Chen, L.-W.; Lewis, K.; Arnott, W.; Mazzoleni, C.; Dubey, M.; Wold, C.; Hao, W.; Kreidenweis, S., Brown carbon in tar balls from smoldering biomass combustion. *Atmospheric Chemistry and Physics* **2010,** *10* (13), 6363-6370.

43.   Wang, B.; Harder, T. H.; Kelly, S. T.; Piens, D. S.; China, S.; Kovarik, L.; Keiluweit, M.; Arey, B. W.; Gilles, M. K.; Laskin, A., Airborne soil organic particles generated by precipitation. *Nature géoscience* **2016,** *9* (6), 433.

44.   Liu, P.; Wang, C., The Diesel Soot Particles Fractal Growth Model and Its Agglomeration Control. In *Kinetic Modeling for Environmental Systems*, IntechOpen: 2018.

45.   Frenklach, M., Reaction mechanism of soot formation in flames. *Physical chemistry chemical Physics* **2002,** *4* (11), 2028-2037.

46.   Zhang, R.; Khalizov, A. F.; Pagels, J.; Zhang, D.; Xue, H.; McMurry, P. H., Variability in morphology, hygroscopicity, and optical properties of soot aerosols during atmospheric processing. *Proceedings of the National Academy of Sciences* **2008,** *105* (30), 10291-10296.

47.   Ma, X.; Zangmeister, C. D.; Gigault, J.; Mulholland, G. W.; Zachariah, M. R., Soot aggregate restructuring during water processing. *Journal of Aerosol Science* **2013,** *66*, 209-219.

48.   DOEscience Scratching the Surface. https://www.eurekalert.org/features/doe/2015-12/dmsl-sts122315.php (accessed May-15).

49.   China, S.; Kulkarni, G.; Scarnato, B. V.; Sharma, N.; Pekour, M.; Shilling, J. E.; Wilson, J.; Zelenyuk, A.; Chand, D.; Liu, S., Morphology of diesel soot residuals from supercooled water droplets and ice crystals: implications for optical properties. *Environmental Research Letters* **2015,** *10* (11), 114010.

50.	Bond, T. C.; Doherty, S. J.; Fahey, D.; Forster, P.; Berntsen, T.; DeAngelo, B.; Flanner, M.; Ghan, S.; Kärcher, B.; Koch, D., Bounding the role of black carbon in the climate system: A scientific assessment. *Journal of Geophysical Research: Atmospheres* **2013,** *118* (11), 5380-5552.

51.	Adachi, K.; Chung, S. H.; Buseck, P. R., Shapes of soot aerosol particles and implications for their effects on climate. *Journal of Geophysical Research: Atmospheres* **2010,** *115* (D15).

52.	Liu, D.; Whitehead, J.; Alfarra, M. R.; Reyes-Villegas, E.; Spracklen, D. V.; Reddington, C. L.; Kong, S.; Williams, P. I.; Ting, Y.-C.; Haslett, S., Black-carbon absorption enhancement in the atmosphere determined by particle mixing state. *Nature Geoscience* **2017,** *10* (3), 184-188.

53.	Tervahattu, H.; Juhanoja, J.; Kupiainen, K., Identification of an organic coating on marine aerosol particles by TOF-SIMS. *Journal of Geophysical Research: Atmospheres* **2002,** *107* (D16), ACH 18-1-ACH 18-7.

54.	Peckhaus, A.; Grass, S.; Treuel, L.; Zellner, R., Deliquescence and efflorescence behavior of ternary inorganic/organic/water aerosol particles. *The Journal of Physical Chemistry A* **2012,** *116* (24), 6199-6210.

55.	Veghte, D. P.; Altaf, M. B.; Freedman, M. A., Size dependence of the structure of organic aerosol. *Journal of the American Chemical Society* **2013,** *135* (43), 16046-16049.

56.	Menzel, N.; Schramel, P.; Wittmaack, K., Elemental composition of aerosol particulate matter collected on membrane filters: A comparison of results by PIXE and ICP-AES. *Nuclear Instruments and Methods in Physics Research Section B: Beam Interactions with Materials and Atoms* **2002,** *189* (1-4), 94-99.

57.	Artaxo, P.; Gerab, F.; Rabello, M. L., Elemental composition of aerosol particles from two atmospheric monitoring stations in the Amazon Basin. *Nuclear Instruments and Methods in Physics Research Section B: Beam Interactions with Materials and Atoms* **1993,** *75* (1-4), 277-281.

58.	Lindberg, S.; Harriss, R., Water and acid soluble trace metals in atmospheric particles. *Journal of Geophysical Research: Oceans* **1983,** *88* (C9), 5091-5100.

59.	Allen, D. T.; Palen, E., Recent advances in aerosol analysis by infrared spectroscopy. *Journal of aerosol science* **1989,** *20* (4), 441-455.

60.	Quincey, P.; Butterfield, D.; Green, D.; Coyle, M.; Cape, J. N., An evaluation of measurement methods for organic, elemental and black carbon in ambient air monitoring sites. *Atmospheric Environment* **2009,** *43* (32), 5085-5091.

61.	Cachier, H.; Bremond, M.-P.; Buat-Menard, P., Determination of atmospheric soot carbon with a simple thermal method. *Tellus B: Chemical and Physical Meteorology* **1989,** *41* (3), 379-390.

62.	Karanasiou, A.; Minguillón, M.; Viana, M.; Alastuey, A.; Putaud, J.-P.; Maenhaut, W.; Panteliadis, P.; Močnik, G.; Favez, O.; Kuhlbusch, T., Thermal-optical analysis for the measurement of elemental carbon (EC) and organic carbon (OC) in ambient air a literature review. *Atmospheric Measurement Techniques Discussions* **2015,** *8* (9).

63.	Budisulistiorini, S.; Canagaratna, M.; Croteau, P.; Baumann, K.; Edgerton, E.; Kollman, M.; Ng, N.; Verma, V.; Shaw, S.; Knipping, E., Intercomparison of an Aerosol Chemical Speciation Monitor (ACSM) with ambient fine aerosol measurements in downtown Atlanta, Georgia. *Atmospheric Measurement Techniques* **2014,** *7* (7), 1929-1941.

64.	Ng, N. L.; Herndon, S. C.; Trimborn, A.; Canagaratna, M. R.; Croteau, P.; Onasch, T. B.; Sueper, D.; Worsnop, D. R.; Zhang, Q.; Sun, Y., An Aerosol Chemical Speciation Monitor (ACSM) for routine monitoring of the composition and mass concentrations of ambient aerosol. *Aerosol Science and Technology* **2011,** *45* (7), 780-794.

65.	Cremers, D. A.; Multari, R. A.; Knight, A. K., Laser-induced breakdown spectroscopy. *Encyclopedia of Analytical Chemistry: Applications, Theory and Instrumentation* **2006**, 1-28.

66.	Miziolek, A. W.; Palleschi, V.; Schechter, I., *Laser induced breakdown spectroscopy*. Cambridge University Press: 2006.

67.	Hahn, D. W.; Omenetto, N., Laser-induced breakdown spectroscopy (LIBS), part II: review of instrumental and methodological approaches to material analysis and applications to different fields. *Applied Spectroscopy* **2012,** *66* (4), 347-419.

68.	Redoglio, D. A.; Palazzo, N.; Migliorini, F.; Dondè, R.; De Iuliis, S., Laser-Induced Breakdown Spectroscopy Analysis of Lead Aerosol in Nitrogen and Air Atmosphere. *Applied Spectroscopy* **2018,** *72* (4), 584-590.

69.	Dudragne, L.; Adam, P.; Amouroux, J., Time-resolved laser-induced breakdown spectroscopy: application for qualitative and quantitative detection of fluorine, chlorine, sulfur, and carbon in air. *Applied Spectroscopy* **1998,** *52* (10), 1321-1327.

70.	Gao, R.; Schwarz, J.; Kelly, K.; Fahey, D.; Watts, L.; Thompson, T.; Spackman, J.; Slowik, J.; Cross, E.; Han, J.-H., A novel method for estimating light-scattering properties of soot aerosols using a modified single-particle soot photometer. *Aerosol Science and Technology* **2007,** *41* (2), 125-135.

71.   Schwarz, J.; Spackman, J.; Gao, R.; Perring, A.; Cross, E.; Onasch, T.; Ahern, A.; Wrobel, W.; Davidovits, P.; Olfert, J., The detection efficiency of the single particle soot photometer. *Aerosol science and technology* **2010,** *44* (8), 612-628.

72.   Huang, X.-F.; Sun, T.-L.; Zeng, L.-W.; Yu, G.-H.; Luan, S.-J., Black carbon aerosol characterization in a coastal city in South China using a single particle soot photometer. *Atmospheric environment* **2012,** *51*, 21-28.

73.   Raatikainen, T.; Brus, D.; Hyvärinen, A.-P.; Svensson, J.; Asmi, E.; Lihavainen, H., Black carbon concentrations and mixing state in the Finnish Arctic. *Atmospheric Chemistry and Physics* **2015,** *15* (17), 10057-10070.

74.   Baumgardner, D.; Kok, G.; Raga, G., Warming of the Arctic lower stratosphere by light absorbing particles. *Geophysical Research Letters* **2004,** *31* (6).

75.   Schwarz, J.; Gao, R.; Fahey, D.; Thomson, D.; Watts, L.; Wilson, J.; Reeves, J.; Darbeheshti, M.; Baumgardner, D.; Kok, G., Single-particle measurements of midlatitude black carbon and light-scattering aerosols from the boundary layer to the lower stratosphere. *Journal of Geophysical Research: Atmospheres* **2006,** *111* (D16).

76.   Spencer, M. T.; Prather, K. A., Using ATOFMS to determine OC/EC mass fractions in particles. *Aerosol Science and Technology* **2006,** *40* (8), 585-594.

77.   Zelenyuk, A.; Imre, D., Single particle laser ablation time-of-flight mass spectrometer: an introduction to SPLAT. *Aerosol Science and Technology* **2005,** *39* (6), 554-568.

78.   Moffet, R. C.; Prather, K. A., Extending ATOFMS measurements to include refractive index and density. *Analytical chemistry* **2005,** *77* (20), 6535-6541.

79.   Marple, V. A.; Rubow, K. L.; Behm, S. M., A microorifice uniform deposit impactor (MOUDI): Description, calibration, and use. *Aerosol Science and Technology* **1991,** *14* (4), 434-446.

80.   Binnig, G.; Quate, C. F.; Gerber, C., Atomic force microscope. *Physical review letters* **1986,** *56* (9), 930.

81.   Goldstein, J. I.; Newbury, D. E.; Michael, J. R.; Ritchie, N. W.; Scott, J. H. J.; Joy, D. C., *Scanning electron microscopy and X-ray microanalysis*. Springer: 2017.

82.   Reimer, L., *Transmission electron microscopy: physics of image formation and microanalysis*. Springer: 2013; Vol. 36.

83.   Ault, A. P.; Axson, J. L., Atmospheric Aerosol Chemistry: Spectroscopic and Microscopic Advances. *Analytical Chemistry* **2016,** *89* (1), 430-452.

84.   Tan, H.; Turner, S.; Yücelen, E.; Verbeeck, J.; Van Tendeloo, G., 2D atomic mapping of oxidation states in transition metal oxides by scanning transmission electron microscopy and electron energy-loss spectroscopy. *Physical review letters* **2011,** *107* (10), 107602.

85.   Ramasse, Q. M.; Seabourne, C. R.; Kepaptsoglou, D.-M.; Zan, R.; Bangert, U.; Scott, A. J., Probing the bonding and electronic structure of single atom dopants in graphene with electron energy loss spectroscopy. *Nano letters* **2013,** *13* (10), 4989-4995.

86.   Egerton, R. F., Electron energy-loss spectroscopy in the TEM. *Reports on Progress in Physics* **2008,** *72* (1), 016502.

87.   Jackson, J.; Panofsky, W., Edwin Mattison McMillan: A Biographical Memoir. *National Academy of Sciences, Washington DC* **1996**.

88.   Wiedemann, H., Synchrotron radiation. In *Particle Accelerator Physics*, Springer: 2003; pp 647-686.

89.   Moffet, R. C., Scanning transmission X-ray microscopy: Applications in atmospheric aerosol research. *Lawrence Berkeley National Laboratory* **2011**.

90.   Spiller, E., *Soft X-ray optics*. SPIE Optical Engineering Press Bellingham, WA: 1994.

91.   Kilcoyne, A.; Tyliszczak, T.; Steele, W.; Fakra, S.; Hitchcock, P.; Franck, K.; Anderson, E.; Harteneck, B.; Rightor, E.; Mitchell, G., Interferometer-controlled scanning transmission X-ray microscopes at the Advanced Light Source. *Journal of Synchrotron Radiation* **2003,** *10* (2), 125-136.

92.   Henke, B. L.; Gullikson, E. M.; Davis, J. C., X-ray interactions: photoabsorption, scattering, transmission, and reflection at E= 50-30,000 eV, Z= 1-92. *Atomic Data and Nuclear Data Tables* **1993,** *54* (2), 181-342.

93.   Moffet, R. C.; Tivanski, A. V.; Gilles, M. K., Scanning Transmission X-ray Microscopy: Applications in Atmospheric Aerosol Research. In *Fundamentals and Applications in Aerosol Spectroscopy*, 2010; p 419.

94.   ALS LINAC. https://www2.lbl.gov/MicroWorlds/ALSTool/ALS_Components/Linac/ (accessed May 28).

95.   Orloff, J., *Handbook of charged particle optics*. CRC press: 2008.

96.   Bunker, G., *Introduction to XAFS: a practical guide to X-ray absorption fine structure spectroscopy*. Cambridge University Press: 2010.

97.   Guizar-Sicairos, M.; Thurman, S. T.; Fienup, J. R., Efficient subpixel image registration algorithms. *Optics Letters* **2008,** *33* (2), 156-158.

98.   Otsu, N., A threshold selection method from gray-level histograms. *Automatica* **1975,** *11* (285-296), 23-27.

99.   Ingle Jr, J. D.; Crouch, S. R., Spectrochemical analysis. **1988**.

100.   Moffet, R. C.; Henn, T.; Laskin, A.; Gilles, M. K., Automated Chemical Analysis of Internally Mixed Aerosol Particles Using X-ray Spectromicroscopy at the Carbon K-Edge†. *Analytical Chemistry* **2010,** *82* (19), 7906-7914.

101.   Villeneuve, P. J.; Goldberg, M. S.; Krewski, D.; Burnett, R. T.; Chen, Y., Fine particulate air pollution and all-cause mortality within the Harvard Six-Cities Study: Variations in risk by period of exposure. *Annals of Epidemiology* **2002,** *12* (8), 568-576.

102.   Pöschl, U., Atmospheric aerosols: composition, transformation, climate and health effects. *Angewandte Chemie International Edition* **2005,** *44* (46), 7520-7540.

103.   Chow, J. C., Measurement methods to determine compliance with ambient air quality standards for suspended particles. *Journal of the Air & Waste Management Association* **1995,** *45* (5), 320-382.

104.   Asano, H.; Aoyama, T.; Mizuno, Y.; Shiraishi, Y., Highly Time-Resolved Atmospheric Observations Using a Continuous Fine Particulate Matter and Element Monitor. *ACS Earth and Space Chemistry* **2017,** *1* (9), 580-590.

105.   Canagaratna, M.; Jayne, J.; Jimenez, J.; Allan, J.; Alfarra, M.; Zhang, Q.; Onasch, T.; Drewnick, F.; Coe, H.; Middlebrook, A., Chemical and microphysical characterization of ambient aerosols with the aerodyne aerosol mass spectrometer. *Mass Spectrometry Reviews* **2007,** *26* (2), 185-222.

106.   Healy, R. M.; Sciare, J.; Poulain, L.; Crippa, M.; Wiedensohler, A.; Prévôt, A. S.; Baltensperger, U.; Sarda-Estève, R.; McGuire, M. L.; Jeong, C.-H., Quantitative determination of carbonaceous particle mixing state in Paris using single-particle mass spectrometer and aerosol mass spectrometer measurements. *Atmospheric Chemistry and Physics* **2013,** *13* (18), 9479-9496.

107.   Moffet, R. C.; O'Brien, R. E.; Alpert, P. A.; Kelly, S. T.; Pham, D. Q.; Gilles, M. K.; Knopf, D. A.; Laskin, A., Morphology and mixing of black carbon particles collected in central California during the CARES field study. *Atmospheric Chemistry and Physics* **2016,** *16* (22), 14515-14525.

108.   Adachi, K.; Buseck, P., Internally mixed soot, sulfates, and organic matter in aerosol particles from Mexico City. *Atmospheric Chemistry and Physics* **2008,** *8* (21), 6469-6481.

109.   Ghosal, S.; Weber, P. K.; Laskin, A., Spatially resolved chemical imaging of individual atmospheric particles using nanoscale imaging mass spectrometry: Insight into particle origin and chemistry. *Analytical Methods* **2014,** *6* (8), 2444-2451.

110.   Li, W.; Sun, J.; Xu, L.; Shi, Z.; Riemer, N.; Sun, Y.; Fu, P.; Zhang, J.; Lin, Y.; Wang, X., A conceptual framework for mixing structures in individual aerosol particles. *Journal of Geophysical Research: Atmospheres* **2016,** *121* (22).

111.   Li, W.; Xu, L.; Liu, X.; Zhang, J.; Lin, Y.; Yao, X.; Gao, H.; Zhang, D.; Chen, J.; Wang, W., Air pollution–aerosol interactions produce more bioavailable iron for ocean ecosystems. *Science advances* **2017,** *3* (3), e1601749.

112.   Warwick, T.; Ade, H.; Kilcoyne, D.; Kritscher, M.; Tyliscczak, T.; Fakra, S.; Hitchcock, A.; Hitchcock, P.; Padmore, H., A new bend-magnet beamline for scanning transmission X-ray microscopy at the Advanced Light Source. *Journal of synchrotron radiation* **2002,** *9* (4), 254-257.

113.   Laskin, A.; Cowin, J. P.; Iedema, M. J., Analysis of individual environmental particles using modern methods of electron microscopy and X-ray microanalysis. *Journal of Electron Spectroscopy and Related Phenomena* **2006,** *150* (2), 260-274.

114.   Fraund, M.; Pham, D. Q.; Bonanno, D.; Harder, T. H.; Wang, B.; Brito, J.; de Sá, S. S.; Carbone, S.; China, S.; Artaxo, P., Elemental Mixing State of Aerosol Particles Collected in Central Amazonia during GoAmazon2014/15. *Atmosphere* **2017,** *8* (9), 173.

115.   Piens, D. S.; Kelly, S. T.; Harder, T. H.; Petters, M. D.; O'Brien, R. E.; Wang, B.; Teske, K.; Dowell, P.; Laskin, A.; Gilles, M. K., Measuring mass-based hygroscopicity of atmospheric particles through in situ imaging. *Environmental Science & Technology* **2016,** *50* (10), 5172-5180.

116.   Worsnop, D.; Morris, J.; Shi, Q.; Davidovits, P.; Kolb, C., A chemical kinetic model for reactive transformations of aerosol particles. *Geophysical research letters* **2002,** *29* (20).

117.   Maria, S. F.; Russell, L. M.; Gilles, M. K.; Myneni, S. C., Organic aerosol growth mechanisms and their climate-forcing implications. *Science* **2004,** *306* (5703), 1921-1924.

118.   Cruz, C. N.; Pandis, S. N., The effect of organic coatings on the cloud condensation nuclei activation of inorganic atmospheric aerosol. *Journal of Geophysical Research: Atmospheres* **1998,** *103* (D11), 13111-13123.

119.   Möhler, O.; Benz, S.; Saathoff, H.; Schnaiter, M.; Wagner, R.; Schneider, J.; Walter, S.; Ebert, V.; Wagner, S., The effect of organic coating on the heterogeneous ice nucleation efficiency of mineral dust aerosols. *Environmental Research Letters* **2008,** *3* (2), 025007.

120.   Beydoun, H.; Polen, M.; Sullivan, R. C., A new multicomponent heterogeneous ice nucleation model and its application to Snomax bacterial particles and a Snomax–illite mineral particle mixture. *Atmospheric Chemistry and Physics* **2017,** *17* (22), 13545-13557.

121.	Petters, M.; Kreidenweis, S., A single parameter representation of hygroscopic growth and cloud condensation nucleus activity. *Atmospheric Chemistry and Physics* **2007,** *7* (8), 1961-1971.

122.	Russell, L. M.; Maria, S. F.; Myneni, S. C., Mapping organic coatings on atmospheric particles. *Geophysical Research Letters* **2002,** *29* (16).

123.	Reinhard, E.; Heidrich, W.; Debevec, P.; Pattanaik, S.; Ward, G.; Myszkowski, K., *High dynamic range imaging: acquisition, display, and image-based lighting*. Morgan Kaufmann: 2010.

124.	O'Brien, R. E.; Wang, B.; Laskin, A.; Riemer, N.; West, M.; Zhang, Q.; Sun, Y.; Yu, X. Y.; Alpert, P.; Knopf, D. A., Chemical imaging of ambient aerosol particles: Observational constraints on mixing state parameterization. *Journal of Geophysical Research: Atmospheres* **2015,** *120* (18), 9591-9605.

125.	Wen, X.-D.; Löble, M. W.; Batista, E. R.; Bauer, E.; Boland, K. S.; Burrell, A. K.; Conradson, S. D.; Daly, S. R.; Kozimor, S. A.; Minasian, S. G., Electronic structure and O K-edge XAS spectroscopy of U3O8. *Journal of Electron Spectroscopy and Related Phenomena* **2014,** *194*, 81-87.

126.	Bourdelle, F.; Benzerara, K.; Beyssac, O.; Cosmidis, J.; Neuville, D. R.; Brown, G. E.; Paineau, E., Quantification of the ferric/ferrous iron ratio in silicates by scanning transmission X-ray microscopy at the Fe L2, 3 edges. *Contributions to Mineralogy and Petrology* **2013,** *166* (2), 423-434.

127.	Baustian, K.; Wise, M.; Jensen, E.; Schill, G.; Freedman, M.; Tolbert, M., State transformations and ice nucleation in amorphous (semi-) solid organic aerosol. *Atmospheric Chemistry and Physics* **2013,** *13*, 5615.

128.	Baustian, K. J.; Cziczo, D. J.; Wise, M. E.; Pratt, K. A.; Kulkarni, G.; Hallar, A.; Tolbert, M. A., Importance of aerosol composition, mixing state, and morphology for heterogeneous ice nucleation: A combined field and laboratory approach. *Journal of Geophysical Research: Atmospheres* **2012,** *117* (D6).

129.	Pöschl, U.; Martin, S.; Sinha, B.; Chen, Q.; Gunthe, S.; Huffman, J.; Borrmann, S.; Farmer, D.; Garland, R.; Helas, G., Rainforest aerosols as biogenic nuclei of clouds and precipitation in the Amazon. *Science* **2010,** *329* (5998), 1513-1516.

130.	DeMott, P. J.; Sassen, K.; Poellot, M. R.; Baumgardner, D.; Rogers, D. C.; Brooks, S. D.; Prenni, A. J.; Kreidenweis, S. M., African dust aerosols as atmospheric ice nuclei. *Geophysical Research Letters* **2003,** *30* (14).

131.	Haynes, W. M., *CRC handbook of chemistry and physics*. CRC press: 2014.

132.	Shiraiwa, M.; Zuend, A.; Bertram, A. K.; Seinfeld, J. H., Gas–particle partitioning of atmospheric aerosols: interplay of physical state, non-ideal mixing and morphology. *Physical Chemistry Chemical Physics* **2013,** *15* (27), 11441-11453.

133.	Karagulian, F.; Lea, A. S.; Dilbeck, C. W.; Finlayson-Pitts, B. J., A new mechanism for ozonolysis of unsaturated organics on solids: phosphocholines on NaCl as a model for sea salt particles. *Physical Chemistry Chemical Physics* **2008,** *10* (4), 528-541.

134.	Kwamena, N.-O.; Buajarern, J.; Reid, J., Equilibrium morphology of mixed organic/inorganic/aqueous aerosol droplets: Investigating the effect of relative humidity and surfactants. *The Journal of Physical Chemistry A* **2010,** *114* (18), 5787-5795.

135.	Bodsworth, A.; Zobrist, B.; Bertram, A. K., Inhibition of efflorescence in mixed organic–inorganic particles at temperatures less than 250 K. *Physical Chemistry Chemical Physics* **2010,** *12* (38), 12259-12266.

136.	Choi, M. Y.; Chan, C. K., The effects of organic species on the hygroscopic behaviors of inorganic aerosols. *Environmental science & technology* **2002,** *36* (11), 2422-2428.

137.	Pósfai, M.; Xu, H.; Anderson, J. R.; Buseck, P. R., Wet and dry sizes of atmospheric aerosol particles: An AFM-TEM Study. *Geophysical Research Letters* **1998,** *25* (11), 1907-1910.

138.	Buseck, P. R.; Posfai, M., Airborne minerals and related aerosol particles: Effects on climate and the environment. *Proceedings of the National Academy of Sciences* **1999,** *96* (7), 3372-3379.

139.	Bertram, A.; Martin, S.; Hanna, S.; Smith, M.; Bodsworth, A.; Chen, Q.; Kuwata, M.; Liu, A.; You, Y.; Zorn, S., Predicting the relative humidities of liquid-liquid phase separation, efflorescence, and deliquescence of mixed particles of ammonium sulfate, organic material, and water using the organic-to-sulfate mass ratio of the particle and the oxygen-to-carbon elemental ratio of the organic component. *Atmospheric Chemistry and Physics* **2011,** *11* (21), 10995-11006.

140.	Tong, H.-J.; Reid, J.; Bones, D.; Luo, B.; Krieger, U., Measurements of the timescales for the mass transfer of water in glassy aerosol at low relative humidity and ambient temperature. *Atmospheric Chemistry and Physics* **2011,** *11* (10), 4739-4754.

141.	Bones, D. L.; Reid, J. P.; Lienhard, D. M.; Krieger, U. K., Comparing the mechanism of water condensation and evaporation in glassy aerosol. *Proceedings of the National Academy of Sciences* **2012,** *109* (29), 11613-11618.

142.	Fard, M. M.; Krieger, U. K.; Peter, T., Kinetic Limitation to Inorganic Ion Diffusivity and to Coalescence of Inorganic Inclusions in Viscous Liquid–Liquid Phase-Separated Particles. *The Journal of Physical Chemistry A* **2017,** *121* (48), 3613-3618.

143.   Skoog, D. A.; Holler, F. J.; Crouch, S. R., *Principles of instrumental analysis*. Thomson Brooks/Cole: 2007.

144.   Greenwood, N. N.; Earnshaw, A., *Chemistry of the Elements*. Elsevier: 2012.

145.   Mouri, H.; Okada, K., Shattering and modification of sea-salt particles in the marine atmosphere. *Geophysical research letters* **1993,** *20* (1), 49-52.

146.   Altaf, M. B.; Freedman, M. A., Effect of Drying Rate on Aerosol Particle Morphology. *The Journal of Physical Chemistry Letters* **2017,** *8* (15), 3613-3618.

147.   Altaf, M. B.; Zuend, A.; Freedman, M. A., Role of nucleation mechanism on the size dependent morphology of organic aerosol. *Chemical Communications* **2016,** *52* (59), 9220-9223.

148.   Virtanen, A.; Joutsensaari, J.; Koop, T.; Kannosto, J.; Yli-Pirilä, P.; Leskinen, J.; Mäkelä, J. M.; Holopainen, J. K.; Pöschl, U.; Kulmala, M., An amorphous solid state of biogenic secondary organic aerosol particles. *Nature* **2010,** *467* (7317), 824.

149.   Dzubay, T.; Hines, L.; Stevens, R., Particle bounce errors in cascade impactors. *Atmospheric Environment (1967)* **1976,** *10* (3), 229-234.

150.   Jain, S.; Petrucci, G. A., A new method to measure aerosol particle bounce using a cascade electrical low pressure impactor. *Aerosol Science and Technology* **2015,** *49* (6), 390-399.

151.   Saukko, E.; Kuuluvainen, H.; Virtanen, A., A method to resolve the phase state of aerosol particles. *Atmospheric Measurement Techniques* **2012,** *5* (1), 259-265.

152.   Jimenez, J.; Canagaratna, M.; Donahue, N.; Prevot, A.; Zhang, Q.; Kroll, J. H.; DeCarlo, P. F.; Allan, J. D.; Coe, H.; Ng, N., Evolution of organic aerosols in the atmosphere. *Science* **2009,** *326* (5959), 1525-1529.

153.   Jacobson, M. Z., Strong radiative heating due to the mixing state of black carbon in atmospheric aerosols. *Nature* **2001,** *409* (6821), 695-697.

154.   Moffet, R. C.; Prather, K. A., In-situ measurements of the mixing state and optical properties of soot with implications for radiative forcing estimates. *Proceedings of the National Academy of Sciences of the United States of America* **2009,** *106* (29), 11872-7.

155.   Fierce, L.; Riemer, N.; Bond, T. C., Explaining variance in black carbon's aging timescale. *Atmospheric Chemistry and Physics* **2015,** *15* (6), 3173-3191.

156.   Warren, D. R.; Seinfeld, J. H., Simulation of aerosol size distribution evolution in systems with simultaneous nucleation, condensation, and coagulation. *Aerosol Science and Technology* **1985,** *4* (1), 31-43.

157.   Peng, J.; Hu, M.; Guo, S.; Du, Z.; Zheng, J.; Shang, D.; Zamora, M. L.; Zeng, L.; Shao, M.; Wu, Y.-S., Markedly enhanced absorption and direct radiative forcing of black carbon under polluted urban environments. *Proceedings of the National Academy of Sciences* **2016,** *113* (16), 4266-4271.

158.   D'Almeida, G. A.; Koepke, P.; Shettle, E. P., *Atmospheric aerosols: global climatology and radiative characteristics*. A Deepak Pub: 1991.

159.   Cappa, C. D.; Onasch, T. B.; Massoli, P.; Worsnop, D. R.; Bates, T. S.; Cross, E. S.; Davidovits, P.; Hakala, J.; Hayden, K. L.; Jobson, B. T., Radiative absorption enhancements due to the mixing state of atmospheric black carbon. *Science* **2012,** *337* (6098), 1078-1081.

160.   Schmidt, G. A.; Ruedy, R.; Hansen, J. E.; Aleinov, I.; Bell, N.; Bauer, M.; Bauer, S.; Cairns, B.; Canuto, V.; Cheng, Y., Present-day atmospheric simulations using GISS ModelE: Comparison to in situ, satellite, and reanalysis data. *Journal of Climate* **2006,** *19* (2), 153-192.

161.   Sedlacek, A. J.; Lewis, E. R.; Kleinman, L.; Xu, J.; Zhang, Q., Determination of and evidence for non-core-shell structure of particles containing black carbon using the Single-Particle Soot Photometer (SP2). *Geophysical Research Letters* **2012,** *39* (6).

162.   Healy, R. M.; Riemer, N.; Wenger, J. C.; Murphy, M.; West, M.; Poulain, L.; Wiedensohler, A.; O'Connor, I. P.; McGillicuddy, E.; Sodeau, J. R., Single particle diversity and mixing state measurements. *Atmospheric Chemistry and Physics* **2014,** *14* (12), 6289-6299.

163.   Streets, D.; Bond, T.; Lee, T.; Jang, C., On the future of carbonaceous aerosol emissions. *Journal of Geophysical Research: Atmospheres* **2004,** *109* (D24).

164.   Artaxo, P.; Rizzo, L. V.; Brito, J. F.; Barbosa, H. M.; Arana, A.; Sena, E. T.; Cirino, G. G.; Bastos, W.; Martin, S. T.; Andreae, M. O., Atmospheric aerosols in Amazonia and land use change: from natural biogenic to biomass burning conditions. *Faraday discussions* **2013,** *165*, 203-235.

165.   Wang, J.; Krejci, R.; Giangrande, S.; Kuang, C.; Barbosa, H. M.; Brito, J.; Carbone, S.; Chi, X.; Comstock, J.; Ditas, F., Amazon boundary layer aerosol concentration sustained by vertical transport during rainfall. *Nature* **2016,** *539* (7629), 416-419.

166.   Martin, S. T.; Andreae, M. O.; Artaxo, P.; Baumgardner, D.; Chen, Q.; Goldstein, A. H.; Guenther, A.; Heald, C. L.; Mayol-Bracero, O. L.; McMurry, P. H., Sources and properties of Amazonian aerosol particles. *Reviews of Geophysics* **2010,** *48* (2).

167.   Bond, T.; Venkataraman, C.; Masera, O., Global atmospheric impacts of residential fuels. *Energy for Sustainable Development* **2004,** *8* (3), 20-32.

168.   Staudt, A.; Jacob, D. J.; Logan, J. A.; Bachiochi, D.; Krishnamurti, T.; Sachse, G., Continental sources, transoceanic transport, and interhemispheric exchange of carbon monoxide over the Pacific. *Journal of Geophysical Research: Atmospheres* **2001,** *106* (D23), 32571-32589.

169.   Kuhn, U.; Ganzeveld, L.; Thielmann, A.; Dindorf, T.; Schebeske, G.; Welling, M.; Sciare, J.; Roberts, G.; Meixner, F.; Kesselmeier, J., Impact of Manaus City on the Amazon Green Ocean atmosphere: ozone production, precursor sensitivity and aerosol load. *Atmospheric Chemistry and Physics* **2010,** *10* (19), 9251-9282.

170.   Martin, S.; Artaxo, P.; Machado, L.; Manzi, A.; Souza, R.; Schumacher, C.; Wang, J.; Andreae, M.; Barbosa, H.; Fan, J., Introduction: observations and modeling of the Green Ocean Amazon (GoAmazon2014/5). *Atmospheric Chemistry and Physics* **2016,** *16* (8), 4785-4797.

171.   Martin, S. T.; Artaxo, P.; Machado, L.; Manzi, A.; Souza, R.; Schumacher, C.; Wang, J.; Biscaro, T.; Brito, J.; Calheiros, A., The Green Ocean Amazon Experiment (GoAmazon2014/5) Observes Pollution Affecting Gases, Aerosols, Clouds, and Rainfall over the Rain Forest. *Bulletin of the American Meteorological Society* **2017,** *98* (5), 981-997.

172.   Swap, R.; Garstang, M.; Greco, S.; Talbot, R.; Kållberg, P., Saharan dust in the Amazon Basin. *Tellus B* **1992,** *44* (2), 133-149.

173.   Martin, S.; Andreae, M.; Althausen, D.; Artaxo, P.; Baars, H.; Borrmann, S.; Chen, Q.; Farmer, D.; Guenther, A.; Gunthe, S., An overview of the Amazonian aerosol characterization experiment 2008 (AMAZE-08). *Atmospheric Chemistry and Physics* **2010,** *10* (23).

174.   Chen, Q.; Farmer, D.; Rizzo, L.; Pauliquevis, T.; Kuwata, M.; Karl, T. G.; Guenther, A.; Allan, J. D.; Coe, H.; Andreae, M., Submicron particle mass concentrations and sources in the Amazonian wet season (AMAZE-08). *Atmospheric Chemistry and Physics* **2015,** *15* (7), 3687-3701.

175.   Andreae, M.; Acevedo, O.; Araùjo, A.; Artaxo, P.; Barbosa, C.; Barbosa, H.; Brito, J.; Carbone, S.; Chi, X.; Cintra, B., The Amazon Tall Tower Observatory (ATTO): overview of pilot measurements on ecosystem ecology, meteorology, trace gases, and aerosols. *Atmospheric Chemistry and Physics* **2015,** *15* (18), 10723-10776.

176.   Artaxo, P.; Martins, J. V.; Yamasoe, M. A.; Procópio, A. S.; Pauliquevis, T. M.; Andreae, M. O.; Guyon, P.; Gatti, L. V.; Leal, A. M. C., Physical and chemical properties of aerosols in the wet and dry seasons in Rondônia, Amazonia. *Journal of Geophysical Research: Atmospheres* **2002,** *107* (D20).

177.   Hartigan, J. A.; Wong, M. A., Algorithm AS 136: A k-means clustering algorithm. *Journal of the Royal Statistical Society. Series C (Applied Statistics)* **1979,** *28* (1), 100-108.

178.   Rebotier, T. P.; Prather, K. A., Aerosol time-of-flight mass spectrometry data analysis: A benchmark of clustering algorithms. *Analytica chimica acta* **2007,** *585* (1), 38-54.

179.   Kodinariya, T. M.; Makwana, P. R., Review on determining number of Cluster in K-Means Clustering. *International Journal* **2013,** *1* (6), 90-95.

180.   Kundu, S.; Kawamura, K.; Andreae, T. W.; Hoffer, A.; Andreae, M. O., Diurnal variation in the water-soluble inorganic ions, organic carbon and isotopic compositions of total carbon and nitrogen in biomass burning aerosols from the LBA-SMOCC campaign in Rondônia, Brazil. *Journal of Aerosol Science* **2010,** *41* (1), 118-133.

181.   Ahlm, L.; Nilsson, E.; Krejci, R.; Mårtensson, E.; Vogt, M.; Artaxo, P., A comparison of dry and wet season aerosol number fluxes over the Amazon rain forest. *Atmospheric Chemistry & Physics Discussions* **2009,** *9* (6).

182.   Li, J.; Pósfai, M.; Hobbs, P. V.; Buseck, P. R., Individual aerosol particles from biomass burning in southern Africa: 2, Compositions and aging of inorganic particles. *Journal of Geophysical Research: Atmospheres* **2003,** *108* (D13).

183.   Ault, A. P.; Moffet, R. C.; Baltrusaitis, J.; Collins, D. B.; Ruppel, M. J.; Cuadra-Rodriguez, L. A.; Zhao, D.; Guasco, T. L.; Ebben, C. J.; Geiger, F. M., Size-dependent changes in sea spray aerosol composition and properties with different seawater conditions. *Environmental Science & Technology* **2013,** *47* (11), 5603-5612.

184.   Pöhlker, C.; Wiedemann, K. T.; Sinha, B.; Shiraiwa, M.; Gunthe, S. S.; Smith, M.; Su, H.; Artaxo, P.; Chen, Q.; Cheng, Y., Biogenic potassium salt particles as seeds for secondary organic aerosol in the Amazon. *Science* **2012,** *337* (6098), 1075-1078.

185.   Brooks, S. D.; Garland, R. M.; Wise, M. E.; Prenni, A. J.; Cushing, M.; Hewitt, E.; Tolbert, M. A., Phase changes in internally mixed maleic acid/ammonium sulfate aerosols. *Journal of Geophysical Research: Atmospheres* **2003,** *108* (D15).

186.   Pósfai, M.; Gelencsér, A.; Simonics, R.; Arató, K.; Li, J.; Hobbs, P. V.; Buseck, P. R., Atmospheric tar balls: Particles from biomass and biofuel burning. *Journal of Geophysical Research: Atmospheres* **2004,** *109* (D6).

187.   Artaxo, P.; Gerab, F.; Yamasoe, M. A.; Martins, J. V., Fine mode aerosol composition at three long-term atmospheric monitoring sites in the Amazon Basin. *Journal of Geophysical Research: Atmospheres* **1994,** *99* (D11), 22857-22868.

188.   Rudich, Y.; Donahue, N. M.; Mentel, T. F., Aging of organic aerosol: Bridging the gap between laboratory and field studies. *Annual Review of Physical Chemistry* **2007,** *58*, 321-352.

189.   Soto-Garcia, L. L.; Andreae, M. O.; Andreae, T. W.; Artaxo, P.; Maenhaut, W.; Kirchstetter, T.; Novakov, T.; Chow, J. C.; Mayol-Bracero, O. L., Evaluation of the carbon content of aerosols from the burning of biomass in the Brazilian Amazon using thermal, optical and thermal-optical analysis methods. *Atmospheric Chemistry and Physics* **2011,** *11* (9), 4425-4444.

190.   Artaxo, P.; Storms, H.; Bruynseels, F.; Van Grieken, R.; Maenhaut, W., Composition and sources of aerosols from the Amazon Basin. *Journal of Geophysical Research: Atmospheres* **1988,** *93* (D2), 1605-1615.

191.   Garstang, M.; Greco, S.; Scala, J.; Swap, R.; Ulanski, S.; Fitzjarrald, D.; Martin, D.; Browell, E.; Shipman, M.; Connors, V., The Amazon boundary-layer experiment (ABLE 2B): a meteorological perspective. *Bulletin of the American Meteorological Society* **1990,** *71* (1), 19-32.

192.   Artaxo, P.; Fernandas, E. T.; Martins, J. V.; Yamasoe, M. A.; Hobbs, P. V.; Maenhaut, W.; Longo, K. M.; Castanho, A., Large-scale aerosol source apportionment in Amazonia. *Journal of Geophysical Research: Atmospheres* **1998,** *103* (D24), 31837-31847.

193.   China, S.; Wang, B.; Weis, J.; Rizzo, L.; Brito, J.; Cirino, G. G.; Kovarik, L.; Artaxo, P.; Gilles, M. K.; Laskin, A., Rupturing of Biological Spores As a Source of Secondary Particles in Amazonia. *Environmental Science & Technology* **2016,** *50* (22), 12179-12186.

194.   Pósfai, M.; Simonics, R.; Li, J.; Hobbs, P. V.; Buseck, P. R., Individual aerosol particles from biomass burning in southern Africa: 1. Compositions and size distributions of carbonaceous particles. *Journal of Geophysical Research: Atmospheres* **2003,** *108* (D13).

195.   Colbeck, I.; Atkinson, B.; Johar, Y., The morphology and optical properties of soot produced by different fuels. *Journal of Aerosol Science* **1997,** *28* (5), 715-723.

196.   Ervens, B.; Cubison, M.; Andrews, E.; Feingold, G.; Ogren, J.; Jimenez, J.; Quinn, P.; Bates, T.; Wang, J.; Zhang, Q., CCN predictions using simplified assumptions of organic aerosol composition and mixing state: a synthesis from six different locations. *Atmospheric Chemistry and Physics* **2010,** *10* (10), 4795-4807.

197.   Medina, J.; Nenes, A.; Sotiropoulou, R. E. P.; Cottrell, L. D.; Ziemba, L. D.; Beckman, P. J.; Griffin, R. J., Cloud condensation nuclei closure during the International Consortium for Atmospheric Research on Transport and Transformation 2004 campaign: Effects of size-resolved composition. *Journal of Geophysical Research: Atmospheres* **2007,** *112* (D10).

198.   Cubison, M.; Ervens, B.; Feingold, G.; Docherty, K.; Ulbrich, I.; Shields, L.; Prather, K.; Hering, S.; Jimenez, J., The influence of chemical composition and mixing state of Los Angeles urban aerosol on CCN number and cloud properties. *Atmospheric Chemistry and Physics* **2008,** *8* (18), 5649-5667.

199.   Stroud, C. A.; Nenes, A.; Jimenez, J. L.; DeCarlo, P. F.; Huffman, J. A.; Bruintjes, R.; Nemitz, E.; Delia, A. E.; Toohey, D. W.; Guenther, A. B., Cloud activating properties of aerosol observed during CELTIC. *Journal of the atmospheric sciences* **2007,** *64* (2), 441-459.

200.   Wang, J.; Cubison, M.; Aiken, A.; Jimenez, J.; Collins, D., The importance of aerosol mixing state and size-resolved composition on CCN concentration and the variation of the importance with atmospheric aging of aerosols. *Atmospheric Chemistry and Physics* **2010,** *10* (15), 7267-7283.

201.   Feng, Y.; Ramanathan, V.; Kotamarthi, V., Brown carbon: a significant atmospheric absorber of solar radiation? *Atmospheric Chemistry and Physics* **2013,** *13* (17), 8607-8621.

202.   Laskin, A.; Laskin, J.; Nizkorodov, S. A., Chemistry of atmospheric brown carbon. *Chemical reviews* **2015,** *115* (10), 4335-4382.

203.   Bond, T. C.; Bergstrom, R. W., Light absorption by carbonaceous particles: An investigative review. *Aerosol science and technology* **2006,** *40* (1), 27-67.

204.   Andreae, M.; Gelencsér, A., Black carbon or brown carbon? The nature of light-absorbing carbonaceous aerosols. *Atmospheric Chemistry and Physics* **2006,** *6* (10), 3131-3148.

205.   Rizzo, L. V.; Artaxo, P.; Mueller, T.; Wiedensohler, A.; Paixao, M.; Cirino, G. G.; Arana, A.; Swietlicki, E.; Roldin, P.; Fors, E. O., Long term measurements of aerosol optical properties at a primary forest site in Amazonia. *Atmospheric Chemistry and Physics* **2013,** *13* (5), 2391-2413.

206.   Joung, Y. S.; Buie, C. R., Aerosol generation by raindrop impact on soil. *Nature communications* **2015,** *6*, 6083.

207.   Joung, Y. S.; Ge, Z.; Buie, C. R., Bioaerosol generation by raindrops on soil. *Nature communications* **2017,** *8*, 14668.

208. Lawless, P. A.; Rodes, C. E.; Ensor, D. S., Multiwavelength absorbance of filter deposits for determination of environmental tobacco smoke and black carbon. *Atmospheric Environment* **2004,** *38* (21), 3373-3383.

209. Hoffer, A.; Gelencsér, A.; Guyon, P.; Kiss, G.; Schmid, O.; Frank, G.; Artaxo, P.; Andreae, M., Optical properties of humic-like substances (HULIS) in biomass-burning aerosols. *Atmospheric Chemistry and Physics* **2006,** *6* (11), 3563-3570.

210. Lack, D.; Langridge, J., On the attribution of black and brown carbon light absorption using the Ångström exponent. *Atmospheric Chemistry and Physics* **2013,** *13* (20), 10535-10543.

211. Veghte, D. P.; China, S.; Weis, J.; Kovarik, L.; Gilles, M. K.; Laskin, A., Optical Properties of Airborne Soil Organic Particles. *ACS Earth and Space Chemistry* **2017,** *1* (8), 511-521.

212. Parworth, C.; Fast, J.; Mei, F.; Shippert, T.; Sivaraman, C.; Tilp, A.; Watson, T.; Zhang, Q., Long-term measurements of submicrometer aerosol chemistry at the Southern Great Plains (SGP) using an Aerosol Chemical Speciation Monitor (ACSM). *Atmospheric Environment* **2015,** *106*, 43-55.

213. Sheridan, P.; Delene, D.; Ogren, J., Four years of continuous surface aerosol measurements from the Department of Energy's Atmospheric Radiation measurement Program Southern Great Plains Cloud and Radiation Testbed site. *Journal of Geophysical Research: Atmospheres* **2001,** *106* (D18), 20735-20747.

214. Ferrare, R.; Turner, D.; Clayton, M.; Schmid, B.; Redemann, J.; Covert, D.; Elleman, R.; Ogren, J.; Andrews, E.; Goldsmith, J. E., Evaluation of daytime measurements of aerosols and water vapor made by an operational Raman lidar over the Southern Great Plains. *Journal of Geophysical Research: Atmospheres* **2006,** *111* (D5).

215. Springston, S. *Radiance Research Particle Soot/Absorption Photometer Instrument Handbook*; DOE ARM Climate Research Facility, Washington, DC (United States): 2016.

216. ARM Data Discovery. https://adc.arm.gov/discovery/ (accessed May-10).

217. Anderson, T. L.; Ogren, J. A., Determining aerosol radiative properties using the TSI 3563 integrating nephelometer. *Aerosol Science and Technology* **1998,** *29* (1), 57-69.

218. Anderson, T.; Covert, D.; Marshall, S.; Laucks, M.; Charlson, R.; Waggoner, A.; Ogren, J.; Caldow, R.; Holm, R.; Quant, F., Performance characteristics of a high-sensitivity, three-wavelength, total scatter/backscatter nephelometer. *Journal of Atmospheric and Oceanic Technology* **1996,** *13* (5), 967-986.

219. Backman, J. C. G.; Virkkula, A. O.; Vakkari, V.; Beukes, P.; van Zyl, P.; Josipovic, M.; Piketh, S.; Tiitta, P.; Chiloane, K.; Petaja, T., Differences in aerosol absorption Ångström exponents between correction algorithms for particle soot absorption photometer measured on South African Highveld. *Atmospheric Measurement Techniques Discussions* **2014**.

220. Hegg, D. A.; Clarke, A. D.; Doherty, S. J.; Ström4, J., Measurements of black carbon aerosol washout ratio on Svalbard. *Tellus B: Chemical and Physical Meteorology* **2011,** *63* (5), 891-900.

221. Fraund, M.; Park, T.; Bonanno, D.; Pham, D. Q.; Moffet, R. C., Quantitative capabilities of STXM to measure spatially resolved organic volume fractions of mixed organic⁄ inorganic particles. *Atmospheric Measurement Techniques* **2019,** *12* (3), 1619.

222. Jennings, S.; Pinnick, R.; Gillespie, J., Relation between absorption coefficient and imaginary index of atmospheric aerosol constituents. *Applied optics* **1979,** *18* (9), 1368-1371.

223. NOAA:OSPO Hazard Mapping System Fire and Smoke Product. https://www.ospo.noaa.gov/Products/land/hms.html (accessed May-10).

224. NWS Quantitative Precipitation Estimates. https://water.weather.gov/precip/ (accessed May-10).

225. Stein, A.; Draxler, R. R.; Rolph, G. D.; Stunder, B. J.; Cohen, M.; Ngan, F., NOAA's HYSPLIT atmospheric transport and dispersion modeling system. *Bulletin of the American Meteorological Society* **2015,** *96* (12), 2059-2077.

226. Rolph, G.; Stein, A.; Stunder, B., Real-time Environmental Applications and Display sYstem: READY. *Environmental Modelling & Software* **2017,** *95*, 210-228.

227. SonomaTechnologiesInc. AirNow - Tech Navigator. http://www.airnowtech.org/navigator/ (accessed May-10).

228. Tivanski, A. V.; Hopkins, R. J.; Tyliszczak, T.; Gilles, M. K., Oxygenated interface on biomass burn tar balls determined by single particle scanning transmission X-ray microscopy. *The Journal of Physical Chemistry A* **2007,** *111* (25), 5448-5458.

229. Lakshmanan, C. M.; Hoelscher, H. E., Production of Levoglucosan by Pyrolysis of Carbohydrates Pyrolysis in Hot Inert Gas Stream. *Starch‐Stärke* **1970,** *22* (8), 261-264.

230. Ibald-Mulli, A.; Timonen, K. L.; Peters, A.; Heinrich, J.; Wölke, G.; Lanki, T.; Buzorius, G.; Kreyling, W. G.; de Hartog, J.; Hoek, G., Effects of particulate air pollution on blood pressure and heart rate in subjects with cardiovascular disease: a multicenter approach. *Environmental health perspectives* **2004,** *112* (3), 369-377.

231. Tong, S.; Schirnding, Y. E. v.; Prapamontol, T., Environmental lead exposure: a public health problem of global dimensions. *Bulletin of the world health organization* **2000,** *78*, 1068-1077.

232.	Walker, S. P.; Wachs, T. D.; Gardner, J. M.; Lozoff, B.; Wasserman, G. A.; Pollitt, E.; Carter, J. A.; Group, I. C. D. S., Child development: risk factors for adverse outcomes in developing countries. *The lancet* **2007,** *369* (9556), 145-157.

233.	Dieter, M. P.; Matthews, H. B.; Jeffcoat, R.; Moseman, R., Comparison of lead bioavailability in F344 rats fed lead acetate, lead oxide, lead sulfide, or lead ore concentrate from Skagway, Alaska. *Journal of Toxicology and Environmental Health, Part A Current Issues* **1993,** *39* (1), 79-93.

234.	Cotter-Howells, J.; Thornton, I., Sources and pathways of environmental lead to children in a Derbyshire mining village. *Environmental Geochemistry and Health* **1991,** *13* (2), 127-135.

235.	Gulson, B.; Korsch, M.; Matisons, M.; Douglas, C.; Gillam, L.; McLaughlin, V., Windblown lead carbonate as the main source of lead in blood of children from a seaside community: an example of local birds as "canaries in the mine". *Environmental Health Perspectives* **2008,** *117* (1), 148-154.

236.	Kennedy, I. M., The health effects of combustion-generated aerosols. *Proceedings of the Combustion Institute* **2007,** *31* (2), 2757-2770.

237.	Flores, J.; Albert, L. A., Environmental lead in Mexico, 1990–2002. In *Reviews of environmental contamination and toxicology*, Springer: 2004; pp 37-109.

238.	Mugica, V.; Maubert, M.; Torres, M.; Muñoz, J.; Rico, E., Temporal and spatial variations of metal content in TSP and PM10 in Mexico City during 1996–1998. *Journal of Aerosol Science* **2002,** *33* (1), 91-102.

239.	Johnson, K. S.; Foy, B. d.; Zuberi, B.; Molina, L.; Molina, M. J.; Xie, Y.; Laskin, A.; Shutthanandan, V., Aerosol composition and source apportionment in the Mexico City Metropolitan Area with PIXE/PESA/STIM and multivariate analysis. *Atmospheric Chemistry and Physics* **2006,** *6* (12), 4591-4600.

240.	Schnaas, L.; Rothenberg, S. J.; Flores, M.-F.; Martínez, S.; Hernández, C.; Osorio, E.; Perroni, E., Blood lead secular trend in a cohort of children in Mexico City (1987–2002). *Environmental health perspectives* **2004,** *112* (10), 1110-1115.

241.	Romieu, I.; Palazuelos, E.; Hernandez Avila, M.; Ríos, C.; Muñoz, I.; Jimenez, C.; Cahero, G., Sources of lead exposure in Mexico City. *Environmental Health Perspectives* **1994,** *102* (4), 384-389.

242.	Hernandez Avila, M.; Romieu, I.; Ríos, C.; Rivero, A.; Palazuelos, E., Lead-glazed ceramics as major determinants of blood lead levels in Mexican women. *Environmental Health Perspectives* **1991,** *94*, 117-120.

243.	Moffet, R. C.; Desyaterik, Y.; Hopkins, R. J.; Tivanski, A. V.; Gilles, M. K.; Wang, Y.; Shutthanandan, V.; Molina, L. T.; Abraham, R. G.; Johnson, K. S., Characterization of aerosols containing Zn, Pb, and Cl from an industrial region of Mexico City. *Environmental Science & Technology* **2008,** *42* (19), 7091-7097.

244.	Christian, T. J.; Yokelson, R. J.; Cárdenas, B.; Molina, L.; Engling, G.; Hsu, S.-C., Trace gas and particle emissions from domestic and industrial biofuel use and garbage burning in central Mexico. *Atmospheric Chemistry and Physics* **2010,** *10* (2), 565-584.

245.	Li, G.; Lei, W.; Bei, N.; Molina, L., Contribution of garbage burning to chloride and PM 2.5 in Mexico City. *Atmospheric Chemistry and Physics* **2012,** *12* (18), 8751-8761.

246.	Moffet, R. C.; Henn, T. R.; Tivanski, A. V.; Hopkins, R. J.; Desyaterik, Y.; Kilcoyne, A.; Tyliszczak, T.; Fast, J.; Barnard, J.; Shutthanandan, V., Microscopic characterization of carbonaceous aerosol particle aging in the outflow from Mexico City. *Atmospheric Chemistry and Physics* **2010,** *10* (3), 961-976.

247.	Laskin, A.; Iedema, M. J.; Cowin, J. P., Time-resolved aerosol collector for CCSEM/EDX single-particle analysis. *Aerosol Science & Technology* **2003,** *37* (3), 246-260.

248.	Li, L.; Yan, H.; Xu, W.; Yu, D.; Heroux, A.; Lee, W.-K.; Campbell, S. I.; Chu, Y. S. In *PyXRF: Python-based X-ray fluorescence analysis package*, X-Ray Nanoimaging: Instruments and Methods III, International Society for Optics and Photonics: 2017; p 103890U.

249.	Ravel, B.; Newville, M., ATHENA, ARTEMIS, HEPHAESTUS: data analysis for X-ray absorption spectroscopy using IFEFFIT. *Journal of Synchrotron Radiation* **2005,** *12* (4), 537-541.

250.	Moffet, R.; Foy, B. d.; Molina, L. a.; Molina, M.; Prather, K., Measurement of ambient aerosols in northern Mexico City by single particle mass spectrometry. *Atmospheric Chemistry and Physics* **2008,** *8* (16), 4499-4516.

251.	Kowalczyk, G. S.; Gordon, G. E.; Rheingrover, S. W., Identification of atmospheric particulate sources in Washington, DC using chemical element balances. *Environmental Science & Technology* **1982,** *16* (2), 79-90.

252.	Aldape, F.; FLORES M, J.; FLORES A, J.; Retama-Hernández, A.; Rivera-Hernández, O., ELEMENTAL COMPOSITION AND SOURCE IDENTIFICATION OF PM 2.5 PARTICLES COLLECTED IN DOWNTOWN MEXICO CITY. *International Journal of PIXE* **2005,** *15* (03n04), 263-270.

253.	Adachi, K.; Tainosho, Y., Characterization of heavy metal particles embedded in tire dust. *Environment International* **2004,** *30* (8), 1009-1017.

254. Liu, L.; Kong, S.; Zhang, Y.; Wang, Y.; Xu, L.; Yan, Q.; Lingaswamy, A.; Shi, Z.; Lv, S.; Niu, H., Morphology, composition, and mixing state of primary particles from combustion sources—crop residue, wood, and solid waste. *Scientific reports* **2017,** *7* (1), 5047.

255. Barrett, J. E.; Taylor, K. G.; Hudson-Edwards, K. A.; Charnock, J. M., Solid-phase speciation of Pb in urban road dust sediment: a XANES and EXAFS study. *Environmental Science & Technology* **2010,** *44* (8), 2940-2946.

256. Tan, M.; Zhang, G.; Li, X.; Zhang, Y.; Yue, W.; Chen, J.; Wang, Y.; Li, A.; Li, Y.; Zhang, Y., Comprehensive study of lead pollution in Shanghai by multiple techniques. *Analytical Chemistry* **2006,** *78* (23), 8044-8050.

257. Graedel, T., Chemical mechanisms for the atmospheric corrosion of lead. *Journal of the Electrochemical Society* **1994,** *141* (4), 922-927.

258. Zhang, Y.; Wang, X.; Chen, H.; Yang, X.; Chen, J.; Allen, J. O., Source apportionment of lead-containing aerosol particles in Shanghai using single particle mass spectrometry. *Chemosphere* **2009,** *74* (4), 501-507.

259. Li, W.; Wang, T.; Zhou, S.; Lee, S.; Huang, Y.; Gao, Y.; Wang, W., Microscopic observation of metal-containing particles from Chinese continental outflow observed from a non-industrial site. *Environmental science & technology* **2013,** *47* (16), 9124-9131.

260. Tan, P. V.; Fila, M. S.; Evans, G. J.; Jervis, R. E., Aerosol laser ablation mass spectrometry of suspended powders from PM sources and its implications to receptor modeling. *Journal of the Air & Waste Management Association* **2002,** *52* (1), 27-40.

261. Lemieux, P. M.; Lutes, C. C.; Abbott, J. A.; Aldous, K. M., Emissions of polychlorinated dibenzo-p-dioxins and polychlorinated dibenzofurans from the open burning of household waste in barrels. *Environmental Science & Technology* **2000,** *34* (3), 377-384.

262. Stockwell, C. E.; Christian, T. J.; Goetz, J. D.; Jayarathne, T.; Bhave, P. V.; Praveen, P. S.; Adhikari, S.; Maharjan, R.; DeCarlo, P. F.; Stone, E. A., Nepal Ambient Monitoring and Source Testing Experiment (NAMaSTE): emissions of trace gases and light-absorbing carbon from wood and dung cooking fires, garbage and crop residue burning, brick kilns, and other sources. *Atmospheric Chemistry and Physics* **2016,** *16* (17), 11043-11081.

263. Jayarathne, T.; Stockwell, C. E.; Bhave, P. V.; Praveen, P. S.; Rathnayake, C. M.; Islam, M.; Panday, A. K.; Adhikari, S.; Maharjan, R.; Goetz, J. D., Nepal Ambient Monitoring and Source Testing Experiment (NAMaSTE): emissions of particulate matter from wood-and dung-fueled cooking fires, garbage and crop residue burning, brick kilns, and other sources. *Atmospheric Chemistry and Physics* **2018,** *18* (3), 2259-2286.

264. Bi, X.; Simoneit, B. R.; Wang, Z.; Wang, X.; Sheng, G.; Fu, J., The major components of particles emitted during recycling of waste printed circuit boards in a typical e-waste workshop of South China. *Atmospheric Environment* **2010,** *44* (35), 4440-4445.

265. Chen, J.; Li, C.; Ristovski, Z.; Milic, A.; Gu, Y.; Islam, M. S.; Wang, S.; Hao, J.; Zhang, H.; He, C., A review of biomass burning: Emissions and impacts on air quality, health and climate in China. *Science of the Total Environment* **2017,** *579*, 1000-1034.

266. Flora, G.; Gupta, D.; Tiwari, A., Toxicity of lead: a review with recent updates. *Interdisciplinary toxicology* **2012,** *5* (2), 47-58.